A WIDE-BANDWIDTH HIGH-SENSITIVITY MEMS GYROSCOPE

A THESIS SUBMITTED TO
THE GRADUATE SCHOOL OF NATURAL AND APPLIED SCIENCES
OF
MIDDLE EAST TECHNICAL UNIVERSITY

BY

KORHAN ŞAHİN

IN PARTIAL FULFILLMENT OF THE REQUIREMENTS
FOR
THE DEGREE OF MASTER OF SCIENCE
IN
ELECTRICAL AND ELECTRONICS ENGINEERING

JULY 2008

Approval of the thesis:

A WIDE-BANDWIDTH HIGH-SENSITIVITY MEMS GYROSCOPE

submitted by **KORHAN ŞAHİN** in partial fulfillment of the requirements for the degree of **Master of Science in Electrical and Electronics Engineering Department, Middle East Technical University** by,

Prof. Dr. Canan Özgen _____
Dean, Graduate School of **Natural and Applied Sciences**

Prof. Dr. İsmet Erkmen _____
Head of Department, **Electrical and Electronics Engineering**

Prof. Dr. Tayfun Akın _____
Supervisor, **Electrical and Electronics Engineering Dept., METU**

Examining Committee Members:

Prof. Dr. Murat Aşkar _____
Electrical and Electronics Engineering Dept., METU

Prof. Dr. Tayfun Akın _____
Electrical and Electronics Engineering Dept., METU

Prof. Dr. Cengiz Beşikçi _____
Electrical and Electronics Engineering Dept., METU

Asst. Prof. Dr. Haluk Külah _____
Electrical and Electronics Engineering Dept., METU

Dr. Said Emre Alper _____
Technical Vocational School of Higher Education, METU

Date: 29.07.2008

I hereby declare that all information in this document has been obtained and presented in accordance with academic rules and ethical conduct. I also declare that, as required by these rules and conduct, I have fully cited and referenced all material and results that are not original to this work.

Name, Last name : Korhan Şahin

Signature :

ABSTRACT

A WIDE-BANDWIDTH HIGH-SENSITIVITY MEMS GYROSCOPE

Şahin, Korhan
M. Sc., Department of Electrical and Electronics Engineering
Supervisor: Prof. Dr. Tayfun AKIN

July 2008, 119 pages

This thesis reports the development of a wide-bandwidth high-sensitivity mode-decoupled MEMS gyroscope showing robustness against ambient pressure variations. The designed gyroscope is based on a novel 2 degrees of freedom (DoF) sense mode oscillator, which allows increasing the operation bandwidth to the amount required by tactical-grade and inertial-grade operations while reaching the mechanical sensitivity of near matched-mode vibratory gyroscopes. Thorough theoretical study and finite element simulations verify the high performance operation of the proposed 2 DoF sense mode oscillator design. The designed gyroscope is fabricated using the in-house developed silicon-on-glass (SOG) micromachining technology at METU Microelectronics (METU-MET) facilities. The fabricated gyroscope measures only 5.1 x 4.6 mm^2.

The drive mode oscillator of the gyroscope reaches quality factor of 8760 under 25 mTorr vacuum environment, owing to high quality single crystal silicon

structural layer. The sense mode bandwidth is measured to reach 2.5 kHz at 40 V proof mass voltage. When the fabricated gyroscope is operated with a relatively wide bandwidth of 1kHz, measurements show a relatively high raw mechanical sensitivity of 131μV/(°/s).

Fabricated gyroscope is hybrid connected to external closed-loop drive mode amplitude control and open-loop sense mode readout electronics developed at METU-MEMS research group, to form a complete angular rate measurement system (ARMS). The scale factor of the ARMS is measured to be 13.1 mV/(◦/s) with a maximum R^2 nonlinearity of 0.0006 % and a maximum percent deviation nonlinearity of 0.141 %, while the maximum deviation of the scale factor for large vacuum level variations between 40 mTorr to 500 mTorr is measured to be only 0.38 %. The bias stability and angle random walk of the gyroscope are measured to be 131°/h and 1.15°/$\sqrt{h}$, respectively.

It is concluded that, the mechanical structure can be optimized to show its theoretical limits of sensitivity with improvements in fabrication tolerances. The proposed 2 DoF sense mode oscillator design shows the potential of tactical-grade operation, while demonstrating extreme immunity to ambient pressure variations, by utilizing an optimized mechanical structure and connecting the gyroscope to dedicated low-noise electronics.

Keywords: Gyroscope, 2 DoF Sense Mode Gyroscope, Robust Gyroscope, Wide-Bandwidth Gyroscope, Microelectromechanical Systems (MEMS).

ÖZ

GENİŞ BANT ARALIĞINA SAHİP YÜKSEK HASSASİYETLİ MEMS DÖNÜÖLÇER

Şahin, Korhan
M. Sc., Elektrik ve Elektronik Mühendisliği Bölümü
Tez Yöneticisi: Prof. Dr. Tayfun AKIN

Temmuz 2008, 119 sayfa

Bu tez çevresel basınç değişimlerine dayanıklı, geniş bant aralığına sahip, yüksek hassasiyetli ve etkileşimsiz MEMS dönüölçer geliştirilmesini anlatmaktadır. Geniş bant aralığına sahip yüksek hassasiyetli dönüölçüm işlemi bu çalışmada önerilen yeni tasarlanmış bir 2 serbestlik dereceli algılama modu osilatörü tarafından sağlanmaktadır. Bu yeni tasarım algılama modu osilatörü, mod frekansı eşleştirmeli dönüölçerlerin hassasiyet seviyelerine yaklaşırken, taktik amaçlı ve ataletsel seyrüsefer denetlemesi amaçlı uygulamaların gerektirdiği geniş bant aralığını sağlamaktadır. Kapsamlı teorik çalışmalara ek olarak yürütülen sonlu elemanlar benzeşimleriyle yeni tasarım algılama modu osilatörünün gösterdiği yüksek performans doğrulanmıştır. Tasarlanan dönüölçer ODTÜ Mikroelektronik tesislerinde geliştirilen cam-üzeri-silisyum mikroişleme yöntemiyle üretilmiştir. Üretilen dönüölçer yalnızca 5,1 x 4,6 mm^2'lik bir yüzey alanı kaplamaktadır.

Tasarlanan dönüölçerin sürüş modu osilatörü, yüksek kaliteli kristal silisyum yapısı sayesinde, 25 mTorr vakum altında 8760 kalite faktörü göstermiştir. Algılama modu osilatörü 40 V potansiyel altında 2,5 kHz bant aralığı göstermektedir. Tasarlanan algılama modu osilatörü 1 kHz bant aralığıyla çalıştırıldığında 131 μV/(°/s) işlenmemiş dönü hassasiyetine sahiptir.

Üretilen dönüölçer METU-MEMS grubunda tasarlanan kapalı devre sürüş modu genlik kontrolü ve açık devre algılama modu okuma devrelerine bağlanarak bütün bir açısal hız ölçüm sistemi hazırlanmıştır. Bu sistemin orantı katsayısı 13,1 mV/(◦/s) olarak ölçülürken, orantı katsayısının çevresel basıncın 40 mTorr ve 500 mTorr arasında değiştirilmesine gösterdiği duyarlılık sadece % 0,38 olarak gözlemlenmiştir. Bu şartlar altında R^2 orantı katsayısı hatası en yüksek % 0,0006, orantı katsayısının yüzdesel doğrusallıktan en yüksek sapması % 0,141 olarak ölçülmüştür. Üretilen açısal dönüş hızı ölçüm sistemi 131°/h sabit kayma kararlılığı ve 1,15°/$\sqrt{h}$ açısal rastgele hareket değeri göstermektedir.

Araştırma sonucunda, tasarlanan 2 serbestlik dereceli algılama modu osilatörü dönü hassasiyetinin üretim toleranslarının iyileştirilmesiyle teorik üst sınırlarına ulaşabileceği sonucuna varılmıştır. Bu şekilde tasarlanan dönüölçerin düşük gürültülü elektronik devrelere bağlanmasıyla elde edilecek açısal hız ölçüm sistemi, taktik amaçlı uygulamaların gerektirdiği yüksek hassasiyeti sağlarken, çevresel basınç değişimlerine karşı yüksek dayanım gösterecektir.

Anahtar Kelimeler: Dönüölçer, 2 Serbestlik Dereceli Algılama Modu Osilatörüne Sahip Dönüölçer, Çevresel Değişkenlere Dayanıklı Dönüölçer, Geniş Bant Aralığına Sahip Dönüölçer, Mikroelektromekanik Sistemler (MEMS).

To the precious people that make this world a livable place for me:

My family

ACKNOWLEDGEMENTS

First, I would like to express my deepest gratitude to my supervisor Prof. Dr. Tayfun Akın for his guidance, support, encouragement, and help throughout my graduate studies and the development of this thesis. It is a great opportunity for me to work with him during the course of my research.

I also would like to thank Dr. Said Emre Alper. His instructive and friendly attitude is very valuable for a gyroscope researcher. Our discussions on MEMS gyroscopes were very useful in the achievements of my research.

I would like to express my special thanks to Emre Şahin. He has always helped me with his circuits, day and night all through the characterization phase with his friendly manner.

I am grateful to all METU-MEMS research group members. It was them who made my research an enjoyable practice by their friendly manner all through our conversations and social activities. My special thanks are to İlker Ender Ocak for his helps in taking SEM pictures of my gyroscope and for discussions on nonlinearity figures of gyroscopes.

My special thanks are to Mr. Orhan Akar and METU-MET staff, who keep the facilities up and running with great effort.

I would like to express my gratitude to Ercihan İncetürkmen. Our conversations on economics and life during sleepless nights were always keeping me motivated.

I would like to express my special thanks to Dr. Kağan Topallı, “my elder brother”. I had the privilege to meet him at my sophomore year in the Department of Electrical and

Electronics Engineering. Over years he was always supporting me in any situation that I face. He was the one to answer my endless questions about our profession. Without his friendship my Electrical and Electronics Engineering years would not be that pleasant to me.

My very special thanks are to my undergraduate double major advisor Prof. Dr. Gülbin Dural. It was very though to carry on my double major studies in undergraduate years, but she was the one to motivate me all through my hard times with her friendly and hearty manner. Without her endless support neither could I achieve to complete my double major studies, nor go on with my graduate study at METU-MEMS research group.

My last but the biggest thanks are to my family. They raised me in a lovely atmosphere. They were always respecting even my worst ideas about life and science. They are the source of my willing to live, my curiosity, my self confidence and my eagerness to learn. I could not even imagine a life without their love and endless support.

TABLE OF CONTENTS

LIST OF TABLES

LIST OF FIGURES

CHAPTER 1

INTRODUCTION

Although miniaturization has been performed over centuries in artistic form, it was the demonstration of the first integrated circuit by Kilby [1] in 1958 that drives attention to developing miniaturized electronics systems. With the improvements in IC fabrication techniques, the speeds and capabilities of the integrated circuits increased enormously, while their sizes are getting smaller and smaller. After the industrial revolution of the 19th century, the developments in IC technology were so impressive on the lives of mankind that, the 20th century was called the solid state devices era. After that, late 20th century has witnessed the start of a new era with the idea of fabricating mechanical components using the IC fabrication technology and integrating those with electronic components. The integration of mechanical and electronic components using IC fabrication techniques is known as the field of Micro Electro Mechanical Systems (MEMS). MEMS devices offer the advantages of low cost, low power consumption, low volume and weight but high operation speeds when compared to their macro counterparts. On the other hand, MEMS technology not only offered improvements in already known devices but also enabled the production of novel devices that do not have macro counterparts; therefore, origination of MEMS deserves to be called as the start of a new era.

One of the key usage areas of the MEMS technology is the field of inertial measurement. Basic inertial measurement devices are of two kinds: accelerometers and gyroscopes. Accelerometers are devices measuring the linear acceleration of the center of mass of a body, while gyroscopes are used to measure angular rotation rates of a body. It is the development of micromachined accelerometers that made airbags standard accessories for many automobiles. Some other applications of

MEMS inertial sensors in automotive industry are traction and yaw control systems. Stabilization of handheld camera optics, virtual reality systems and inertial joysticks are some of the devices in consumer electronics category where micromachined inertial sensors are the novel solutions because of their small sizes and low power consumption.

Although aforementioned devices are the most popular applications of MEMS inertial sensors, the most demanding application area for MEMS inertial sensors is the area of inertial navigation. The position of the center of mass of a rigid body at space can exactly be determined with the knowledge of its x-y-z coordinates measured with respect to a known origin. Knowledge of the rotation angles of the body around x-y-z axis in addition to the position of mass center will be sufficient to spot any point of interest of the rigid body in space. For the measurement of the mentioned coordinates and rotations, 3 accelerometers and 3 gyroscopes are utilized respectively in an inertial measurement unit (IMU). By double integration of the acceleration data extracted by accelerometers, with accurate knowledge of initial position, the location of the center of mass of the body can be traced in course of its motion. Meanwhile the orientation of the body is traced by integrating the angular velocity data output of the gyroscopes. Global positioning system (GPS) is another means of the measurement of position coordinates by the use of satellites located around the earth. On the other hand, although GPS gives very accurate measurement results, its reliability is a big concern such that any loss of connection with the satellites will result in the system using GPS to lack the position information. Therefore, many inertial navigation applications like spacecrafts, autonomous underwater vehicles (AUV), unmanned aerial vehicles (UAV) and guided missiles utilize both the inertial measurement units and GPS systems. The weights and power consumptions of the IMUs utilized is the most important factor in all the mentioned applications, as the extra weight added by the IMU will result in a decrease in the payloads of those devices. Today's IMUs consist of bulky and heavy mechanical and optical accelerometers and gyroscopes; therefore, there is a great interest in MEMS community to increase the performance of micromachined accelerometers and gyroscopes to achieve inertial-grade performances.

Micromachined accelerometers aimed for inertial-grade applications, achieving micro-g resolutions have already been reported [2, 3]. On the other hand micromachined gyroscopes are far away from inertial-grade performance due to their complex mechanical structures in addition to increased dedicated electronics requirement. Hence the need for improved mechanical designs, low-noise dedicated electronics and high quality packaging for micromachined gyroscopes still remains to be a hot topic in the MEMS research community.

This thesis presents a new micromachined vibratory gyroscope with a novel 2 degrees of freedom (DoF) sense mode oscillator design in order to obtain a robust operation against ambient temperature and pressure variations, while showing a potential to be utilized in tactical-grade applications. The organization of this chapter is as follows; Section 1.1 gives a brief introduction of micromachined vibratory gyroscopes. Section 1.2 deals with the performance criteria and challenges in the design of micromachined vibratory gyroscopes. Section 1.3 presents an overview of micromachined vibratory gyroscopes in literature. Finally, Section 1.4 gives the research objectives and the organization of the thesis.

1.1 Micromachined Vibratory Gyroscopes

Figure 1.1 illustrates the schematic view of a micromachined vibratory gyroscope with single DoF drive and sense modes composed of a mass, called *proof mass* attached to the *gyro frame* with spring-damper type linkages. The proof mass is driven into oscillations in the *drive axis* as shown in Figure 1.2 (a) during operation of the gyroscope, using actuators commonly utilizing actuation mechanisms such as electromagnetic, electrostatic, and piezoelectric. When the gyro frame is rotated around the out-of-plane axis called the *sensitive axis* of the gyroscope, an oscillatory motion at the same frequency of sustained drive oscillations is induced in the *sense axis* which is orthogonal to the drive axis, as shown in Figure 1.2 (b). The induction of oscillations in the sense axis is due to the transfer of some vibration energy from the drive mode to the sense mode under the existence of input rotations. This

transfer of energy is called *Coriolis coupling* after the French scientist Gaspard Gustave de Coriolis.

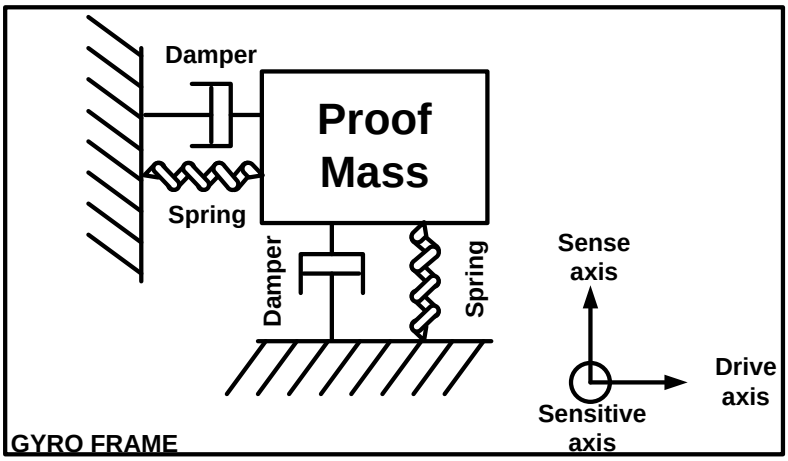

Figure 1.1: Schematic view of a micromachined vibratory gyroscope with single DoF drive and sense modes.

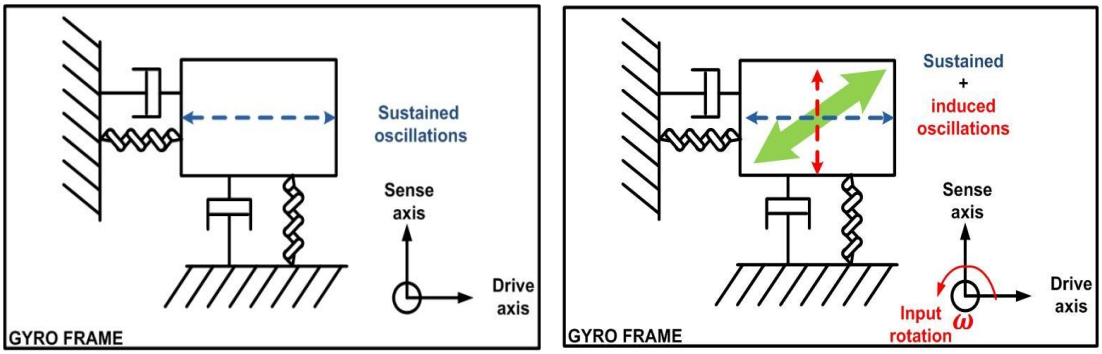

(a) **(b)**

Figure 1.2: The oscillatory motion of the proof mass. (a) Sustained oscillations. (b) Superposition of sustained and induced oscillations.

For an observer sitting on the gyro frame, the motion of the proof mass will be the superposition of the sustained and induced oscillations as shown in Figure 1.2 (b); on the other hand, an observer outside of the gyro frame will observe both the superposition of the sustained and induced oscillations and the rotation of the gyro frame, hence will notice the motion of the proof mass as a complex helical path. In order to extract the applied angular rate information, the amplitude of induced sense

mode vibrations has to be detected. For this purpose, special sensing elements are located on the gyro in a manner to detect only the induced oscillations. Those sense elements can be of electromagnetic, capacitive, and piezoresistive type, but capacitive and piezoresistive sense mechanisms are the most commonly utilized sense mechanisms in gyroscope designs due to their easy implementation using MEMS fabrication techniques.

1.2 Performance Parameters and Challenges in Design of Micromachined Vibratory Gyroscopes

There are a number of parameters determined for vibratory gyroscopes to classify their performance grades. The most importants of them can be listed as *scale factor, resolution, zero-rate output (ZRO)*, and *bias drift* [4].

The scale factor of a vibratory gyroscope defines the change in the electrical signal output in response to a change in applied angular rate input, and has the unit of $V/(^o/s)$.

The resolution of a gyroscope is determined by the random noise observed at the output of the gyroscope in the absence of any angular rate input. Resolution is determined by the rate input that would produce this noise output per square root of bandwidth of measurement and has the unit of $(^o/s)/\sqrt{Hz}$. *Angle random walk* is another parameter used to express the resolution of a gyroscope. It is the buildup of error generated by the random noise in time, by definition [5], and has the unit of $^o/\sqrt{h}$.

The zero-rate output is the electrical signal observed at the output of the gyroscope in the absence of any rate input. The source of ZRO is mainly the coupling of oscillations in the drive direction to the sense mode, in addition to phase errors introduced by demodulation electronics. Ideally there should be no oscillation in the sense mode for zero angular input rate as the drive mode of a gyroscope is oscillating, On the other hand, due to the poor fabrication tolerances associated with

micromachining, there appears to be oscillations in the sense mode in the absence of any rate input, which is called *quadrature coupling*. ZRO does not appear as a noise term as the source of ZRO is mainly the coupling of oscillations in drive direction to the sense mode. Rather ZRO shows itself as a constant DC offset signal at the sense mode output of the gyroscope.

Bias drift is another important gyroscope parameter. There appears a slow fluctuation at the output of a gyroscope in the absence of an angular rate input, due to electronics or other components susceptible to random flickering [6]. This is called the bias drift or bias instability and has the unit of $^{o}/h$.

According to the aforementioned performance parameters, there are three classes of gyroscopes: rate-grade, tactical-grade and inertial-grade. Table 1.1 summarizes the performance requirements for the three classes of gyroscopes [4]. It is observed that one of the most important parameters to be improved to achieve inertial-grade performance is the signal to noise ratio (SNR) of the gyroscope when Table 1.1 is investigated considering the performance parameters. The gain of electronics stages can be increased in order to maximize the signal output from the gyroscope, but then the extra amplifier stages will add additional noise to the system; therefore, improving the mechanical sensitivity is considered to be a better solution in improving the SNR performance of a micromachined vibratory gyroscope.

Table 1.1: Performance requirements for the three classes of gyroscopes

Parameter	**Rate-grade**	**Tactical-grade**	**Inertial-grade**
Angle Random Walk $^{o}/\sqrt{h}$	>0.5	0.5-0.05	<0.001
Bias Drift $^{o}/h$	10-1000	0.1-10	<0.01
Scale factor Accuracy, %	0.1-1	0.01-0.1	<0.001
Full Scale Range $^{o}/s$	50-1000	>500	>400
Max Shock in 1ms, g's	10^3	10^3-10^4	10^3
Bandwidth, Hz	>70	~ 100	~ 100

It is necessary to increase the amplitude of drive mode vibrations in order to increase the mechanical sensitivity of a vibratory gyroscope, as Coriolis coupling is directly proportional to this parameter. For a mechanical oscillator, there is a frequency at which the vibration amplitude for a given force is maximum, called the *resonance frequency* of the system. Moreover, the resonance vibration amplitude will be increased significantly by operating the gyroscope at vacuum. Increasing the amplitude of drive mode vibrations is necessary but not sufficient. Increasing the amplitude of vibrations in the sense mode by tuning the sense mode resonance frequency close to the drive mode resonance frequency is the second requirement in improving the Coriolis coupling effect. Tuning the sense mode resonance frequency close to the drive mode resonance frequency is called *mode matching*, and there are a number of devices reported in literature relying on performance improvement by mode-matching [7-15].

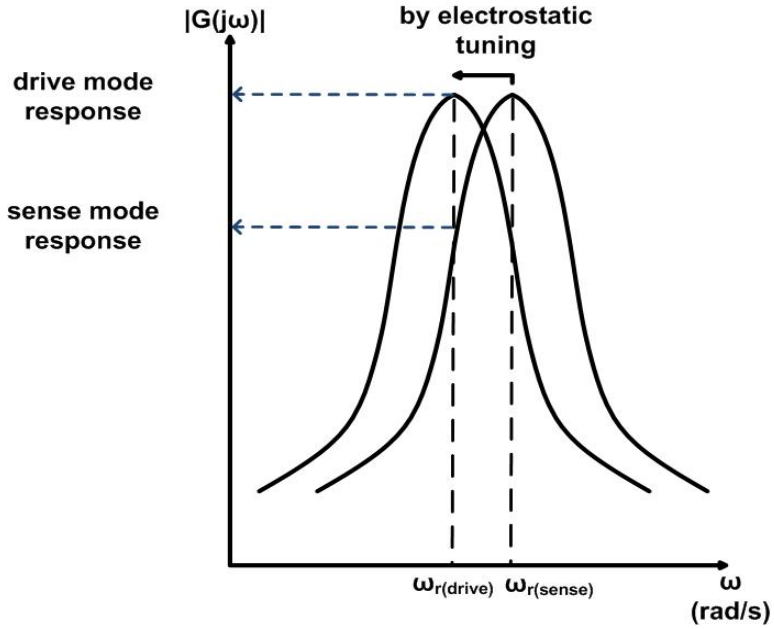

Figure 1.3: Frequency response characteristics for a vibratory gyroscope with single degree of freedom drive and sense modes, demonstrating improved sense mode response by mode-matching.

Figure 1.3 shows the frequency response characteristics for a vibratory gyroscope with single degree of freedom drive and sense modes, demonstrating improved sense

mode response by mode-matching. In practice sense mode resonance frequency of the vibratory gyroscope is tuned electrostatically by the negative electrostatic spring effect of varying-gap type capacitive plates as demonstrated in Section 2.6.2.

Although mechanical sensitivity of a gyroscope is improved significantly through mode-matching, there are three problems associated with this approach. Firstly matched modes result in increased quadrature coupling, which may result in saturation of sense mode electronics in addition to degrading the SNR performance. Mode-matched gyroscopes with decoupled oscillation modes are suggested in order to cope with the increased cross coupling problem, [7, 8, 10-13, 16-18]. The schematic view of a decoupled vibratory gyroscope is shown in Figure 1.4. The frictionless rollers of Figure 1.4 restrict the coupling of the oscillation in one direction to the other by defining the direction of oscillations precisely. In practice, instead of frictionless rollers, dedicated flexible linkage structures are utilized in micromachined vibratory gyroscopes.

Second problem associated with mode-matched gyroscopes is the limited operation bandwidth. The operation bandwidth of a gyroscope is dependent on the amount of mismatch between the drive and sense mode resonance frequencies and mode-matched and near-match gyroscopes are limited to operation bandwidths to less than a few Hz.

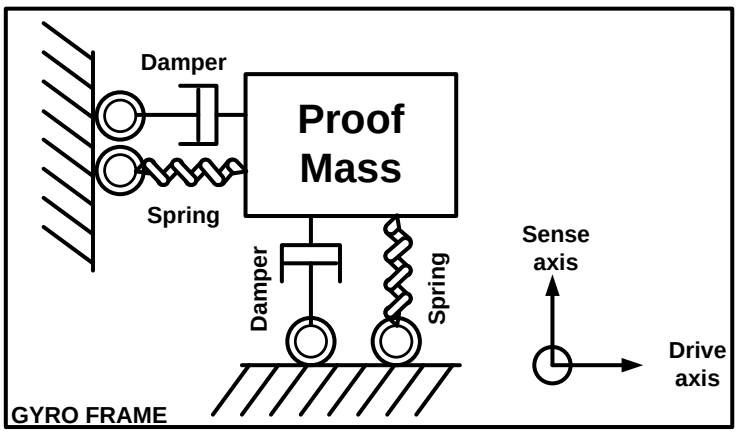

Figure 1.4: Schematic view of a decoupled vibratory gyroscope.

The third problem associated with mode-matched operation is the lack of robustness, which is one of the most important properties of a gyroscope when long-term performance is of concern. Drive mode actuators of gyroscopes are operated at their resonance frequencies using dedicated electronics trying to lock the operating frequency at a close proximity of the resonance peak. The frequency response characteristics show very sharp resonance peaks as the gyroscopes are operated at high vacuum conditions, therefore, limiting the possibility for exact determination of the operating frequency. The result of the uncertainty may result in very small fluctuations in the operating frequency set by the electronics, resulting in fluctuations in the sense mode response for the same applied angular rate input. Moreover fluctuations in ambient conditions like temperature and pressure result also in variations in the resonance peaks of the drive modes, therefore the robustness of the gyroscope becomes a big concern for mode-matched gyroscopes.

A closed-loop control scheme on the sense mode oscillator called *force-feedback type control*, is utilized in literature [19, 21] in order to increase the operation bandwidth of the gyroscopes while eliminating the need for precise control of the relative amount of mismatch between the vibration modes. Force-feedback type gyroscopes employ dedicated electronics to track vibratory motion in the sense mode and apply a force on the proof mass so as to cancel the vibrations induced by the Coriolis coupling. Although the mechanical response characteristics of the gyroscope cannot be modified this way, the response characteristics of the electrical signal output is shaped so as to demonstrate improved bandwidth and robustness. On the other hand, the increased complexity of the gyroscope electronics will be the key factor in determining the resolution of the gyroscope, as adding electronic components to the system will increase the amount of random noise generated, inevitably degrading the SNR performance.

Another method to improve the operation bandwidth and robustness of a micromachined vibratory gyroscope is to shape the mechanical response characteristics by utilizing 2 DoF sense mode oscillators as shown in Figure 1.5. For this configuration, the proof mass is the Coriolis coupling element. Sustained

oscillations of the proof mass excite the *sense mass*, which is flexibly connected to the proof mass, and applied angular rate information is extracted from the vibration of the sense mass.

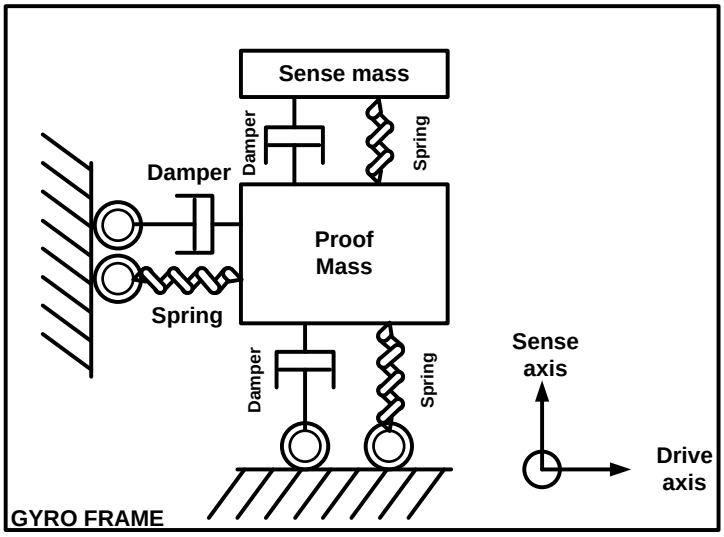

Figure 1.5: Schematic view of a vibratory gyroscope with 2 DoF sense mode oscillator.

2 DoF sense mode configuration results in the frequency response characteristics of the sense mass demonstrated in Figure 1.6. For a 2 DoF sense mode oscillator, there are two resonance peaks and a flat-band between them. If the drive mode resonance frequency is designed to be in the flat-band region, the response from the sense mode will be constant for a given time-varying angular rate input, significantly increasing the operation bandwidth of the gyroscope. Moreover, small fluctuations in the operating frequency set by the electronics will not affect the response to angular rate inputs in this case. There are a number of gyroscope designs utilizing 2 DoF sense mode oscillators to improve the bandwidth and robustness of a micromachined vibratory gyroscope [17, 22-24]. However, the weakness of the 2 DoF sense mode oscillators is the reduction in the mechanical sensitivity of the sense mode oscillator at the flat-band region. The reduction in the mechanical sensitivity results in a reduction in the signal output of the 2 DoF sense mode gyroscope, hence degrading the SNR performance. A new 2 DoF sense mode oscillator to cope with the SNR degradation problem is proposed in this research.

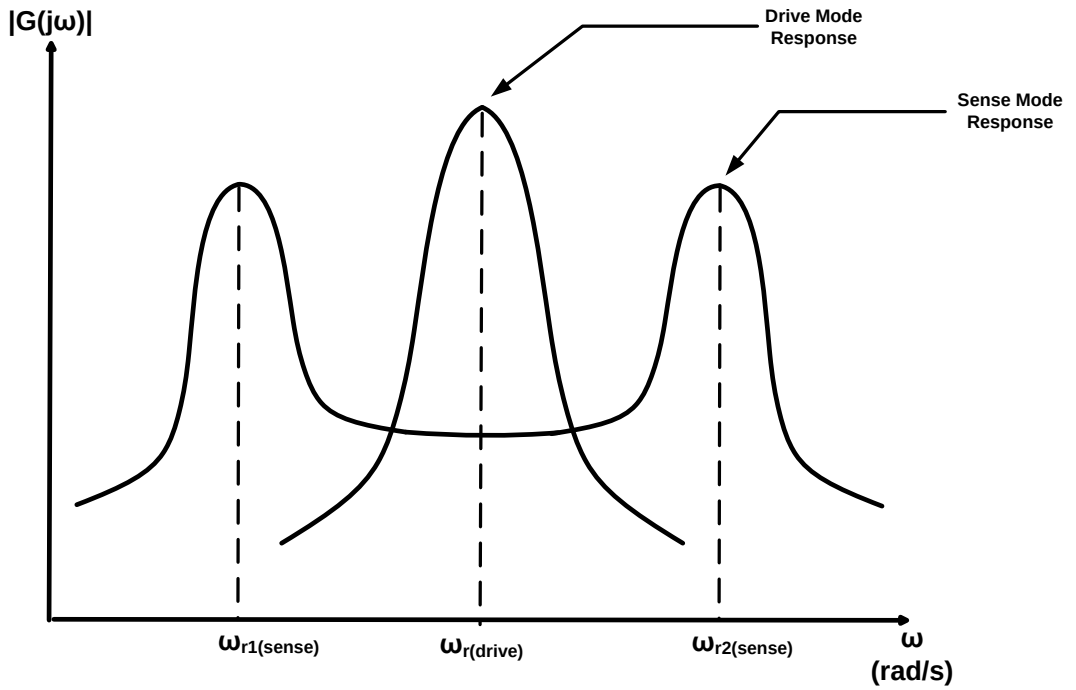

Figure 1.6: Frequency response characteristics for a vibratory gyroscope with single DoF drive and 2 DoF sense mode oscillators.

Sensitivity to linear accelerations is another big challenge in micromachined vibratory gyroscope design. A linear acceleration applied on the gyro frame in the sense direction will result in a deflection of the proof mass in the sense direction, and this deflection cannot be differentiated from the deflection due to Coriolis coupling. Designing the sense mode oscillator stiffer may be a solution, but this will also result in degradation of the sense mode oscillator response to Coriolis induced vibrations. Another way to cope with linear acceleration problem is to connect two proof masses and drive them in opposite directions, called *differential drive mechanism*, as shown in Figure 1.7. This configuration is called a *tuning-fork* structure. Because of the differential drive mechanism, the spring connection in between the two masses acts as a *node* of vibrations in a tuning fork structure. When a rotation is applied to the gyro frame, the masses start to oscillate in the sense direction with 180 º phase shift. In order to extract the applied rotation information, the amplitude of vibrations of the two proof masses in the sense directions are subtracted by *differential sense mode readout electronics*. As the response of the two masses are subtracted, any deflection in the sense mode due to common mode linear accelerations will be canceled out, while the signal generated

due to Coriolis coupling is doubled. Tuning fork structures are commonly used in micromachined vibratory gyroscope designs for research purposes as well as in commercial products [9, 14, 15, 24, 25].

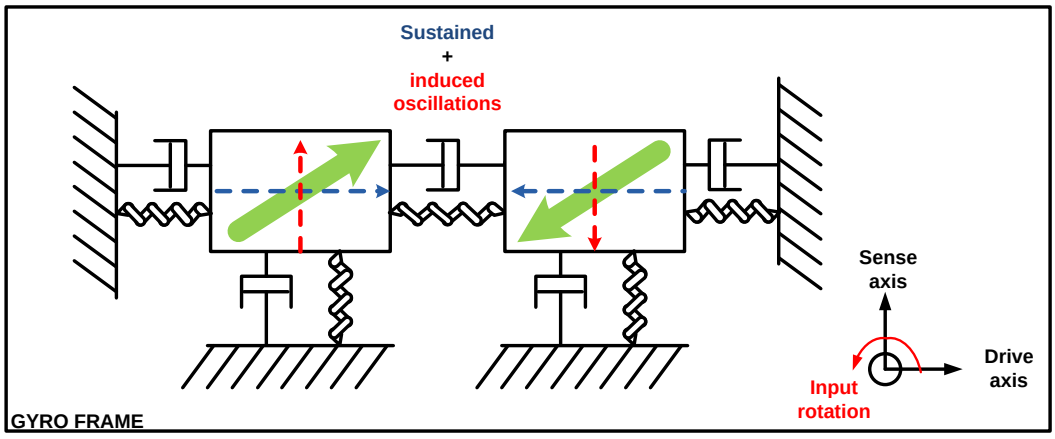

Figure 1.7: A tuning-fork type vibratory gyroscope structure.

1.3 Overview of Reported Micromachined Vibratory Gyroscopes

Quartz micromachined vibratory gyroscopes have already been demonstrated in 1980s but it was early 1990s that research interest emerged on silicon micromachined vibratory gyroscopes. In 1991, one of the first batch fabricated silicon micromachined gyroscopes was reported by the Charles Stark Draper Laboratory. This was a bulk micromachined double gimbal structure supported by torsional flexures, and demonstrated an angular rate resolution of 4 °/s in a 1 Hz bandwidth [26]. Later, on 1994, Draper reported a tuning fork design fabricated by silicon-on-glass (SOG) micromachining technology [27]. This was one of the breakthroughs of that time, as the angle random walk of the design was measured to be 0.72 $°/\sqrt{h}$ with a bias stability of 55 °/h. Figure 1.8 shows the SEM image of Draper's tuning fork design driven into sustained oscillations electrostatically using comb drive actuators, while the sense mode oscillations are detected via capacitive sense plates.

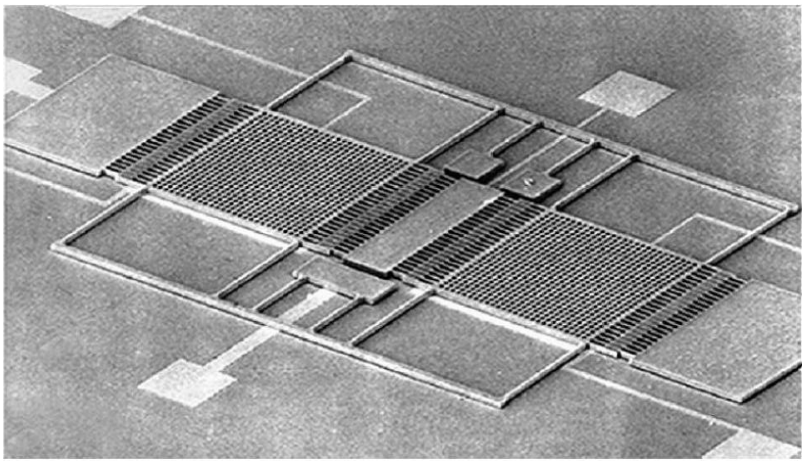

Figure 1.8: SEM image of the tuning-fork type gyroscope of Draper fabricated with SOG technology [27].

During the studies on vibrating plate type gyroscopes were going on, University of Michigan researchers proposed a new gyroscope structure utilizing a micromachined ring as the vibrating element [28] as shown in Figure 1.9. In this gyroscope, the micromachined ring structure was being vibrated in the drive axis but the Coriolis coupling induced oscillations are observed to appear on an axis that is 45 º apart of the drive axis as shown in Figure 1.10. The main advantage of the vibrating ring structure is its inherent symmetry, improving the gyroscopes immunity to variations in ambient temperature. This design showed a resolution of ~1 º/s in 1 Hz bandwidth.

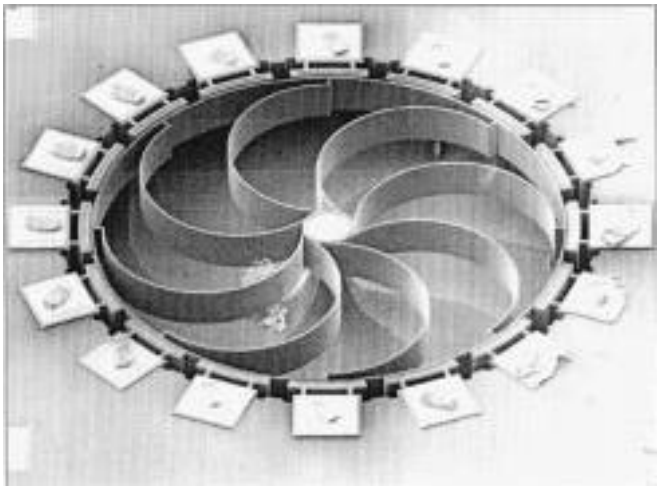

Figure 1.9: SEM image of the vibrating ring type gyroscope produced by University of Michigan [28].

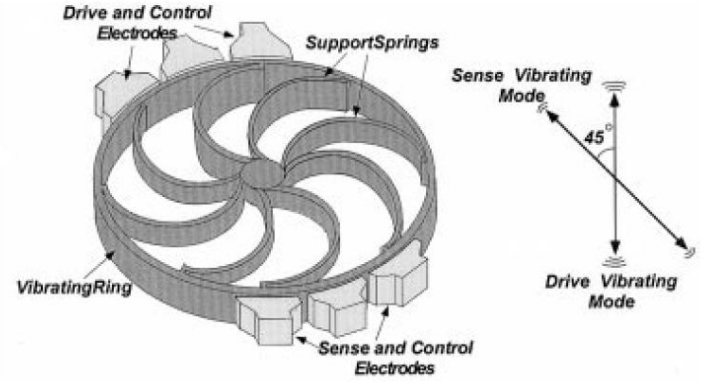

Figure 1.10: Schematic illustration of drive and sense mode oscillations for a vibrating ring gyroscope [28].

Another important research group in this field is the MEMS group at Georgia Institute of Technology, which has been working on improving the performance of vibratory gyroscopes by mode-matching for years [9, 14, 15]. In 2008, they have reported a tuning-fork gyroscope working at perfect mode-matched condition by the help of a dedicated circuit that automatically matches the drive and sense mode frequencies [15]. The SEM view of the reported gyroscope is shown in Figure 1.11. This design has demonstrated a bias drift of 0.15 °/h with an angle random walk of $0.003\ ^{\circ}/\sqrt{\text{h}}$.

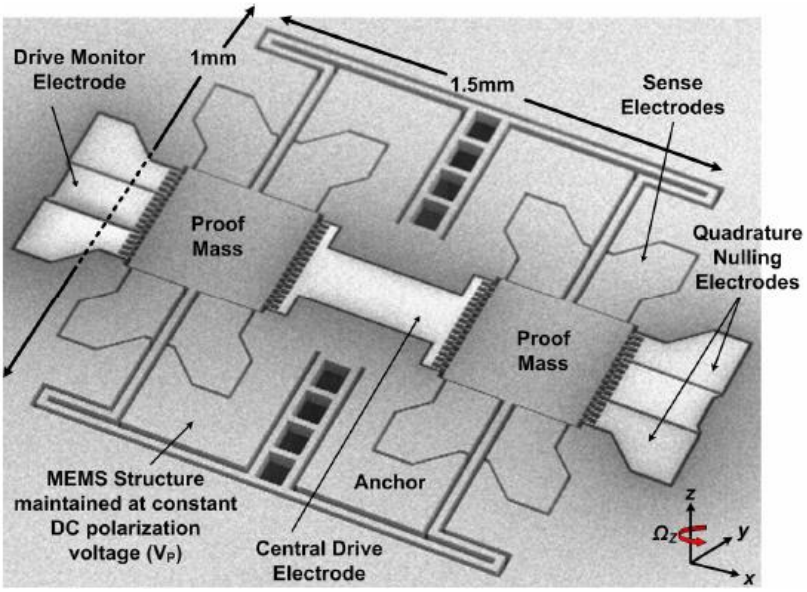

Figure 1.11: SEM image of the mode-matched tuning fork gyroscope produced by Georgia Institute of Technology [15].

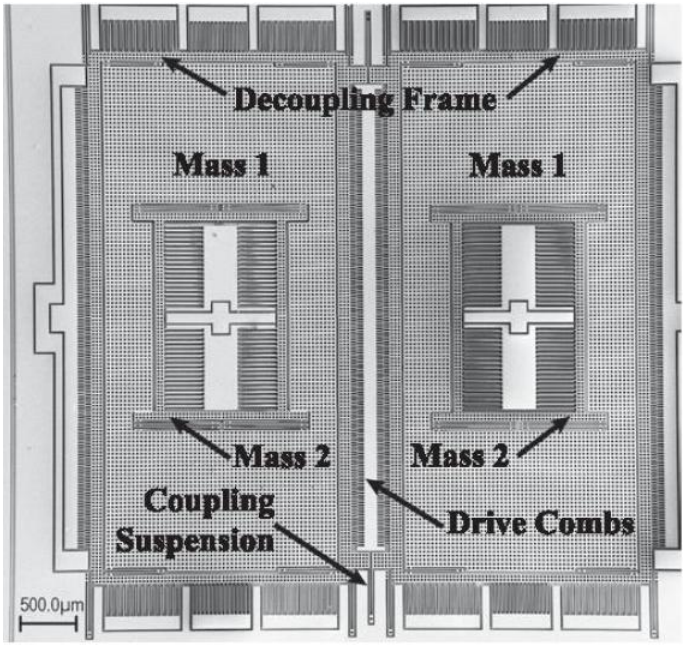

Figure 1.12: SEM image of the robust tuning fork gyroscope produced by University of California Irvine [24].

Improving the operation bandwidth and robustness of micromachined gyroscopes by utilizing multi degree of freedom sense mode oscillators is mostly studied by the researchers of University of California Irvine. Their most recent work is a robust tuning-fork gyroscope with single DoF drive and 2 DoF sense modes with an operation bandwidth >500 Hz. The SEM image of this design is shown in Figure 1.12 [24].

Another way to improve the performance of micromachined gyroscopes is to integrate the mechanical structure of the gyroscope with the electronic circuitry on the same die. In this approach, the need of connecting the mechanical sensor element with circuitry in hybrid packages is eliminated. Therefore, the parasitic capacitances introduced by wire interconnects disappear, resulting in superior SNR performance of monolithic gyroscopes. Carnegie Mellon University is one of the most active universities conducting research on monolithic integration in MEMS gyroscopes. Their research is on releasing the mechanical structure buried in the CMOS die after the circuitry is fabricated [29]. This fabrication method of monolithic integration is called post-CMOS micromachining. Figure 1.13 shows the cross sectional view of a post-CMOS processed device.

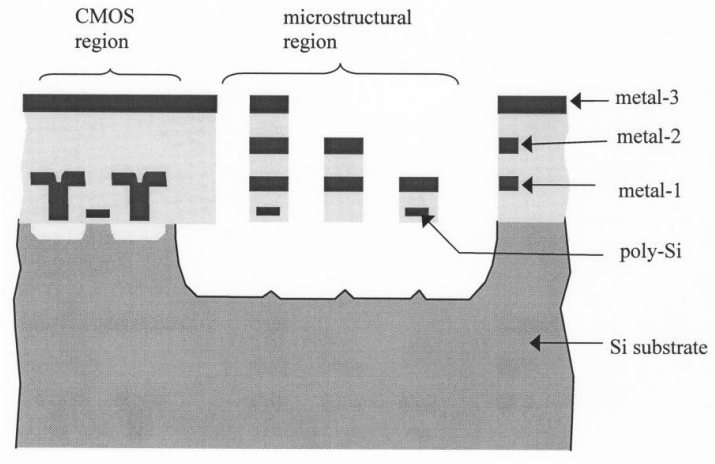

Figure 1.13: Cross sectional view of a post-CMOS processed device fabricated by Carnegie Mellon University [29].

Analog Devices is batch fabricating monolithic MEMS gyroscopes since 2002 using their iMEMS process, which is an intra-CMOS micromachining process [29] based on the BiCMOS IC fabrication technology. Figure 1.14 shows the die view of the iMEMS ADXRS gyroscope of Analog Devices [25].

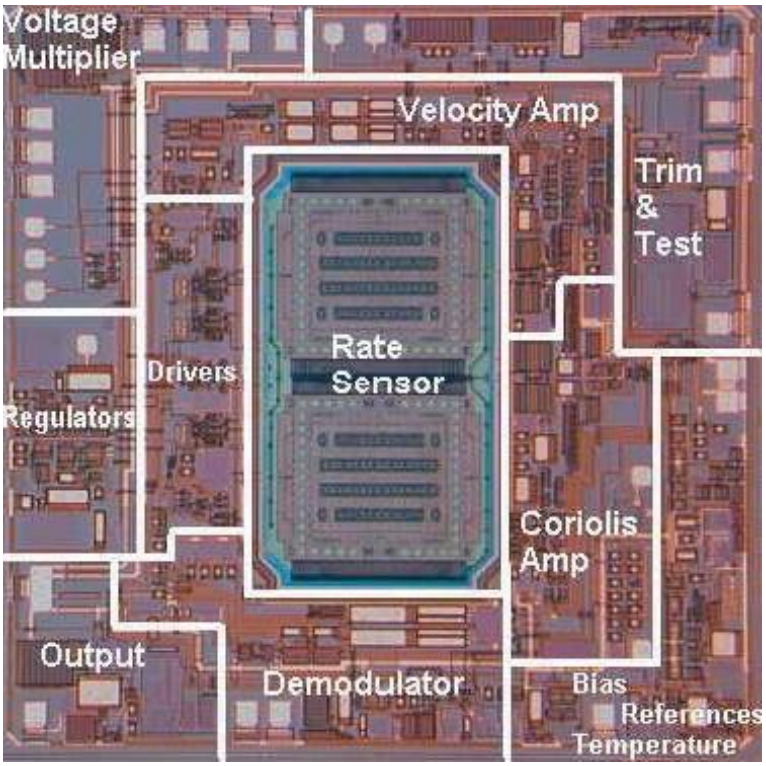

Figure 1.14: Die view of iMEMS ADXRS gyroscope produced by Analog Devices [25].

There is a tuning-fork mechanical structure at the heart of iMEMS ADXRS, around which low-noise signal conditioning and control electronics are located. iMEMS ADXRS demonstrates a bias stability of ~50 º/h with an incredible minimum detectable sense mode motion of ~16 10^{-6} nm equivalent to a capacitance change of ~12 zF, owing to its superior dedicated electronics design.

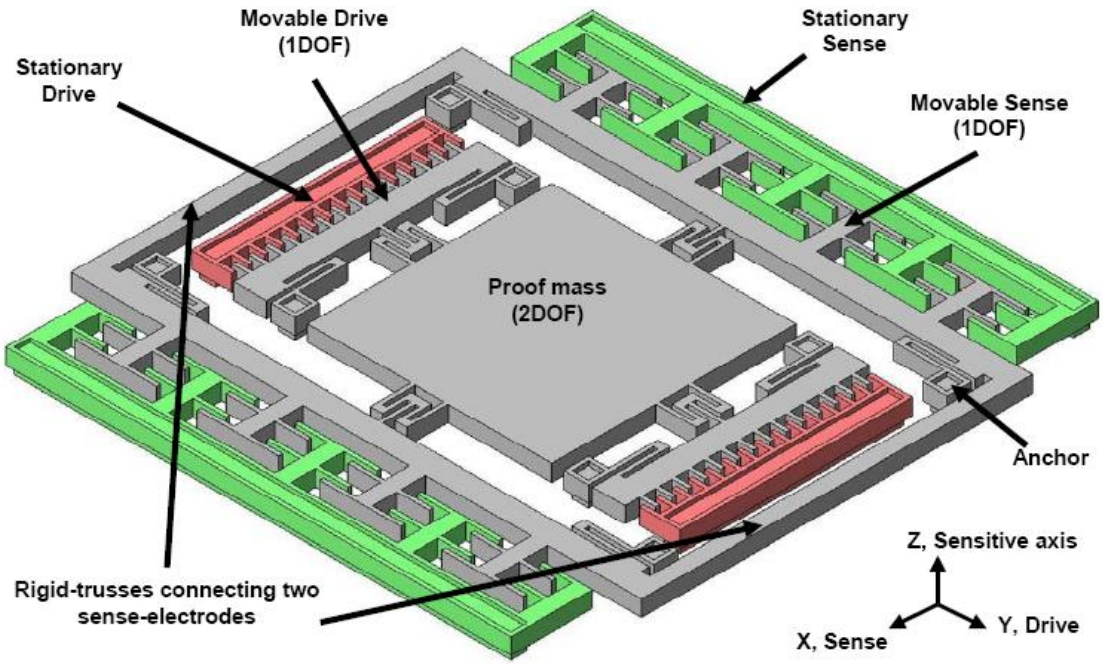

Figure 1.15: Schematic view of very low quadrature coupling symmetrical and decoupled gyroscope produced by METU [11].

METU-MEMS research group has also been working on micromachined gyroscopes since 1998. Through years, a number of gyroscopes have been fabricated in various micromachining processes, including nickel electroforming, silicon-on-insulator (SOI), dissolved wafer, and SOG processes [7, 8, 10, 11, 13]. The main emphasis of the research is on producing symmetrical and decoupled structures. The aim of symmetrical structures is minimizing the dependence of gyroscope response to thermal variations by utilizing same type of flexible linkages in the drive and sense directions. Figure 1.15 shows the schematic view of the most recently reported symmetrical and decoupled gyroscope [11]. This gyroscope demonstrates an uncompensated quadrature coupling as low as 15 º/sec at 50 mTorr vacuum level,

owing to its improved decoupling mechanism. Recently, research in tuning-fork gyroscopes has also started at METU and the first reported design demonstrated a bias drift and angle random walk of 200 º/h and 5.47 $^{o}/\sqrt{h}$, respectively, while the g sensitivity was measured to be as low as 9.3 (º/h)/g [30]. In 2007 new closed-loop drive mode constant amplitude control and open-loop sense mode readout circuits are developed at METU-MEMS research group and the gyroscope tested with these advanced circuits show a bias drift of 14.3 º/h with an angle random walk of 0.126 $^{o}/\sqrt{h}$ [31].

1.4 Research Objectives and Thesis Organization

Main goal of this research is to develop a novel mechanical structure that demonstrates the advantages of force-feedback type gyroscopes, namely high mechanical sensitivity, wide bandwidth, and immunity to environment condition variations, shortly robustness, while eliminating the necessity of complex feedback electronics. More specific objectives of this research are listed as follows:

1. Analysis of mechanical principles lying behind vibratory gyroscope designs. Through the complete use of mechanics principles, dynamics of vibratory gyroscopes will be explained thoroughly and the nonlinearities originating from the dynamics of vibratory gyroscopes will be investigated.

2. Thorough theoretical analysis of 2 DoF sense mode gyroscopes and development of a novel 2 DoF sense mode mechanical oscillator intended to improve the mechanical sensitivity of the sense mode at the flat mechanical sensitivity region, resolving the SNR degradation problem of current 2 DoF sense mode gyroscope designs.

3. Electromechanical design of an environmentally robust, tuning-fork, mode-decoupled, high performance micromachined vibratory gyroscope based on the developed 2 DoF sense mode design concept, using analytical design

equations. The 3D model of the gyroscope will be generated according to the dimensional parameters extracted during analytical design.

4. Verification of the analytical design through Finite Element Analysis (FEA) performed on the 3D model. Main FEA simulations will be modal analyses to verify the correct operation of drive and sense mode oscillators, temperature dependent modal analysis to verify the temperature robustness of the design, static deflection analyses to investigate the strengths and weaknesses of the design to acceleration loadings, and electrostatic analysis to extract the stray capacitances of the 3D structure.

5. Fabrication of the designed gyroscope using the in-house silicon-on-glass (SOG) micromachining process developed at METU Microelectronics facilities (METU-MET).

6. Characterization of the fabricated gyroscopes using the probe station. Then, the gyroscopes will be hybrid connected to external drive and sense mode electronics developed at METU MEMS-VLSI Research Group.

7. Verification of the design concept through characterizing the working prototypes in terms of bandwidth, scale factor, scale factor linearity, dependence of scale factor to ambient vacuum conditions, long term bias stability and angle random walk.

The organization of this thesis and summary of the following chapters are stated below.

Chapter 2 is devoted to theoretical study. First, it summarizes elementary mechanics principles useful in the design of a vibratory gyroscope. Next, it investigates the dynamics of a single degree of freedom drive and single degree of freedom sense mode vibratory gyroscope. Third, 2 DoF oscillator theory is presented and the proposed novel 2 DoF sense mode design will be demonstrated. Next, the dynamics of the proposed single degree of freedom drive and 2 DoF sense mode vibratory

gyroscope is investigated. Afterwards, electromechanical structures utilized in MEMS technology to implement a vibratory gyroscope are presented. Finally, secondary effects that are important in the design of a micromachined vibratory gyroscope are thoroughly investigated.

Chapter 3 presents the design of a mode-decoupled tuning-fork type gyroscope based on the novel 2 DoF sense mode oscillator design. This chapter also demonstrates verification of the analytical design through FEA simulations and explains the details of the fabrication process.

Chapter 4 deals with the verification of the proposed 2 DoF design concept by characterization of fabricated gyroscopes. It demonstrates the test procedures, the test setups and the electronic circuits used to characterize the fabricated gyroscopes. This chapter also summarizes the characterization results as bandwidth, scale factor, scale factor linearity, dependence of scale factor to ambient vacuum conditions, long term bias stability, and angle random walk.

Chapter 5 gives the conclusions, discusses the strengths and weaknesses of the new design, and presents future work to be performed so as to improve the performance of the designed gyroscope further.

CHAPTER 2

THEORETICAL STUDY

This chapter introduces the theoretical background upon which the electromechanical design of micromachined vibratory gyroscopes is built. Section 2.1 introduces kinematics of absolute motion, which will be followed by the presentation of dynamics of absolute motion and mechanical vibrations theory, which will be useful in the understanding of theoretical background lying behind the design of a vibratory gyroscopes. Section 2.2 deals with the application of elementary mechanics principles to 1 DoF drive and 1 DoF sense mode gyroscopes. Section 2.3 analyzes dynamics of 2 DoF sense mode oscillators. A novel 2 DoF oscillator design for gyroscope applications is proposed in this section. Strengths and weaknesses of the proposed design are also investigated in this section. Section 2.4 deals with the details of 1 DoF drive and 2 DoF sense mode gyroscopes. Implementation of a vibratory gyroscope using micromachining techniques is the subject of Section 2.5. Among the many electromechanical transduction methods like electromagnetic, electrostatic, piezoelectric; electrostatic actuation and sense techniques that are utilized in this research are demonstrated. Moreover, the flexible linkages used in place of springs and frictionless rollers are also presented in this section. This chapter is finalized in Section 2.6 by the introduction of secondary effects that should be of concern in the design of micromachined vibratory gyroscopes. The inherent nonlinearities of vibratory gyroscope dynamics is presented in this section in addition to the electrostatic spring phenomena observed in varying-gap type capacitive comb structures, quadrature coupling, and consideration of mechanical-thermal noise appearing in the electrical signal output of MEMS gyroscopes.

2.1 Elementary Mechanics Principles

2.1.1 Kinematics of Absolute Motion

In order to demonstrate the working principles of a vibratory gyroscope, it is necessary to start with the kinematics of a point P, fixed on a rigid body rotating around point O [32], as shown in Figure 2.1. In this figure *X*-*Y* frame is the fixed reference frame and *x*-*y* is the reference frame rotating with the rigid body at a speed of $\dot{\theta} = \vec{\varpi} = \varpi\, \hat{k}$, with the unit vectors $\hat{I}$-$\hat{J}$ and $\hat{\imath}$-$\hat{\jmath}$, respectively.

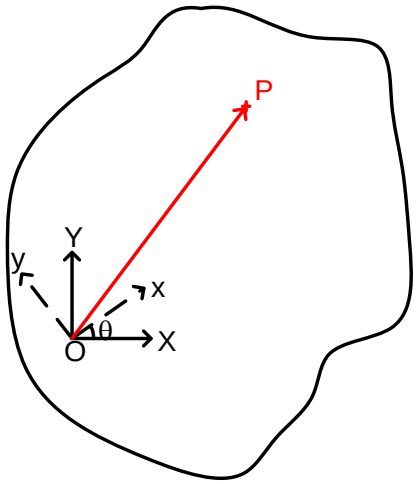

Figure 2.1: A rigid body rotating around point O.

Equations 2.1 and 2.2 represent the position of P with respect to the fixed and rotating reference frames, respectively.

$$\vec{r_P} = X\,\hat{I} + Y\,\hat{J} \tag{2.1}$$

$$\vec{r_P} = x\,\hat{\imath} + y\,\hat{\jmath} \tag{2.2}$$

Equations 2.3 and 2.4 describe the velocity of point P with respect to observers sitting on the fixed reference frame and on the rotating reference frame, respectively.

$$\vec{v_P} = \dot{X}\,\hat{I} + X\,\dot{\hat{I}} + \dot{Y}\,\hat{J} + Y\,\dot{\hat{J}} = \dot{X}\,\hat{I} + \dot{Y}\,\hat{J} \tag{2.3}$$

$$\vec{v_P} = \dot{x}\,\hat{\imath} + x\,\dot{\hat{\imath}} + \dot{y}\,\hat{\jmath} + y\,\dot{\hat{\jmath}} = 0 \tag{2.4}$$

The result of the velocity equation with respect to the stationary observer is due to the fact that, unit vectors $\hat{I}$ and $\hat{J}$ are constant vectors fixed to *X*-*Y* frame but the *X* and Y coordinates of point P are functions of time, due to the rotation of the body. The velocity with respect to the stationary observer sitting on the fixed reference frame is called the *absolute velocity*. On the other hand, both the unit vectors $\hat{\imath}$-$\hat{\jmath}$ and the coordinates *x*-*y* are constant according to the observer sitting on the rotating reference frame, resulting in the observer to see point P at rest. This result is an expected consequence of this velocity to be measured relative to the rotating reference frame. It is called the *relative velocity*.

An important equation is obtained when the absolute motion of point P is represented using the rotating coordinate system. In this case the position equation will be the same as Equation 2.2 but the velocity of the point will be as shown in Equation 2.5.

$$\overrightarrow{v_P} = \dot{x}\,\hat{\imath} + x\,\dot{\hat{\imath}} + \dot{y}\,\hat{\jmath} + y\,\dot{\hat{\jmath}} = x\,\dot{\hat{\imath}} + y\,\dot{\hat{\jmath}} \tag{2.5}$$

For this situation, although *x*-*y* coordinates of the point P are constant with respect to the rotating coordinate system, the unit vectors $\hat{\imath}$-$\hat{\jmath}$ are rotating with respect to the observer on the fixed reference frame. Therefore, the time derivatives of those unit vectors are to be found in order to simplify Equation 2.5. In order to find those derivates, firstly the unit vectors $\hat{\imath}$-$\hat{\jmath}$ are represented in terms of constant unit vectors $\hat{I}$ and $\hat{J}$ in Equations 2.6 and 2.7.

$$\hat{\imath} = cos\theta\,\hat{I} + sin\theta\,\hat{J} \tag{2.6}$$

$$\hat{\jmath} = -sin\theta\,\hat{I} + cos\theta\,\hat{J} \tag{2.7}$$

Equations 2.8 and 2.9 are obtained when the time derivatives of Equations 2.6 and 2.7 are taken, keeping in mind that $\hat{I}$ and $\hat{J}$ are constant unit vector.

$$\dot{\hat{\imath}} = \dot{\theta}\,\hat{\jmath} = \vec{\omega} \times \hat{\jmath} \tag{2.8}$$

$$\dot{\hat{\jmath}} = -\dot{\theta}\,\hat{\imath} = \vec{\omega} \times \hat{\imath} \tag{2.9}$$

The velocity expression is obtained by inserting Equation 2.8 and Equation 2.9 in Equation 2.5.

$$\overrightarrow{v_P} = x\,\dot{\hat{\imath}} + y\,\dot{\hat{\jmath}} = x\,(\vec{\omega} \times \hat{\jmath}) + y(\vec{\omega} \times \hat{\imath}) = \vec{\omega} \times (x\,\hat{\imath} + y\,\hat{\jmath}) = \vec{\omega} \times \overrightarrow{r_P} \tag{2.10}$$

Equation 2.10 demonstrates the well known relation between the angular velocity vector $\vec{\omega}$, and the linear velocity vector $\overrightarrow{v_P}$ which is tangent to the circle that position vector $\overrightarrow{r_P}$ traces during the course of its motion. The linear acceleration of point P is derived in Equation 2.11 using the results from Equations 2.8 and 2.9

$$\begin{aligned}\overrightarrow{a_P} &= \dot{\vec{\omega}} \times (x\,\hat{\imath} + y\,\hat{\jmath}) + \vec{\omega} \times \left(\vec{\omega} \times (x\,\hat{\imath} + y\,\hat{\jmath})\right) \\ &= \dot{\vec{\omega}} \times \overrightarrow{r_P} + \vec{\omega} \times (\vec{\omega} \times \overrightarrow{r_P}) = \underbrace{\dot{\vec{\omega}} \times \overrightarrow{r_P}}_{\substack{\text{tangential} \\ \text{acceleration}}} - \underbrace{\omega^2\,\overrightarrow{r_P}}_{\substack{\text{centripetal} \\ \text{acceleration}}}\end{aligned} \tag{2.11}$$

Tangential acceleration term appearing in Equation 2.11 is due to the change of the magnitude of linear velocity vector $\overrightarrow{v_P}$. On the other hand, *centripetal acceleration* term arises from the change of direction of the velocity vector $\overrightarrow{v_P}$. The velocity and acceleration terms of P are illustrated in Figure 2.2.

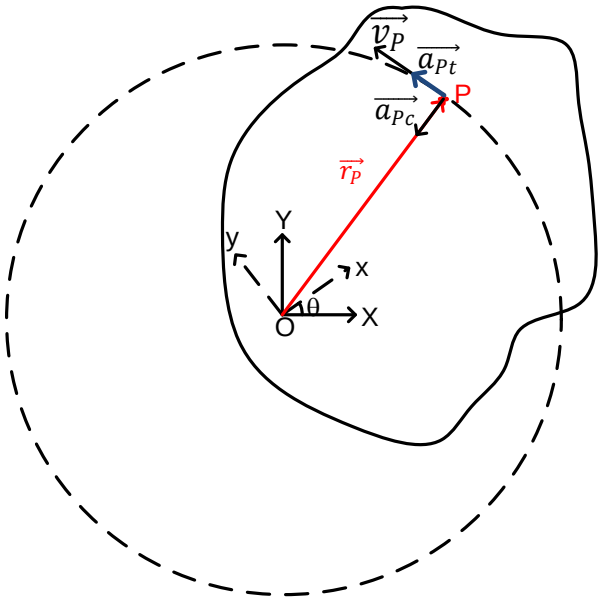

Figure 2.2: The velocity and acceleration terms of P.

Next, it is necessary to investigate the motion of a particle p located at point P at time t, moving on a rigid body that is making both translation and rotation with respect to a fixed reference frame with origin O′ as shown in Figure 2.3.

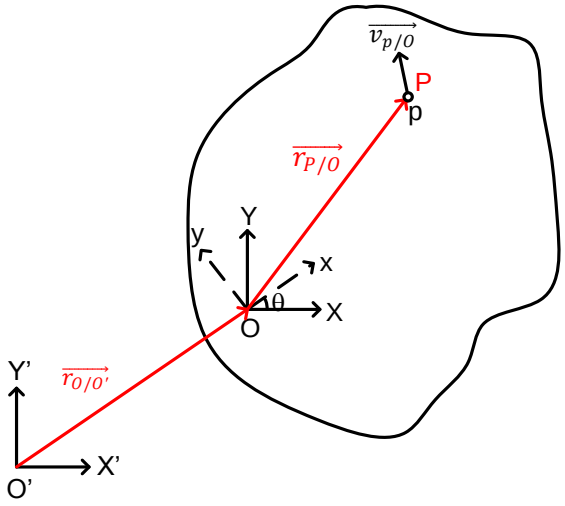

Figure 2.3: Particle p located at point P at time t, moving on a rigid body that is making both translation and rotation with respect to a fixed reference frame with origin O′.

Equations 2.12, 2.13, and 2.14 express the absolute position, the absolute velocity and the absolute acceleration vectors of particle p, respectively depending on the reasoning obtained from Equations 2.6 and 2.7.

$$\overrightarrow{r_{p/O'}} = \overrightarrow{r_{O/O'}} + \overrightarrow{r_{p/O}} \tag{2.12}$$

$$\overrightarrow{v_{p/O'}} = \overrightarrow{v_{O/O'}} + \overrightarrow{v_{p/O}} + \vec{\omega} \times \overrightarrow{r_{P/O}} \tag{2.13}$$

$$\begin{aligned}\overrightarrow{a_{p/O'}} &= \overrightarrow{a_{O/O'}} + \overrightarrow{a_{p/O}} + \vec{\omega} \times \overrightarrow{v_{P/O}} + \dot{\vec{\omega}} \times \overrightarrow{r_{P/O}} + \vec{\omega} \times \overrightarrow{v_{P/O}} + \vec{\omega} \times \left(\vec{\omega} \times \overrightarrow{r_{P/O}}\right) \\ &= \underbrace{\overrightarrow{a_{O/O'}}}_{1} + \underbrace{\overrightarrow{a_{p/O}}}_{2} + \underbrace{2\,\vec{\omega} \times \overrightarrow{v_{P/O}}}_{3} + \underbrace{\dot{\vec{\omega}} \times \overrightarrow{r_{P/O}}}_{4} + \underbrace{\vec{\omega} \times \left(\vec{\omega} \times \overrightarrow{r_{P/O}}\right)}_{5}\end{aligned} \tag{2.14}$$

Table 2.1 gives the physical explanations of the acceleration terms in absolute acceleration equation of particle p.

Table 2.1: Physical explanations of the acceleration terms in absolute acceleration equation of particle p.

1	Translational acceleration of rigid body with respect to the fixed reference frame having origin O'.
2	Translational acceleration of particle p with respect to the moving reference frame O attached to the rigid body.
3	*Coriolis acceleration* due firstly to the orientation change of the velocity vector of particle p, generated by the rotation of the rigid body, and secondly to the change of tangential velocity of particle p, generated by its motion with respect to frame O attached to the rigid body.
4	Tangential acceleration of point P fixed to the rigid body, due to the angular acceleration of the rigid body with respect to frame O.
5	Centripetal acceleration of point P fixed to the rigid body, due to the change of direction of the velocity vector.

Coriolis acceleration is first figured out by the French scientist Gaspard Gustave de Coriolis [33] in 1835, and is responsible for the energy coupling between the drive and sense mode oscillators of a vibratory gyroscope, as stated in Section 1.1.

2.1.2 Dynamics of Absolute Motion

Newton's first law of motion states that, in the absence of external forces an object at rest remains at rest, and an object in motion continues its motion with constant velocity. This law is also called the law of inertia, as the tendency of an object to resist any attempt to change its velocity is called the *inertia* of the object. From Newton's first law of motion an *inertial reference frame* or a *Newtonian reference frame* is defined as a reference frame that is fixed or making translatory motion with constant velocity.

Newton's second law of motion states that, the acceleration of an object with respect to an inertial reference frame is directly proportional to the resultant force acting on it, where the mass of the object is the proportionality constant as given in Equation 2.15.

$$\vec{F} = m\vec{a} \tag{2.15}$$

Newton's second law of motion should be redefined while making dynamics calculations if a non-inertial reference frame, such as a rotating reference frame, is used in the representation of the motion of a particle [34]. Equation 2.16 demonstrates second law of motion for the particle p of Figure 2.3.

$$\vec{F} - m\left(2\,\vec{\omega} \times \overrightarrow{v_{P/O}} + \dot{\vec{\omega}} \times \overrightarrow{r_{P/O}} + \vec{\omega} \times \left(\vec{\omega} \times \overrightarrow{r_{P/O}}\right)\right) = m\left(\overrightarrow{a_{O/O'}} + \overrightarrow{a_{p/O}}\right) \tag{2.16}$$

Right hand side of Equation 2.16 includes the translational acceleration term with respect to O' for particle p, while the other acceleration terms are passed to the left hand side as fictitious forcing terms, so called *inertial forces* in literature.

2.1.3 Mechanical Vibrations Theory

Figure 2.4 shows the schematic view and the free body diagram of a mass-spring-damper system, the simplest mechanical oscillator, with *m* representing the mass, *k* representing the spring constant, and *c* representing the damping constant of the system [35]. The free body diagram is drawn using D'Alembert's principle and assuming $\dot{x}(t) > 0$.

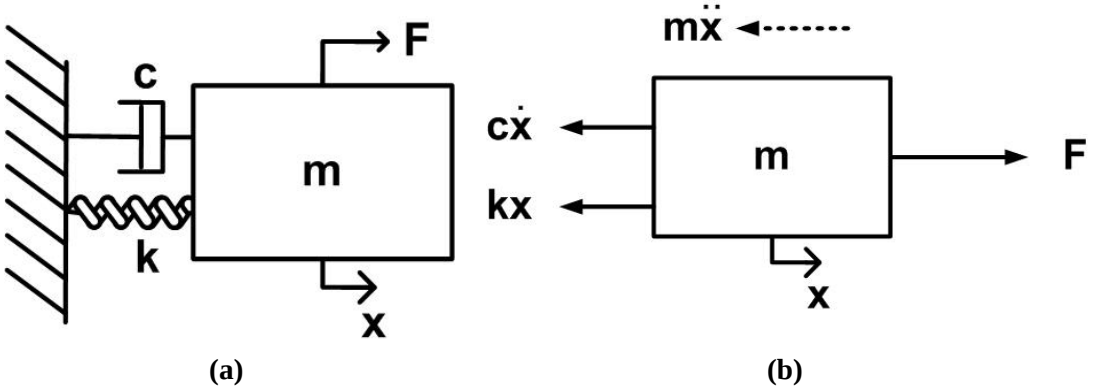

Figure 2.4: The (a) schematic view and the (b) free body diagram of a mass-spring-damper system.

Equations 2.17 and 2.18 represent the equation of motion for the system shown in Figure 2.4.

$$m\ddot{x}(t) + c\dot{x}(t) + kx(t) = F(t) \tag{2.17}$$

$$\ddot{x}(t) + 2\zeta\omega_n\dot{x}(t) + {\omega_n}^2 x(t) = \frac{1}{m}F(t) \tag{2.18}$$

In Equation 2.18, $\zeta = \frac{c}{2\sqrt{km}}$ is defined as the *damping ratio*, the ratio of the system damping to the critical damping, and $\omega_n = \sqrt{\frac{k}{m}}$ is defined as the *natural frequency* of the system. The steady state performance is of concern for micromachined vibratory gyroscopes, as the sensor system starts generating electrical measurement signals after the transients decay in practice. Therefore, it is necessary to work on the theory of forced mechanical vibrations. In mechanical vibrations theory, it is customary to assume a sinusoidal forcing function, not only because most of the physical forces are harmonic in nature, but also any other type of forcing can be expressed as sum of sinusoids using Fourier series expansion. Equation 2.19 expresses equation of motion for a forcing function of $F = F_o\, cos\omega t$ in time domain, while Equation 2.20 expresses the same equation in frequency domain by the use of Fourier transformation.

$$\ddot{x}(t) + 2\zeta\omega_n\dot{x}(t) + {\omega_n}^2 x(t) = \frac{F_o}{m} cos\Omega t \tag{2.19}$$

$$X(j\omega)(-\omega^2 - j2\zeta\omega_n\omega + {\omega_n}^2) = \frac{F_o}{m}\, Re\{e^{j\Omega t}\} \tag{2.20}$$

At this point it is important to note that, for a forcing in the form of a sinus function the same equation will hold true with the forcing part being imaginary, as the system is a linear time invariant (LTI) system. Making some mathematical manipulations, the system can be simplified into the form given in Equations 2.21 and 2.22, where $|G(j\omega)|$ is the *response amplification factor* and Φ is the *phase angle* between the applied force and displacement response. Equation 2.25 is obtained by taking the inverse Fourier transform.

$$X(j\omega) = \frac{F_o}{k} \frac{1}{\sqrt{\left[\left(1-\frac{\omega^2}{{\omega_n}^2}\right)^2 + 4\zeta^2\frac{\omega^2}{{\omega_n}^2}\right]}\, e^{\,j\,tan^{-1}\left(\frac{-2\zeta\frac{\omega}{\omega_n}}{1-\frac{\omega^2}{{\omega_n}^2}}\right)}} \tag{2.21}$$

$$X(j\omega) = \frac{F_o}{k}\ |G(j\omega)|\, e^{-j\Phi} \tag{2.22}$$

$$|G(j\omega)| = \frac{1}{\sqrt{\left[\left(1-\frac{\omega^2}{{\omega_n}^2}\right)^2 + 4\zeta^2\frac{\omega^2}{{\omega_n}^2}\right]}} \tag{2.23}$$

$$\Phi = tan^{-1}\left(\frac{-2\zeta\frac{\omega}{\omega_n}}{1-\frac{\omega^2}{{\omega_n}^2}}\right) \tag{2.24}$$

$$x(t) = \frac{F_o}{k}\ |G(j\omega)|\, cos(\Omega t - \Phi) \tag{2.25}$$

For a mechanical oscillator, the frequency at which the displacement response amplitude maximizes is called the *resonance frequency*, or the *damped natural frequency* of the system. It is necessary to solve Equation 2.27 which is the simplified form of Equation 2.26 for frequency, in order to find the resonance frequency of the system under investigation. Equation 2.28 demonstrates the resonance frequency of the system.

$$\frac{d|G(j\omega)|}{dr} = 0 \tag{2.26}$$

$$4\zeta^2 = 2\left(1-\left(\frac{\omega}{\omega_n}\right)^2\right) \tag{2.27}$$

$$\omega_r = \omega_n\sqrt{1-2\zeta^2} \tag{2.28}$$

The response amplification factor and the phase difference at resonance frequency can be determined by inserting ω_r in Equations 2.23 and 2.24.

$$|G(j\omega)| = \frac{1}{\sqrt{\left[\left(1-\frac{{\omega_n}^2\,(1-2\zeta^2)}{{\omega_n}^2}\right)^2 + 4\zeta^2\frac{{\omega_n}^2\,(1-2\zeta^2)}{{\omega_n}^2}\right]}} = \frac{1}{\sqrt{[-4\zeta^4+4\zeta^2]}} = \frac{1}{2\zeta\sqrt{[1-\zeta^2]}} \tag{2.29}$$

$$\Phi = tan^{-1}\left(\frac{-2\zeta\frac{\omega_n\sqrt{1-2\zeta^2}}{\omega_n}}{1-\frac{\omega_n{}^2(1-2\zeta^2)}{\omega_n{}^2}}\right) = tan^{-1}\left(\frac{\sqrt{1-2\zeta^2}}{\zeta}\right) \quad (2.30)$$

For light damping condition of $\zeta \ll 1$, the resonance frequency will be very close to the natural frequency of the system, such that $\omega_r \cong \omega_n$. Therefore, Equations 2.29 and 2.30 can be simplified as follows.

$$|G(j\omega)| = \frac{1}{2\zeta} \quad (2.31)$$

$$\Phi = tan^{-1}\left(\sqrt{\frac{1}{\zeta^2}-2}\right) \cong \frac{\pi}{2}\ rad \quad (2.32)$$

Figure 2.5 illustrates a typical $|G(j\omega)|$ vs. ω plot. In this plot light damping condition is assumed ($\omega_r \cong \omega_n$) and *half power frequencies* ω_1 and ω_2 are figured out. Half power frequencies, or *3 dB frequencies* are the points at which the response amplification factor drops to $\frac{1}{\sqrt{2}}$ of its peak value as seen on the plot. The importance of half power frequency concept is that, $\omega_2 - \omega_1$ is defined as the *bandwidth (BW)* for any type of oscillator whether it is mechanical or electrical.

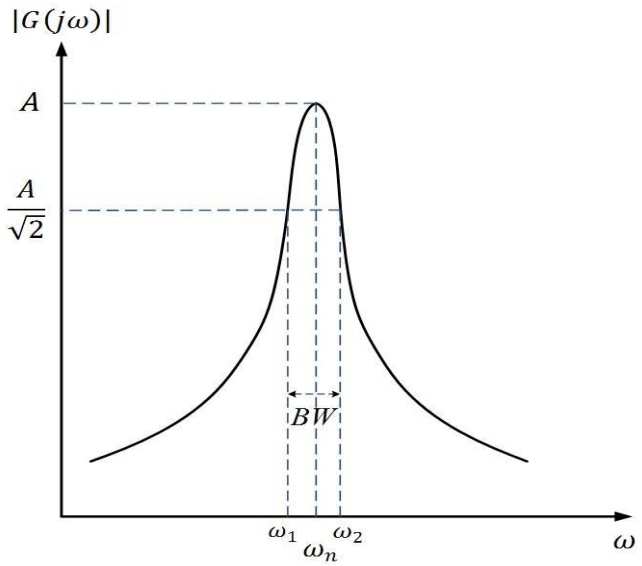

Figure 2.5: A typical |G(jω)| vs. ω plot.

Half power frequencies can be found by inserting ω_1 and ω_2 in Equation 2.23 considering the result obtained in Equation 2.31.

$$|G(j\omega)|_{\omega_{1,}\omega_2} = \frac{1}{2\sqrt{2}\zeta} = \frac{1}{\sqrt{\left[\left(1-\frac{{\omega_{1,2}}^2}{{\omega_n}^2}\right)^2 + 4\zeta^2\frac{{\omega_{1,2}}^2}{{\omega_n}^2}\right]}} \tag{2.33}$$

$$8\zeta^2 = \left(1-\frac{{\omega_{1,2}}^2}{{\omega_n}^2}\right)^2 + 4\zeta^2\frac{{\omega_{1,2}}^2}{{\omega_n}^2} \tag{2.34}$$

Equation 2.34 is a quadratic equation in terms of $\frac{{\omega_{1,2}}^2}{{\omega_n}^2}$, and its solution gives the half power frequencies as given in Equations 2.35 and 2.36.

$${\omega_1}^2 = \left(-2\zeta^2 + 1 - 2\zeta\sqrt{\zeta^2+1}\right){\omega_n}^2 \tag{2.35}$$

$${\omega_2}^2 = \left(-2\zeta^2 + 1 + 2\zeta\sqrt{\zeta^2+1}\right){\omega_n}^2 \tag{2.36}$$

Equation 2.37 is obtained by taking the difference of Equations 2.35 and 2.36, keeping in mind the definition of BW.

$$(\omega_2-\omega_1)(\omega_2+\omega_1) = BW\ (\omega_2+\omega_1) = \left(4\zeta\sqrt{\zeta^2+1}\right){\omega_n}^2 \tag{2.37}$$

For light damping condition, $\omega_n \cong \omega_1 \cong \omega_2$ assumption holds true such that $(\omega_2+\omega_1) = 2\omega_n$. Moreover, ζ^2 is so small that it can be neglected. Equation 2.39 expresses the BW of the oscillator.

$$BW\ 2\omega_n \cong 4\zeta{\omega_n}^2 \tag{2.38}$$

$$BW \cong 2\zeta\omega_n \tag{2.39}$$

Another important parameter for an oscillator is the quality factor, Q, and is defined as the ratio of the natural frequency to the bandwidth.

$$Q = \frac{\omega_n}{BW} \cong \frac{1}{2\zeta} \tag{2.40}$$

If Equation 2.25 is written for a sinusoidal forcing function with frequency equal to the resonance frequency with light damping condition, Equation 2.41 is obtained.

$$x(t) = \frac{F_o}{k}\ |G(j\omega)|\ cos(\Omega t - \Phi) = \frac{F_o}{k}\ \frac{1}{2\zeta}\ cos\left(\Omega t - \frac{\pi}{2}\right) = \frac{F_o}{k}\ Q\ cos\left(\Omega t - \frac{\pi}{2}\right) \qquad (2.41)$$

If the forcing term was a constant force with amplitude F_o for the system shown in Figure 2.4, then $\frac{F_o}{k}$ will be the static deflection of the mass. On the other hand, Equation 2.41 demonstrates the very important result such that, if a harmonic force at the resonance frequency is applied to the system, the dynamic displacement amplitude of the mass will be amplified by the quality factor Q. Moreover, it will be a harmonic function of the same form as the input force, but will display a 90º phase shift with respect to the harmonic forcing function.

2.2 Dynamics of 1 DoF Drive and 1 DoF Sense Mode Gyroscopes

Figure 2.6 displays the schematic view of a single mass vibratory gyroscope structure with proof mass *m*, spring constant in the drive direction k_d, damping in the drive direction c_d, spring constant in the sense direction k_s, and damping in the sense direction c_s.

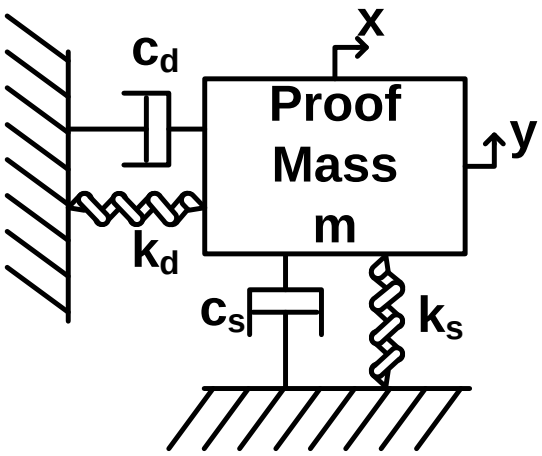

Figure 2.6: Schematic view of a single mass vibratory gyroscope structure.

Equations 2.42 and 2.43 express the dynamic equations describing the motion of the gyroscope in the drive (x) axis and the sense (y) axis, respectively, where a_{gs_x} and a_{gs_y} are the acceleration terms of the gyro frame with respect to the stationary frame. F_d and F_s are the external forces applied on the proof mass in the x and y directions, respectively. ϖ is the angular velocity, so called angular rate input applied to the gyro frame around the z direction, and $\dot{\varpi}$ (called α in the literature) is the angular acceleration, the rate of change of the angular velocity of the gyro frame with time.

$$m\left(\ddot{x} + a_{gs_x} - 2\varpi\dot{y} - \dot{\varpi}y - \varpi^2 x\right) + c_d\dot{x} + k_d x = F_d \tag{2.42}$$

$$m\left(\ddot{y} + a_{gs_y} + 2\varpi\dot{x} + \dot{\varpi}x - \varpi^2 y\right) + c_s\dot{y} + k_s y = F_s \tag{2.43}$$

If Equations 2.42 and 2.43 are inspected carefully, it can easily be concluded that they are the x and y components of Equation 2.16 applied for the proof mass instead of particle p of Figure 2.3. In micromachined vibratory gyroscopes the proof mass is forced to oscillate in the drive direction via F_d, and the oscillation amplitude in the sense direction due to the applied angular rate is measured. The angular velocity of the frame where the gyroscope is attached can be extracted this way. F_s is zero in open-loop sense mode gyroscopes. On the other hand, in closed-loop controlled sense mode gyroscopes, so called Force-Feedback type gyroscopes, F_s is the force applied to the sense mode oscillator so as to diminish the sense mode oscillations induced by Coriolis coupling.

It is better to put the forcing terms to the right hand side of the equations, in order to examine the dynamics of a gyroscope in more detail. Moreover, it is sufficient to start with an open-loop gyroscope, as the results obtained can easily be applied to a closed-loop gyroscope.

$$m\,\ddot{x} + c_d\dot{x} + k_d x = F_d - m\,(a_{gs_x} - 2\varpi\dot{y} - \dot{\varpi}y - \varpi^2 x) \tag{2.44}$$

$$m\ddot{y} + c_s\dot{y} + k_s y = -m\,(a_{gs_y} + 2\varpi\dot{x} + \dot{\varpi}x - \varpi^2 y) \tag{2.45}$$

In those equations the $-2m\varpi\dot{x}$ and $2m\varpi\dot{y}$ terms are the Coriolis coupling terms from the drive to sense and from sense to drive modes, respectively. Other forcing terms are originating from the angular and linear accelerations, in addition to higher order forcing terms that will show their effects mostly for high input rates.

Angular acceleration terms can be assumed to be negligibly small as designers are usually concerned with the steady state performances and slowly changing angular rates in micromachined vibratory gyroscopes. Moreover, using tuning fork structures one can get rid of the effects of linear acceleration terms, by differential sense mode readout electronics. On the other hand, it must be noted that the effects of angular acceleration and high order terms get doubled in tuning fork structures. Hence, it is suggested in this research that, a designer should consider those spurious effects more deeply while using tuning fork structures. There is another common assumption in vibratory gyroscope designs such that, in practical gyroscopes sense displacements are on the order of nanometers while drive displacements are on the order of micrometers, therefore Coriolis coupling from the sense to drive mode so called the inverse Coriolis coupling is negligible. On the other hand, inverse Coriolis coupling effect can be considerable if the drive mode resonance frequency is designed to be high, as the sense mode velocity is directly proportional to the frequency of drive mode oscillations.

Making the aforementioned assumptions, the gyroscope dynamics are modeled in the literature with the simplified equations given below.

$$m\,\ddot{x} + c_d\dot{x} + k_d x = F_d \tag{2.46}$$

$$m\ddot{y} + c_s\dot{y} + k_s y = -2m\,\varpi\dot{x} \tag{2.47}$$

Using simplified equations is always desirable in a design study, as this allows the designer to examine the design under consideration more deeply. The simplified dynamics equations make the design of vibratory gyroscopes possible, as the coupled-nonlinear differential equation set is impossible to solve using analytical methods. On the other hand, the effects of spurious forcing terms need to be

investigated numerically. Section 2.6.1 discusses the effects of spurious forcing terms in detail, through numerical simulations performed in Matlab Simulink environment.

Equations 2.48 and 2.49 express the drive mode displacement and velocity for a single DoF drive mode oscillator, respectively using the result obtained in Equation 2.41 with $F_d = F_0\, cos(\Omega t)$.

$$x(t) = \frac{F_0}{k_d}\, Q_d\, cos\left(\Omega t - \frac{\pi}{2}\right) = \frac{F_0}{c_d}\, \sqrt{\frac{m}{k_d}}\, cos\left(\Omega t - \frac{\pi}{2}\right) \tag{2.48}$$

$$\dot{x}(t) = -\Omega \frac{F_0}{c_d}\, \sqrt{\frac{m}{k_d}}\, sin\left(\Omega t - \frac{\pi}{2}\right) = \Omega \frac{F_0}{c_d}\, \sqrt{\frac{m}{k_d}}\, cos(\Omega t) \tag{2.49}$$

Equation 2.50 expresses the sense mode displacement with the same reasoning obtained from Equation 2.41, using the derived drive mode velocity expression.

$$y(t) = \frac{-2m\varpi\dot{x}(t)}{k_s}\, Q_s = \frac{-2m^2\varpi F_0\Omega}{c_s c_d}\, \sqrt{\frac{1}{k_s k_d}}\, cos(\Omega t) = \frac{2m^2\varpi F_0\Omega}{c_s c_d}\, \sqrt{\frac{1}{k_s k_d}}\, cos(\Omega t - \pi) \tag{2.50}$$

It is observed from Equations 2.48 and 2.50 that, sense mode displacement lags drive mode displacement by $\frac{\pi}{2}$ rad for matched-mode gyroscopes.

If the applied angular rate input to the gyroscope is a time varying function, like a sinusoid of $\varpi(t) = \varpi cos(\Omega_{in} t)$, the forcing due to Coriolis coupling f_c will have two terms as given in Equation 2.51. Hence, the sense mode response will be the sum of the two sinusoids expressed in Equation 2.52.

$$\begin{aligned} f_c(t) &= -2m\varpi(t)\dot{x}(t) = -2m\varpi\Omega \frac{F_0}{c_d}\, \sqrt{\frac{m}{k_d}}\, cos(\Omega t)\, cos(\Omega_{in} t) \\ &= -2m\varpi\Omega \frac{F_0}{c_d}\, \sqrt{\frac{m}{k_d}}\, \Big(cos\big((\Omega + \Omega_{in})t\big) + cos\big((\Omega - \Omega_{in})t\big)\Big) \end{aligned} \tag{2.51}$$

$$y(t) = \frac{-2m\varpi\dot{x}(t)}{k_s}\ Q_s = \frac{-2m^2\varpi F_0\Omega}{c_s c_d}\sqrt{\frac{1}{k_s k_d}}\left(cos\big((\Omega+\Omega_{in})t\big) + cos\big((\Omega-\Omega_{in})t\big)\right) \quad (2.52)$$

It is observed from Equation 2.52 that, sense mode response appears at frequencies of gyroscope operating frequency $\pm\,\Omega_{in}$, as shown in Figure 2.7. It is clear that the two sense response terms have different amplitudes for a near matched-mode gyroscope. Moreover, applied angular rate inputs with same amplitudes but different frequencies will result in completely different vibration responses in the sense mode. For a perfectly mode-matched gyroscope the two sense response terms will have same amplitudes but sense mode response to angular rate inputs with same amplitudes but different frequencies will be significantly different both for matched-mode and near-matched mode gyroscopes.

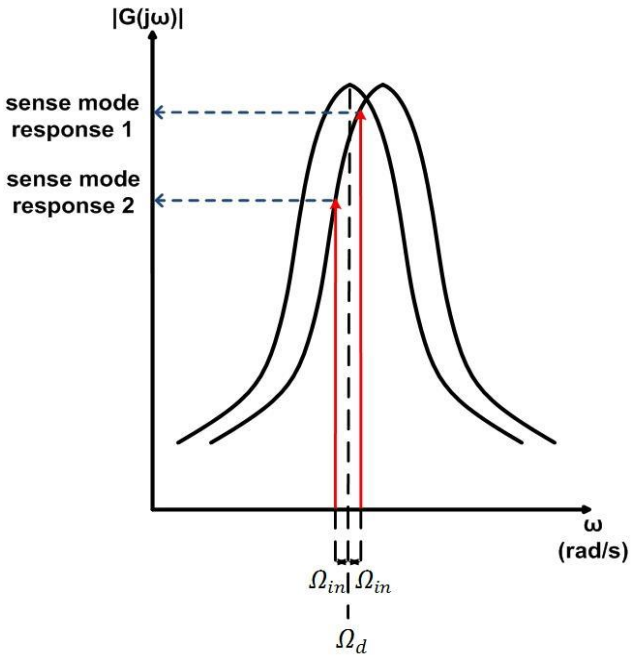

Figure 2.7: Sense mode response to time varying angular rate input of a single DoF drive and single DoF sense mode gyroscope.

2.3 2 DoF Sense Mode Oscillators

As mentioned in Section 1.2 gyroscopes utilizing 2 DoF sense mode oscillators showing improved bandwidth and robustness have already been reported. In this

section already reported 2 DoF sense mode oscillator is discussed, and a novel 2 DoF sense mode oscillator showing an improved mechanical sensitivity at the flat-band region with only a small reduction in operation bandwidth is proposed.

2.3.1 Dynamics of Previously Reported 2 DoF Sense Mode Oscillator

Figure 2.8 illustrates the schematic view of the previously reported 2 DoF sense mode oscillator structure [17, 23, 24] with the proof mass m_1, which is excited by force f_c due to Coriolis acceleration, second mass m_2 connected to the proof mass generating the second degree of freedom, spring constants k_1 and k_2, and damping factors c_1, c_2 and c_3.

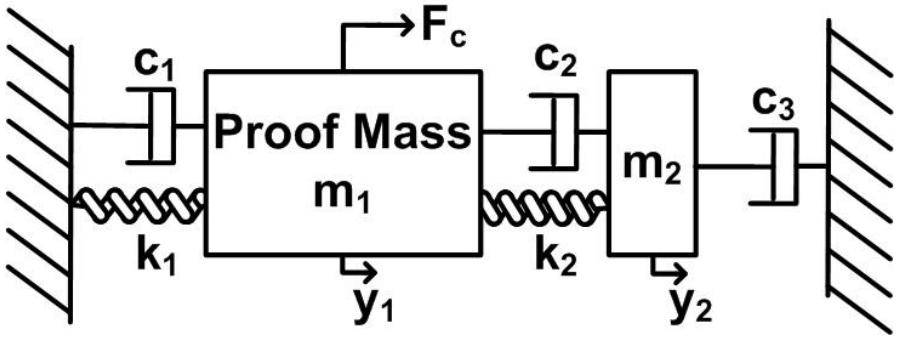

Figure 2.8: Schematic view of the previously reported 2 DoF sense mode oscillator of a vibratory MEMS gyroscope.

Equations 2.53 and 2.54 express the dynamic equations describing the motion of the two masses in the sense direction.

$$m_1 \ddot{y}_1 + (c_1 + c_2)\dot{y}_1 + (k_1 + k_2)y_1 - c_2\dot{y}_2 - k_2 y_2 = f_c \quad (2.53)$$

$$m_2 \ddot{y}_2 + (c_2 + c_3)\dot{y}_2 + k_2 y_2 - c_2\dot{y}_1 - k_2 y_1 = 0 \quad (2.54)$$

Using matrix formulation is more informative in analysis of multi degree of freedom vibratory systems, therefore dynamic equations of motion are generally written in matrix form as $[M]\{\ddot{y}\} + [C]\{\dot{y}\} + [K]\{y\} = \{f\}$. Equation 2.55 expresses the equations of motion for the system of Figure 2.8 in matrix form.

$$\begin{bmatrix} m_1 & 0 \\ 0 & m_2 \end{bmatrix} \{\ddot{y}\} + \begin{bmatrix} c_1 + c_2 & -c_2 \\ -c_2 & (c_2 + c_3) \end{bmatrix} \{\dot{y}\} + \begin{bmatrix} k_1 + k_2 & -k_2 \\ -k_2 & k_2 \end{bmatrix} \{y\} = \begin{Bmatrix} f_c \\ 0 \end{Bmatrix} \quad (2.55)$$

A 2 DoF system has two natural frequencies. In order to find the natural frequencies of the system, it is meaningful to consider the system with zero damping matrix and a zero forcing vector as damping introduced to the system cannot change the natural frequencies, and the natural frequencies are defined for free vibrations. Therefore, it is sufficient to examine the system $[M]\{\ddot{y}\} + [K]\{y\} = 0$ to find the natural frequencies. For this kind of a set of differential equations, the response vector $\{y\}$ should be sinusoidal such as $\{y\} = \{Y\}\sin(\varpi t)$, implying the condition that, $\{\ddot{y}\} = -\varpi^2\{y\}$. Hence, the equation can be rewritten as given in Equation 2.56

$$\left[[K] - \varpi^2[M]\right]\{Y\}\sin(\varpi t) = 0 \quad (2.56)$$

When the resulting equation is investigated, there is only the trivial solution of $\{Y\} = 0$, meaning there is no vibration, if $\left[[K] - \varpi^2[M]\right]$ matrix is nonsingular. On the other hand, a set of linearly dependent solutions can be found if $\left[[K] - \varpi^2[M]\right]$ is singular. This singularity implies the determinant $|[K] - \varpi^2[M]|$ to be equal to zero.

$$\begin{vmatrix} (k_1 + k_2) - m_1\varpi^2 & -k_2 \\ -k_2 & k_2 - m_2\varpi^2 \end{vmatrix} = 0 \quad (2.57)$$

The characteristic equation of the system is extracted as in Equation 2.58 from Equation 2.57.

$$k_1k_2 - \varpi^2k_2m_1 - \varpi^2k_1m_2 - \varpi^2k_2m_2 + \varpi^4m_1m_2 = 0 \quad (2.58)$$

The roots of the characteristic equation give the most important physical properties of a 2 DoF oscillator, namely the natural frequencies of the system, as given in Equations 2.59 and 2.60.

$$\varpi_{n1} = \sqrt{\frac{k_1 m_2 + k_2(m_1 + m_2) - \sqrt{4k_1 k_2 m_1 m_2 + (k_1 m_2 + k_2(m_1 + m_2))^2}}{2m_1 m_2}} \tag{2.59}$$

$$\varpi_{n2} = \sqrt{\frac{k_1 m_2 + k_2(m_1 + m_2) + \sqrt{4k_1 k_2 m_1 m_2 + (k_1 m_2 + k_2(m_1 + m_2))^2}}{2m_1 m_2}} \tag{2.60}$$

On the other hand, these equations are too complex to use in a design study. Equations 2.53 and 2.54 introduce two new parameters $\varpi_{m1}$and ϖ_{m2}, that are to be used in obtaining more meaningful design equations.

$$\varpi_{m1} = \sqrt{\frac{k_1}{m_1}} \tag{2.61}$$

$$\varpi_{m2} = \sqrt{\frac{k_2}{m_2}} \tag{2.62}$$

Those two constants are physically representing the natural frequencies of the two mass-spring oscillators if they are not interconnected. Equations 2.63 and 2.64 demonstrate the natural frequencies of the system in terms of ϖ_{m1}, ϖ_{m2} , k_2, and m_1 obtained by some mathematical manipulations.

$$\varpi_{n1} = \sqrt{\frac{k_2 + m_1({\varpi_{m1}}^2 + {\varpi_{m2}}^2) - \sqrt{{k_2}^2 + {m_1}^2({\varpi_{m1}}^2 - {\varpi_{m2}}^2)^2 + 2k_2 m_1({\varpi_{m1}}^2 + {\varpi_{m2}}^2)}}{2m_1}} \tag{2.63}$$

$$\varpi_{n2} = \sqrt{\frac{k_2 + m_1({\varpi_{m1}}^2 + {\varpi_{m2}}^2) + \sqrt{{k_2}^2 + {m_1}^2({\varpi_{m1}}^2 - {\varpi_{m2}}^2)^2 + 2k_2 m_1({\varpi_{m1}}^2 + {\varpi_{m2}}^2)}}{2m_1}} \tag{2.64}$$

Equations 2.63 and 2.64 define the bandwidth of the gyroscope, BW and the *mid-band frequency,* ϖ_{mid} .

$$BW = \varpi_{n2} - \varpi_{n1} \tag{2.65}$$

$$\varpi_{mid} = \frac{\varpi_{n1} + \varpi_{n2}}{2} \tag{2.66}$$

After finding the natural frequencies, the next characteristic to consider in a design study is the displacement response of the system to a force input. Equation 2.55 should be solved in order to obtain the displacement responses. It is customary to assume a forcing function in the form of $f_c = F_c(\varpi)e^{j\varpi t}$, not only because forcing functions of MEMS vibratory gyroscopes are sinusoidal, but also any other forcing function can be written as sum of sinusoids by using Fourier Series expansion. The response to a harmonic forcing will also be harmonic, and will be of the form $\{y\} = \{Y(j\varpi)\}e^{j\varpi t}$. Then, Equation 2.55 can be rewritten as shown below.

$$\begin{bmatrix} -m_1\varpi^2 + j\varpi(c_1+c_2) + (k_1+k_2) & -j\varpi c_2 - k_2 \\ -j\varpi c_2 - k_2 & -m_2\varpi^2 + j\varpi(c_2+c_3) + k_2 \end{bmatrix} \{Y(\varpi)\}e^{j\varpi t} = \begin{Bmatrix} F_c(\varpi) \\ 0 \end{Bmatrix} e^{j\varpi t} \tag{2.67}$$

By solving Equation 2.67, the ratio of the displacement responses to the force inputs, so called the receptance frequency response functions (FRF) in literature [36] can be obtained.

$$\frac{Y_1(\varpi)}{F_c(\varpi)} = \frac{-j\varpi(c_2+c_3) - k_2 + \varpi^2 m_2}{(-j\varpi c_2 - k_2)^2 - (j\varpi(c_1+c_2) + k_1 + k_2 - \varpi^2 m_1)(j\varpi(c_2+c_3) + k_2 - \varpi^2 m_2)} \tag{2.68}$$

$$\frac{Y_2(\varpi)}{F_c(\varpi)} = \frac{-j\varpi c_2 - k_2}{(-j\varpi c_2 - k_2)^2 - (j\varpi(c_1+c_2) + k_1 + k_2 - \varpi^2 m_1)(j\varpi(c_2+c_3) + k_2 - \varpi^2 m_2)} \tag{2.69}$$

Table 2.2: Mechanical design parameters of a gyroscope with a 2 DoF sense mode oscillator.

$m_1 = 100\ \mu g$
$m_2 = 100\ \mu g$
$k_1 = 1000\ N/m$
$k_2 = 1000\ N/m$
$\varpi_{m1} = 100000\ rad/s$
$\varpi_{m2} = 100000\ rad/s$
$c_1 = c_2 = c_3 = 2.5 * 10^{-7}\ Ns/m$

In order to achieve inertial-grade performance, a mode-matched gyroscope employing quality factors >30000, proof mass >100μg and drive mode oscillation

amplitude >5μm is required according to [9]. Table 2.2 lists the mechanical design parameters of a gyroscope with a 2 DoF sense mode for which the magnitude and phase receptance FRF's are demonstrated in Figure 2.9 through Figure 2.12. The design parameters are chosen to be in coincidence with the requirements given in [9], so that a comparison between a mode-matched gyroscope and the 2 DoF sense mode design can be possible.

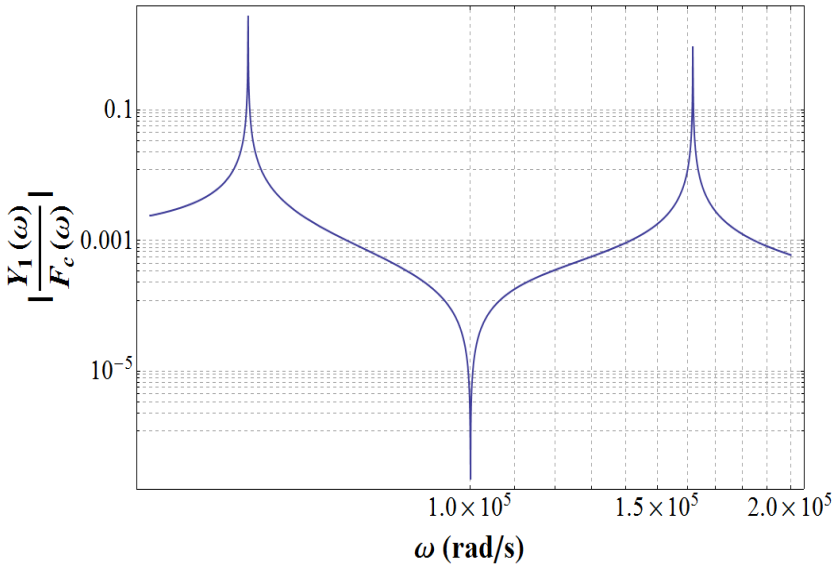

Figure 2.9: Magnitude Receptance FRF for m_1.

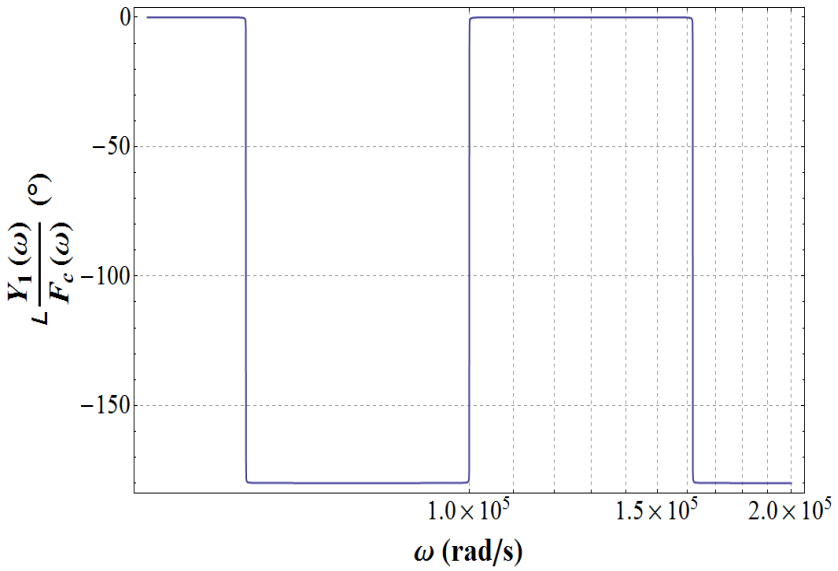

Figure 2.10: Phase Receptance FRF for m_1.

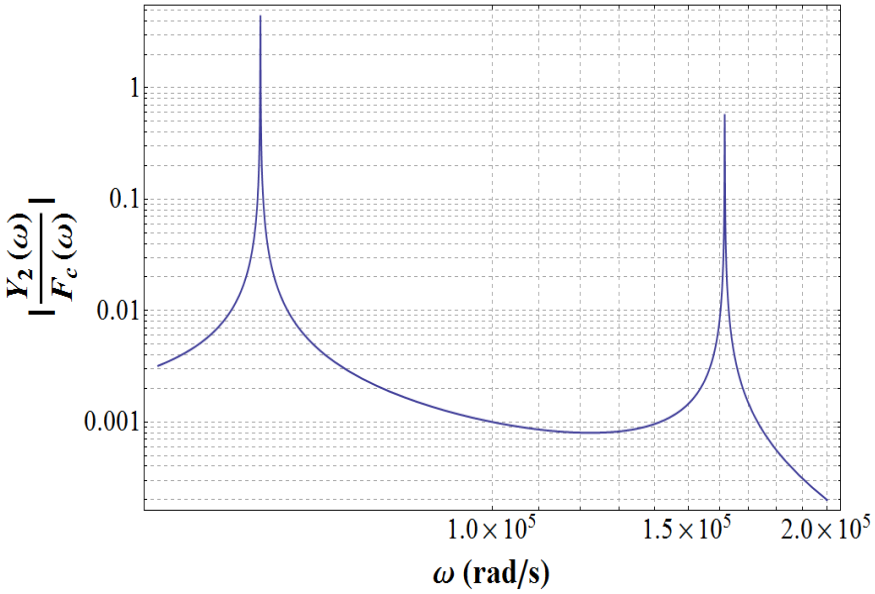

Figure 2.11: Magnitude Receptance FRF for m_2.

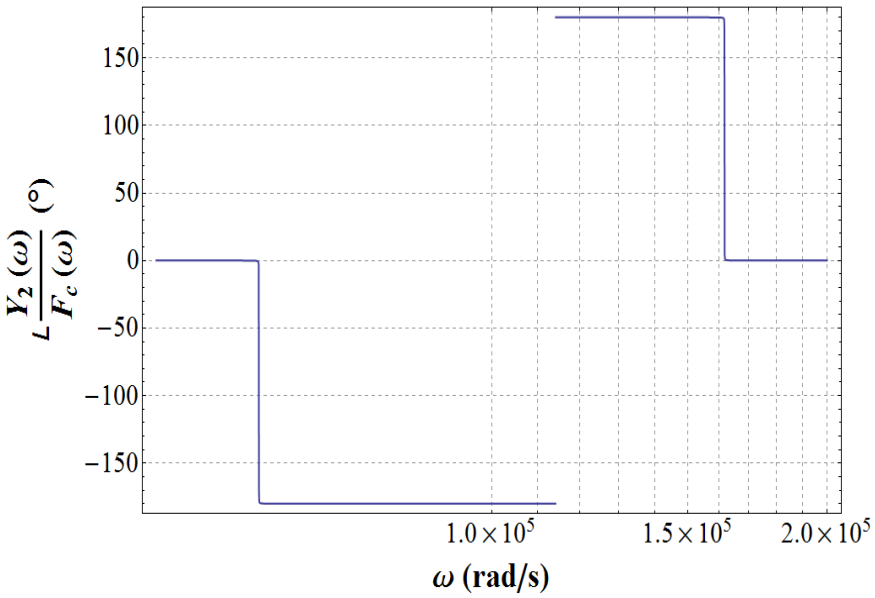

Figure 2.12: Phase Receptance FRF for m_2.

It is observed from the calculated FRF's that m_2 displacement response demonstrates a valley between the two peaks occurring at the natural frequencies ϖ_{n1} and ϖ_{n2}. The bandwidth and mid-band receptance magnitude of this response can be adjusted by varying the mechanical parameters. On the other hand, m_1 displacement response has a very sharp decrease between the two natural

frequencies and does not possess a useful flat-band region. In today's machinery this configuration is used for vibration absorption such that, a rotating machine with mass imbalance causing a harmonic force on m_1 is prevented from vibrating by connecting it to m_2, which absorbs the vibration energy and keeps the vibration amplitude of m_1 at minimum.

Next, the displacement response of m_2 should be optimized so as to obtain maximum attainable mid-band receptance magnitude with sufficient bandwidth, so that mechanical sensitivity of the gyroscope to applied angular rates is maximized, improving SNR performance of the gyroscope. 3D plots are obtained using Mathematica in order to examine the effects of mechanical parameters on the performance. Figure 2.13 demonstrates variation of the bandwidth with varying ϖ_{m1} and ϖ_{m2}, for constant k_2 and m_1.

From Figure 2.13 it can be observed that, the bandwidth decreases to its minimum value when ϖ_{m1} is designed to be equal to ϖ_{m2}, while it increases with the increasing difference between ϖ_{m1} and ϖ_{m2}.

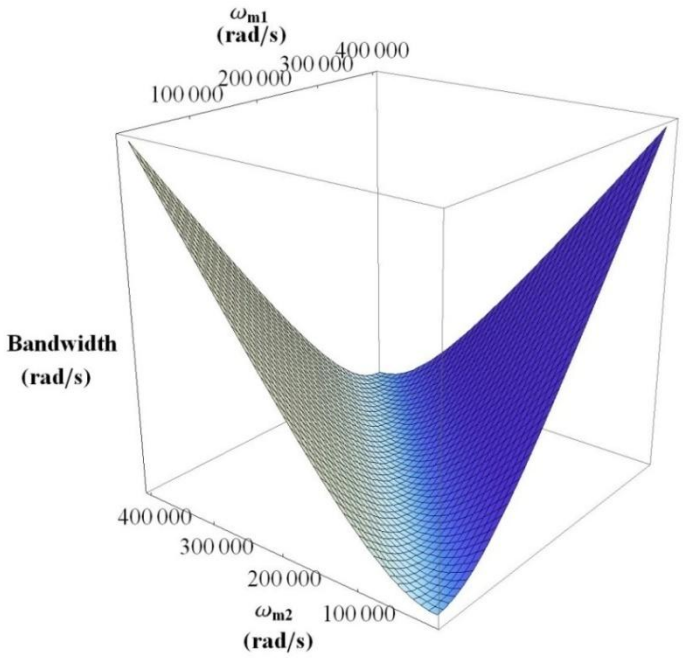

Figure 2.13: Variation of bandwidth with varying ω_{m1} and ω_{m2} for constant for constant k_2 and m_1.

Figure 2.14 demonstrates variation of the mid-band receptance magnitude with varying k_2 and m_1, for constant ϖ_{m1} and ϖ_{m2}.

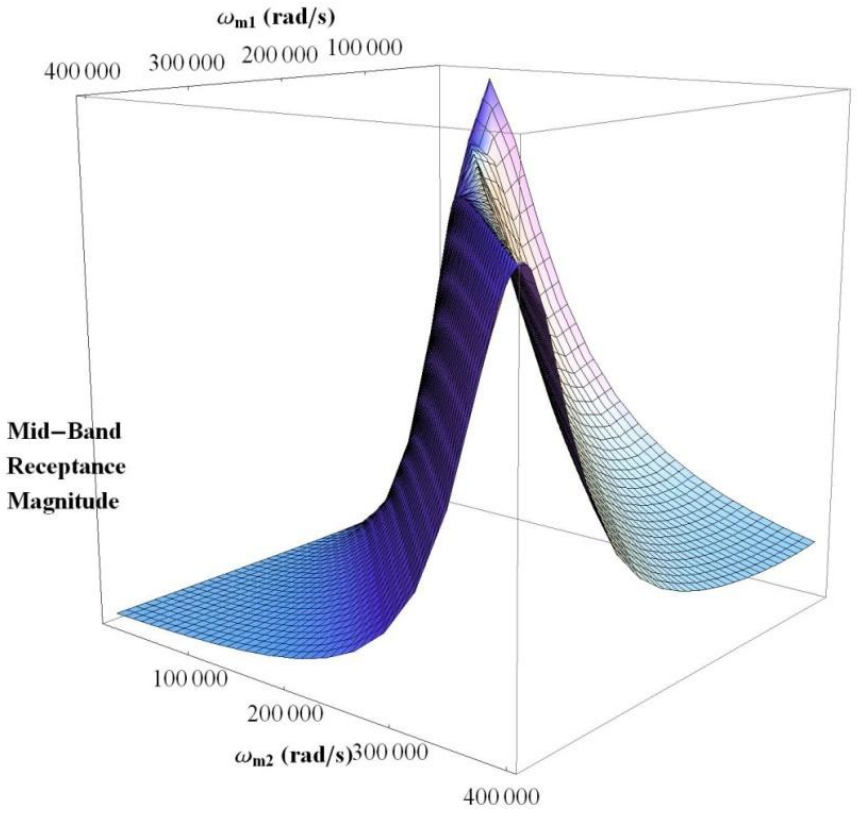

Figure 2.14: Variation of mid-band receptance magnitude with varying k_2 and m_1, for constant ω_{m1} and ω_{m2}.

From Figure 2.14 it can be deduced that, when ϖ_{m1} is designed to be equal to ϖ_{m2} the mid-band receptance magnitude, therefore, the mechanical sensitivity of the gyroscope can be maximized. On the other hand, the introduction of any difference between ϖ_{m1} and ϖ_{m2} decreases the mid-band receptance magnitude. Therefore, there is a trade-off between the bandwidth and sensitivity of the gyroscope. On the other hand, a bandwidth of >>100 Hz which is sufficient for inertial-grade operation can be obtained with a gyroscope satisfying $\varpi_{m1} = \varpi_{m2}$ condition. Hence, in this design study ϖ_{m1} is taken to be equal to ϖ_{m2}.

After $\varpi_{m1} = \varpi_{m2}$ condition is decided, the effects of k_2 and m_1 on the bandwidth and mid-band receptance magnitude for constant $\varpi_{m1} = \varpi_{m2}$ should be investigated. Figure 2.15 demonstrates variation of the bandwidth with varying k_2 and m_1 for constant ϖ_{m1} equal to ϖ_{m2}.

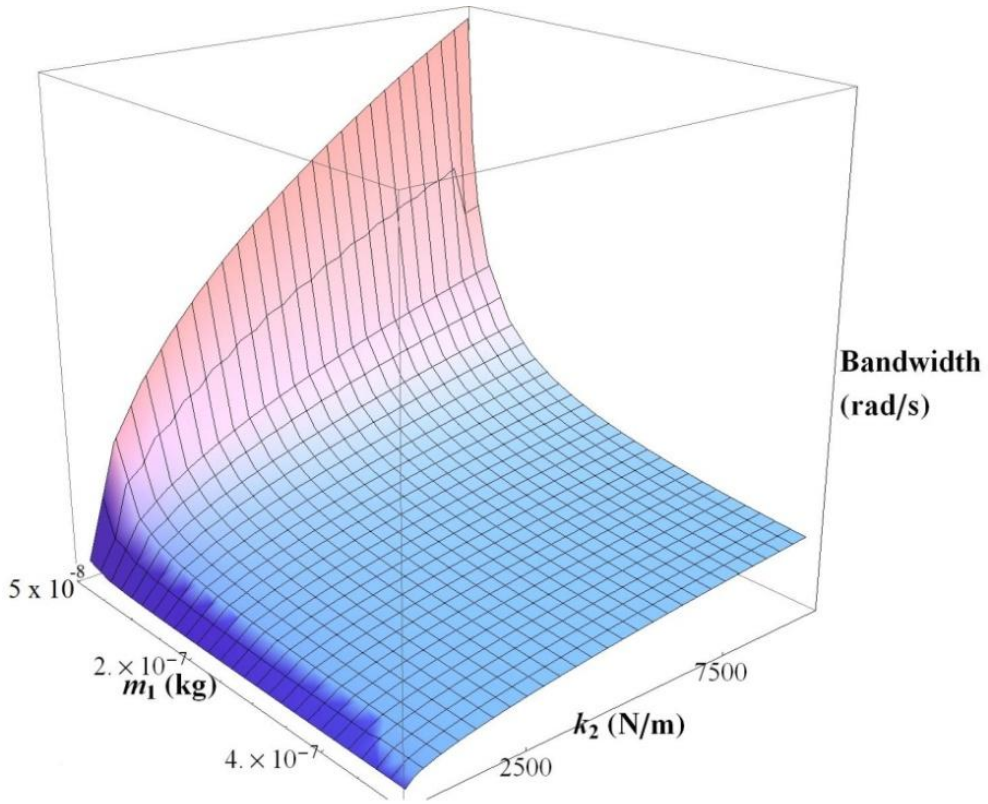

Figure 2.15: Variation of bandwidth with varying k_2 and m_1, for constant ω_{m1} equal to ω_{m2}.

From Figure 2.15 it can be concluded that, the bandwidth can be said to be independent of m_1, if m_1 is not designed to be too small. For very small m_1 values bandwidth is increasing sharply. On the other hand, bandwidth is significantly affected from the variation of k_2, and as k_2 increases an increasing bandwidth is observed. One more relation needs to be investigated before deciding the mechanical design parameter values. Figure 2.16 demonstrates variation of mid-band receptance magnitude with varying k_2 and m_1, for constant ϖ_{m1} equal to ϖ_{m2}.

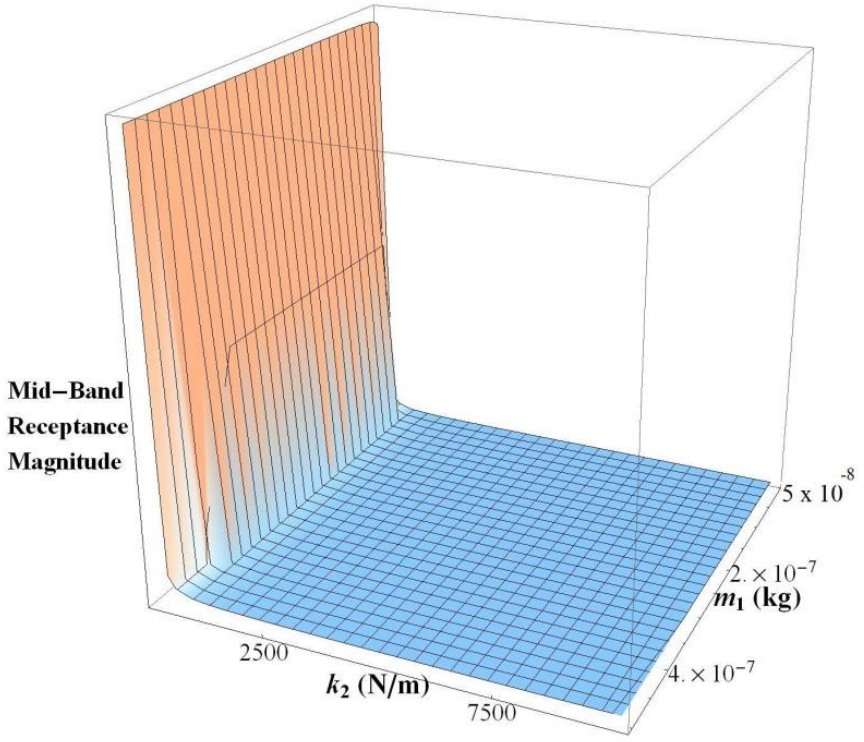

Figure 2.16: Variation of mid-band receptance magnitude with varying k_2 and m_1, for constant ω_{m1} equal to ω_{m2}

By investigating Figure 2.16 one of the most important results about the reported 2 DoF sense mode oscillator designs is obtained. Mid-band receptance magnitude is independent of m_1, but it diminishes very fast by increasing k_2. When Figure 2.15 and Figure 2.16 are inspected simultaneously, the spring constant range of 10-250 N/m for k_2, where both a sufficient bandwidth and a high mid-band receptance magnitude can be obtained seems to be the only range to be utilized in a design study. A spring with such a small spring constant can be fabricated with MEMS technology; on the other hand, $\varpi_{m1} = \varpi_{m2}$ requirement will then necessitate a very small m_2 value. The problem with a very small m_2 value is that it will significantly limit the number of capacitive plates attached to m_2 that will convert the mechanical displacement due to Coriolis coupling to electrical signal, resulting in a significant degradation in SNR performance of the gyroscope. Therefore, it is not possible to achieve a high-performance gyroscope using the previously reported 2 DoF sense mode oscillator design.

2.3.2 Dynamics of the Proposed 2 DoF Sense Mode Oscillator

A new 2 DoF sense mode oscillator is proposed in this research for the first time in literature in order to overcome the limitations set by the previous design [17, 23, 24]. Figure 2.17 illustrates the schematic view of the proposed 2 DoF sense mode oscillator, with the proof mass m_1 that is excited by force f_c due to Coriolis acceleration, second mass m_2 connected to the proof mass generating the second degree of freedom, spring constants k_1 , k_2 and, k_3 and damping factors c_1, c_2 and c_3.

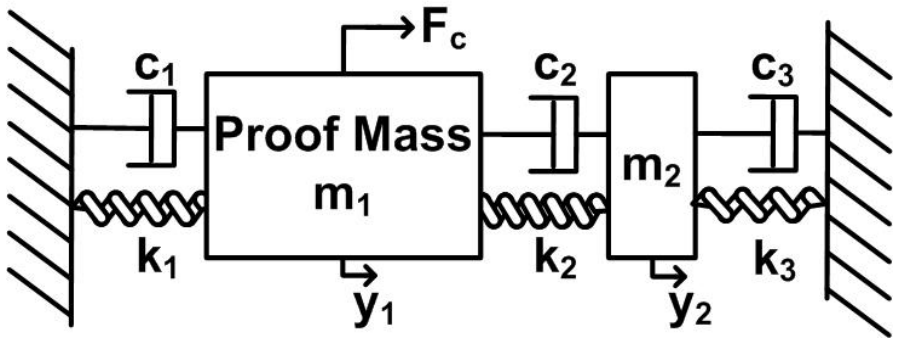

Figure 2.17: Schematic view of the proposed 2 DoF sense mode oscillator.

Equation 2.70 demonstrates the dynamics of the proposed design in matrix form.

$$\begin{bmatrix} m_1 & 0 \\ 0 & m_2 \end{bmatrix} \{\ddot{y}\} + \begin{bmatrix} c_1 + c_2 & -c_2 \\ -c_2 & (c_2 + c_3) \end{bmatrix} \{\dot{y}\} + \begin{bmatrix} k_1 + k_2 & -k_2 \\ -k_2 & k_2 + k_3 \end{bmatrix} \{y\} = \begin{Bmatrix} f_c \\ 0 \end{Bmatrix} \qquad (2.70)$$

Equations 2.71 and 2.72 define natural frequencies of the separate oscillators for this design.

$$\varpi_{m1} = \sqrt{\frac{k_1}{m_1}} \qquad (2.71)$$

$$\varpi_{m2} = \sqrt{\frac{k_2 + k_3}{m_2}} \qquad (2.72)$$

Equations 2.73 and 2.74 express the natural frequencies of the system by using the parameters defined in Equations 2.71 and 2.72.

$$\varpi_{n1} = \sqrt{\frac{k_2 + m_1({\varpi_{m1}}^2 + {\varpi_{m2}}^2) - \sqrt{\frac{{k_2}^2(4m_1 + m_2)}{m_2} + {m_1}^2({\varpi_{m1}}^2 - {\varpi_{m2}}^2)^2 + 2k_2m_1({\varpi_{m1}}^2 - {\varpi_{m2}}^2)}}{2m_1}} \tag{2.73}$$

$$\varpi_{n2} = \sqrt{\frac{k_2 + m_1({\varpi_{m1}}^2 + {\varpi_{m2}}^2) + \sqrt{\frac{{k_2}^2(4m_1 + m_2)}{m_2} + {m_1}^2({\varpi_{m1}}^2 - {\varpi_{m2}}^2)^2 + 2k_2m_1({\varpi_{m1}}^2 - {\varpi_{m2}}^2)}}{2m_1}} \tag{2.74}$$

For this structure ϖ_{m2} is defined in a form that, it includes the effect of parallel connection of k_2 and k_3. This definition results in a close similarity between the natural frequencies of previous and proposed designs.

Next, Equations 2.75 and 2.76 demonstrate the receptance FRF's for the improved design, from the solution of Equation 2.70.

$$\frac{Y_1(\varpi)}{F_c(\varpi)} = \frac{-j\varpi(c_2 + c_3) - k_2 - k_3 + \varpi^2 m_2}{(-j\varpi c_2 - k_2)^2 - (j\varpi(c_1 + c_2) + k_1 + k_2 - \varpi^2 m_1)(j\varpi(c_2 + c_3) + k_2k_2 + k_3 - \varpi^2 m_2)} \tag{2.75}$$

$$\frac{Y_2(\varpi)}{F_c(\varpi)} = \frac{-j\varpi c_2 - k_2}{(-j\varpi c_2 - k_2)^2 - (j\varpi(c_1 + c_2) + k_1 + k_2 - \varpi^2 m_1)(j\varpi(c_2 + c_3) + k_2 + k_3 - \varpi^2 m_2)} \tag{2.76}$$

The close similarity between the previous and proposed designs can be observed when the receptance FRF equations are investigated.

Figure 2.18 and Figure 2.19 demonstrate the variations of the bandwidth and mid-band receptance magnitude for varying ϖ_{m1} and ϖ_{m2} but constant m_1, m_2 and k_2, respectively.

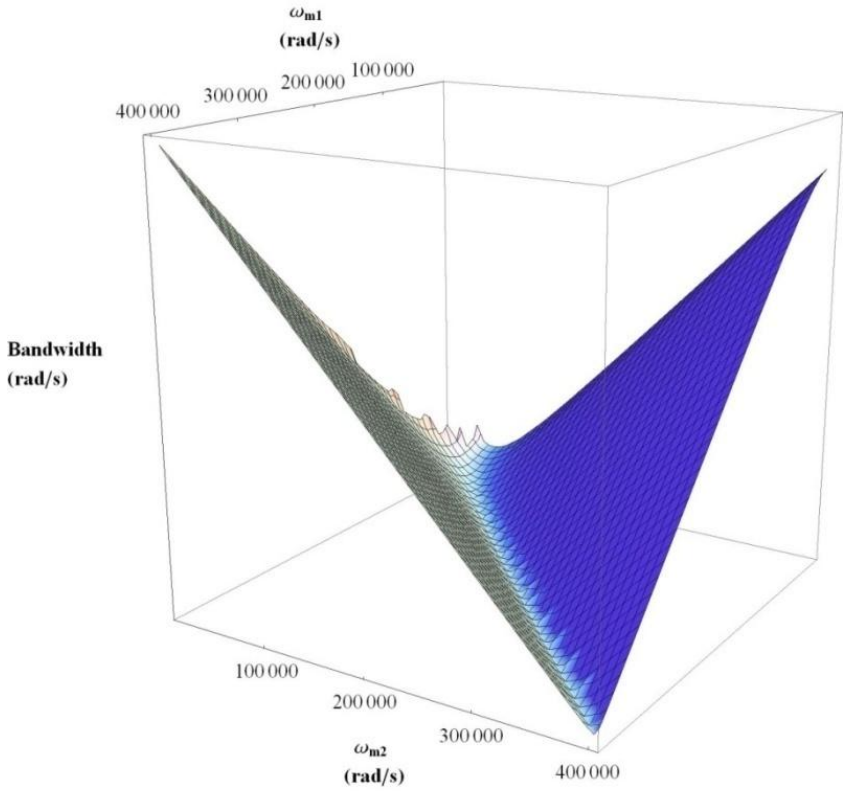

Figure 2.18: Variation of bandwidth due to varying ω_{m1} and ω_{m2}.

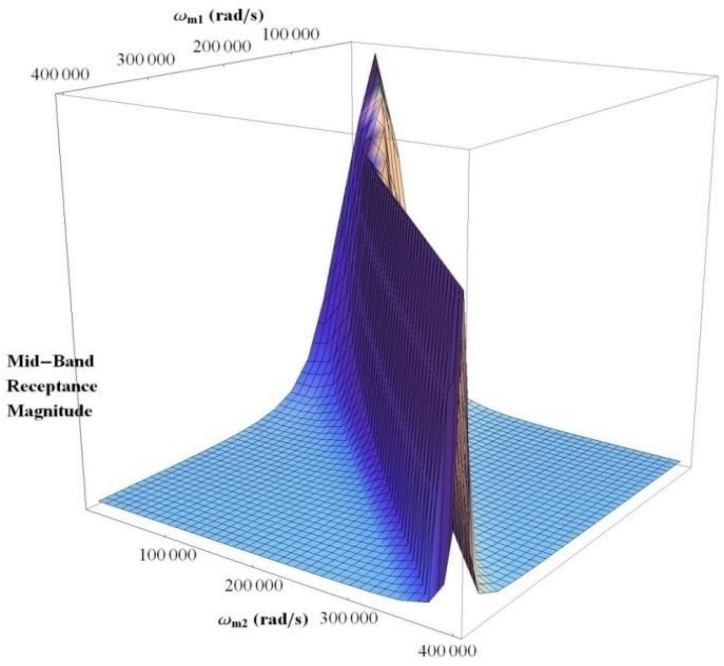

Figure 2.19: Variation of mid-band receptance magnitude due to varying ω_{m1} and ω_{m2}.

It is concluded that the condition $\varpi_{m1} = \varpi_{m2}$ is also necessary for the proposed design by investigating Figure 2.18 and Figure 2.19. Here the trade-off between bandwidth and mid-band receptance magnitude is more emphasized as the decrease in bandwidth and the increase in mid-band receptance magnitude are sharper than the previous design.

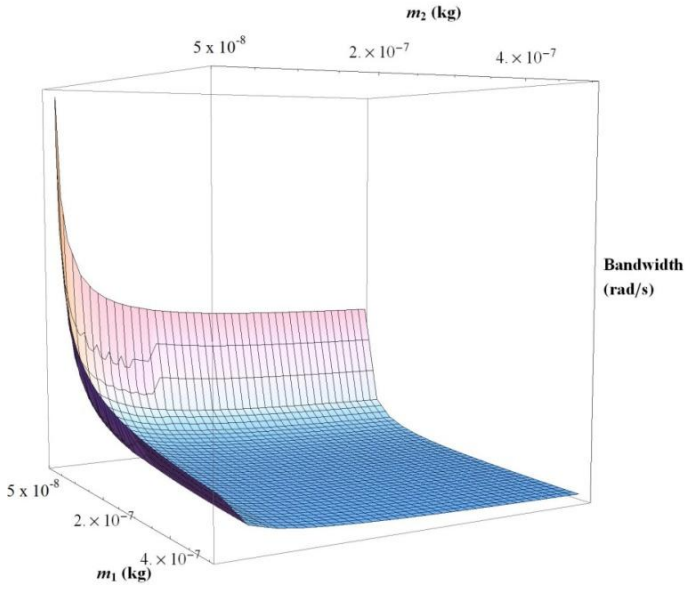

Figure 2.20: Variation of bandwidth due to varying m_1 and m_2.

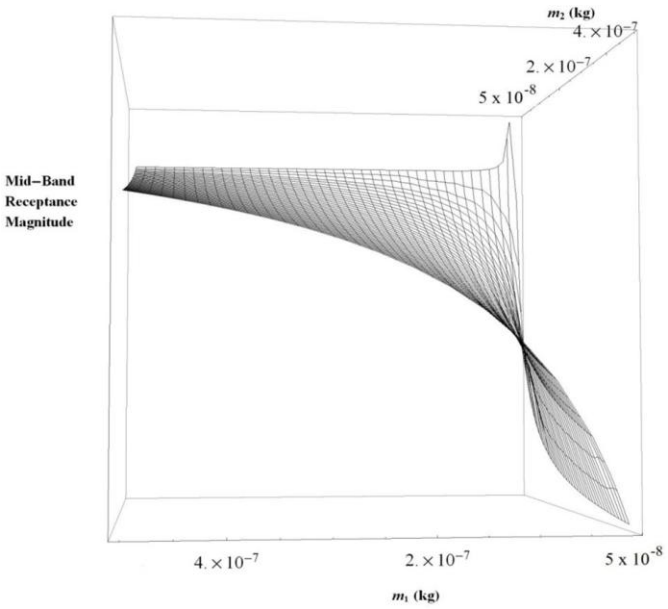

Figure 2.21: Variation of mid-band receptance magnitude due to varying m_1 and m_2.

Figure 2.20 and Figure 2.21 demonstrate variations of bandwidth and mid-band receptance magnitude for constant $\varpi_{m1} = \varpi_{m2}$ and k_2 but varying m_1 and m_2, respectively.

It is observed from Figure 2.20 that, a decline in m_2 generates an increase in bandwidth for a constant m_1, and vice versa. It is observed from Figure 2.21 that, the same situation is valid for mid-band receptance magnitude too. Hence, choosing an optimized value for $m_1 = m_2 = 100\ \mu g$ is reasonable in the design study.

Figure 2.22 and Figure 2.23 present relations of bandwidth and mid-band receptance magnitude to varying m_1 and k_2, respectively. it is observed from Figure 2.22 that, k_2 should be increased for increased bandwidth. On the other hand, it is observed from Figure 2.23 that, an increased k_2 value results in a degradation. The trade-off between bandwidth and sensitivity is emphasized once more.

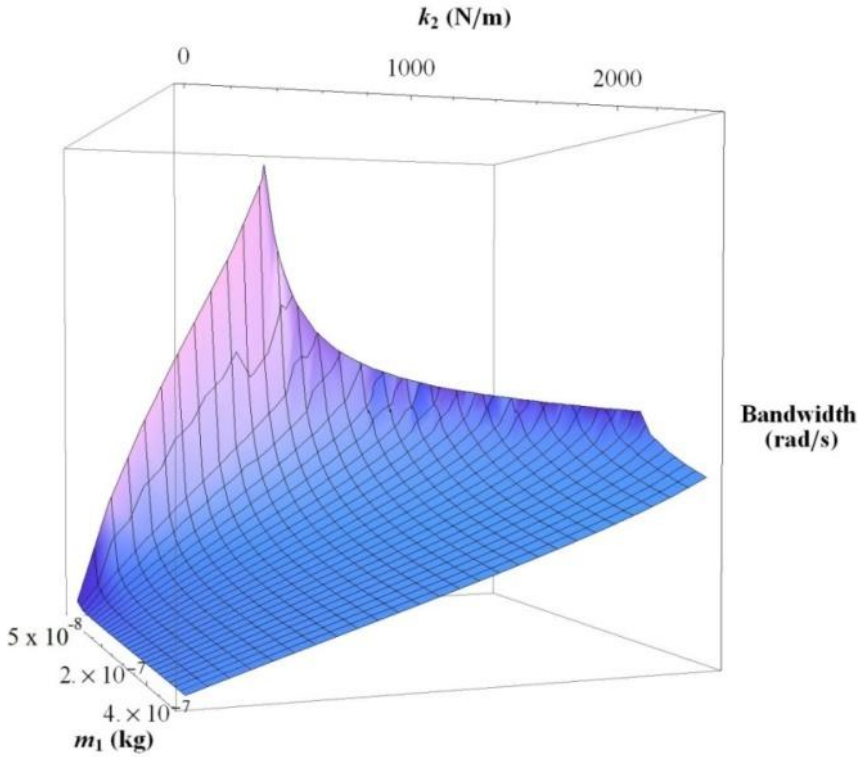

Figure 2.22: Variation of bandwidth due to varying m_1 and k_2.

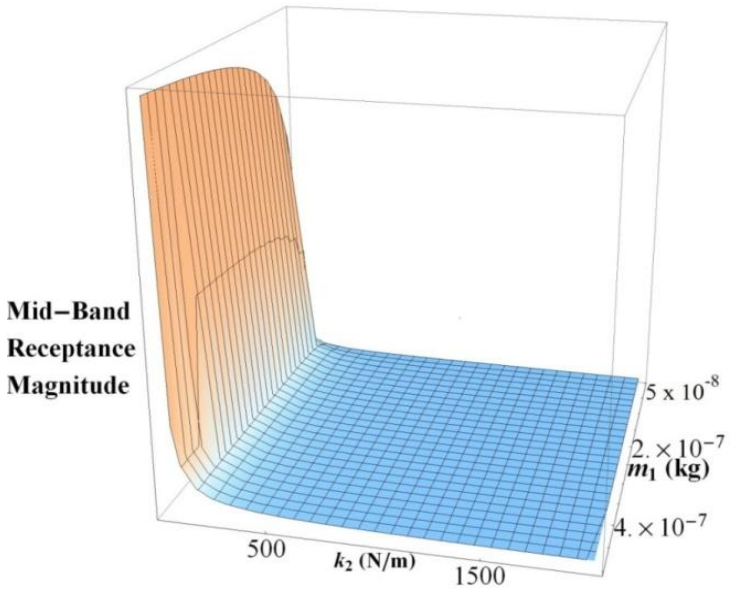

Figure 2.23: Variation of mid-band receptance magnitude due to varying m_1 and k_2.

Next, Figure 2.24 and Figure 2.25 demonstrate the relations of bandwidth and mid-band receptance to varying m_2 and k_2, respectively.

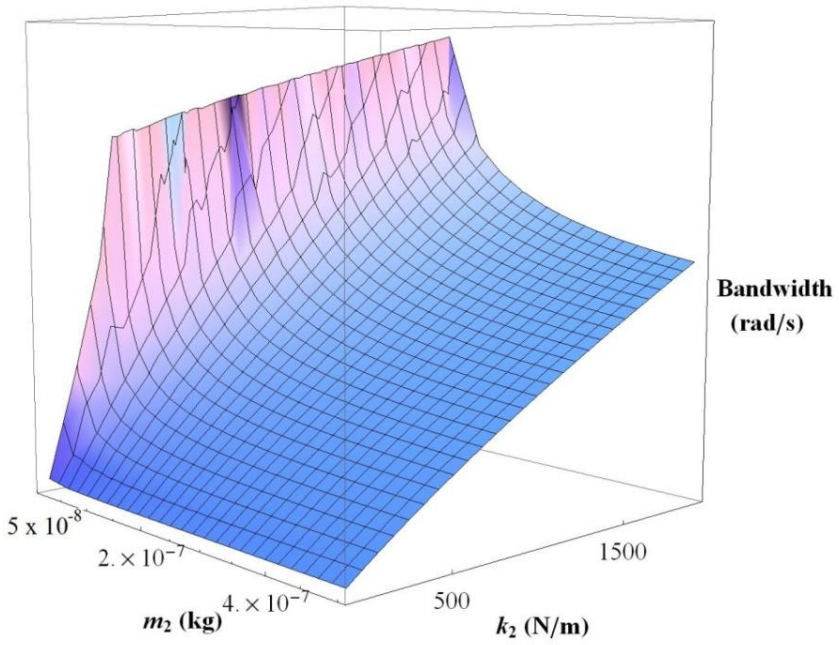

Figure 2.24: Variation of bandwidth due to varying m_2 and k_2.

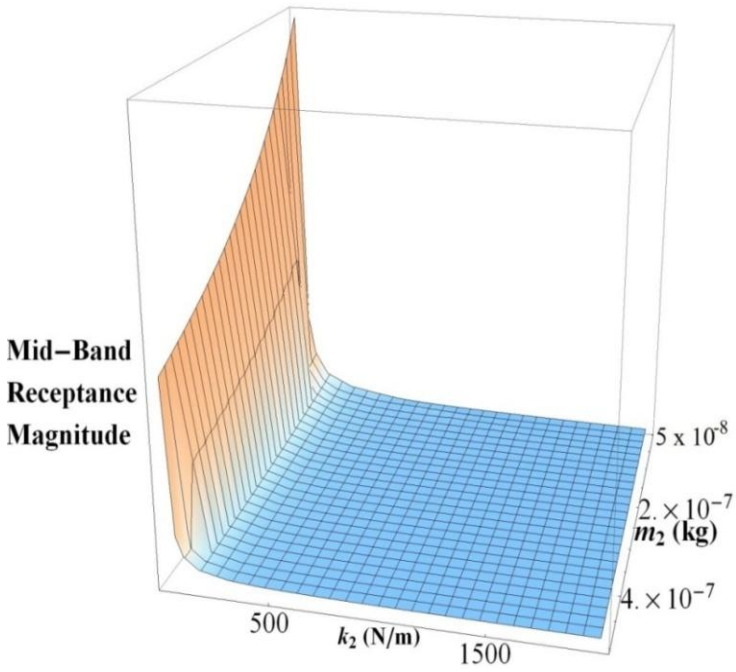

Figure 2.25: Variation of mid-band receptance magnitude due to varying m_2 and k_2.

It can be concluded from the aforementioned arguments that, although the trade-off between bandwidth and sensitivity remains, the proposed design allows the implementation of low k_2 structures with high mechanical sensitivity without sacrificing from m_2. Here k_3 aids in designing m_2 high enough while keeping k_2 minimum.

Table 2.3: Mechanical design parameters of the gyroscopes with previous 2 DoF sense mode and proposed 2 DoF sense mode.

Previous Design	**Proposed Design**
$m_1 = m_2 = 100\ \mu g$	$m_1 = m_2 = 100\ \mu g$
$k_1 = k_2 = 1000\ N/m$	$k_1 = 1000\ N/m$
	$k_2 = 100\ N/m$
	$k_3 = 900\ N/m$
$\varpi_{m1} = \varpi_{m2} = 100000\ rad/s$	$\varpi_{m1} = \varpi_{m2} = 100000\ rad/s$
$c_1 = c_2 = c_3 = 2.5 * 10^{-7}\ Ns/m$	$c_1 = c_2 = c_3 = 2.5 * 10^{-7}\ Ns/m$

Figure 2.26 through Figure 2.29 demonstrate the FRF's of two sense mode oscillators with mechanical design parameters given in Table 2.3, in order to compare the performance of previous design and the proposed design

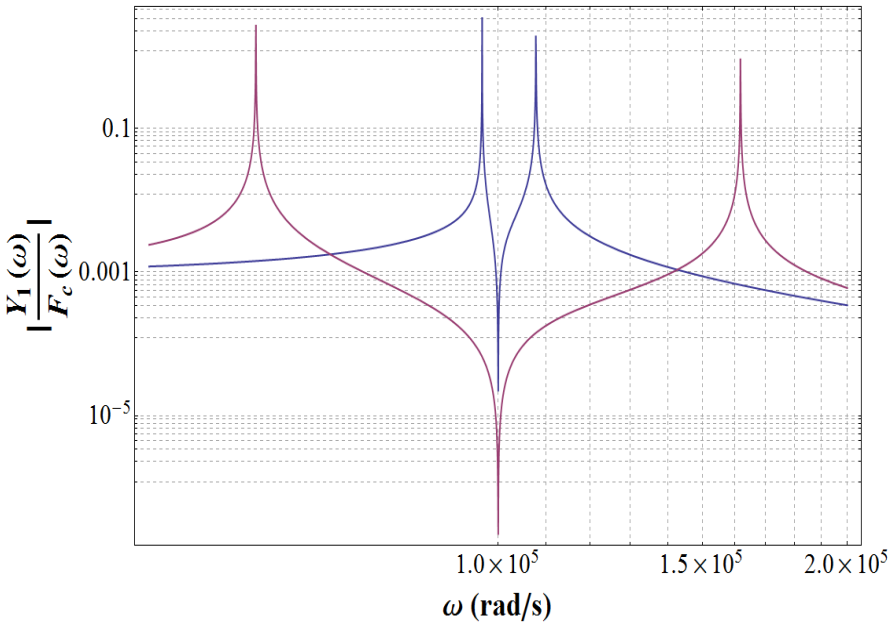

Figure 2.26: Magnitude Receptance FRF for m_1.

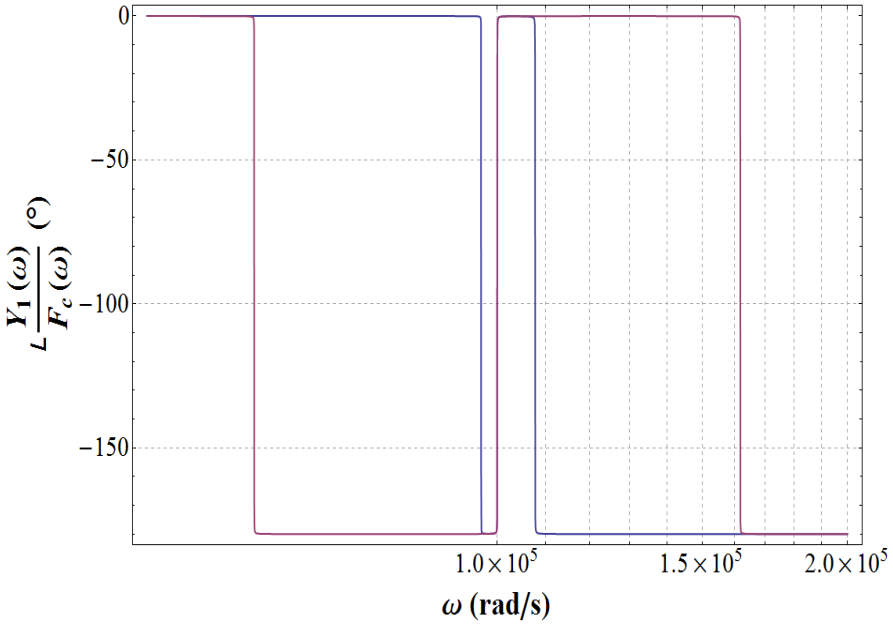

Figure 2.27: Phase Receptance FRF for m_1.

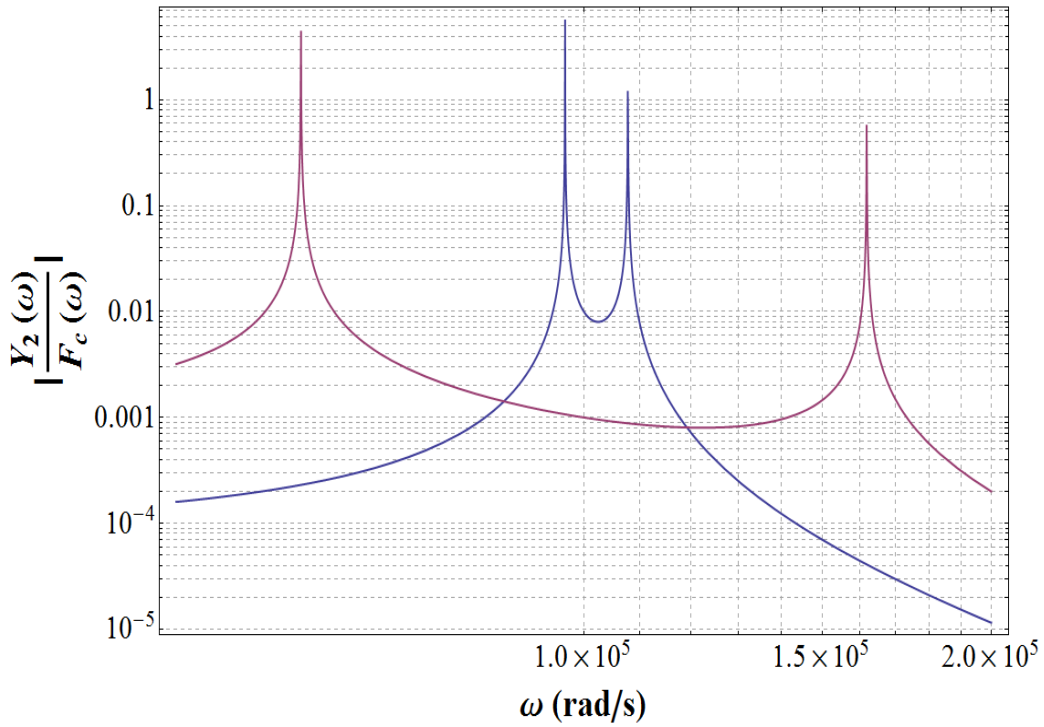

Figure 2.28: Magnitude Receptance FRF for m_2.

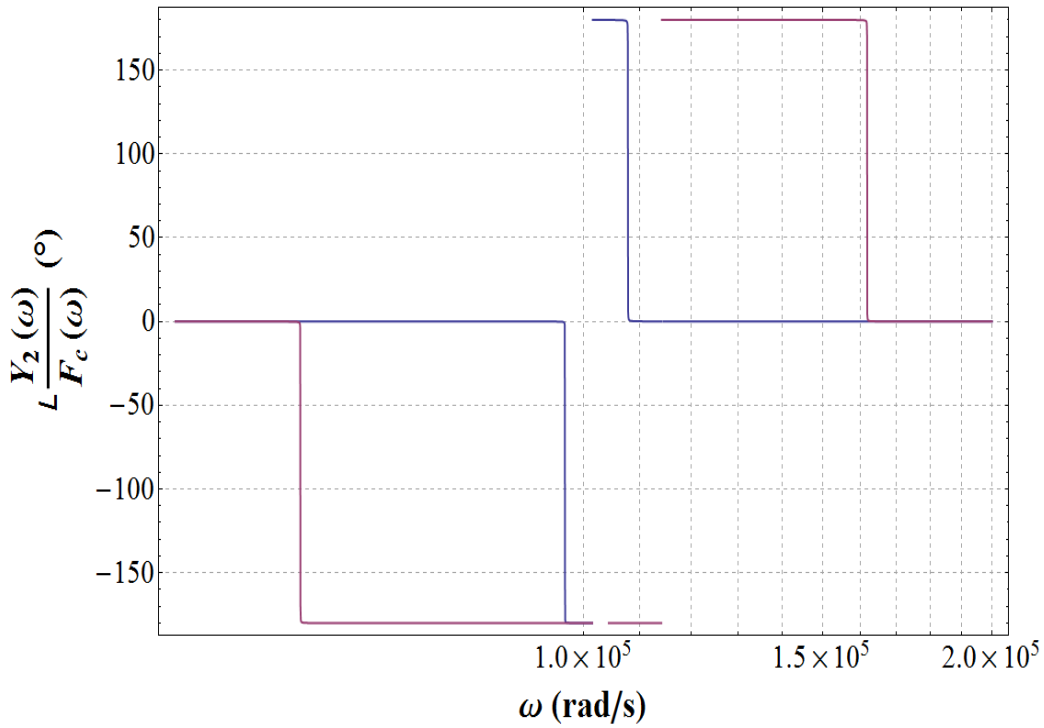

Figure 2.29: Phase Receptance FRF for m_2.

Figure 2.28 clearly demonstrates a ~ 10 times increase in the mid-band receptance magnitude, or the mechanical sensitivity, of the gyroscope when the proposed 2 DoF sense mode oscillator is utilized. It is clear for the proposed design that, bandwidth significantly decreased to around ~ 1.6 kHz with the design parameters given in Table 2.3. On the other hand, there is a flat-band region of ~ 200 Hz around 16313 Hz, which is sufficient for inertial-grade performance. It is not possible to achieve such a high gain with the old design without making m_2 smaller, which is not desirable in terms of electrical sensitivity. Hence the superiority of the proposed design over the previous design is verified.

Next it is necessary to compare the sense mode response of a matched-mode gyroscope with the proposed 2 DoF sense mode design. Figure 2.30 demonstrates the magnitude receptance FRF plots for the gyroscopes with mechanical design parameters given in Table 2.4. The operating frequencies of both gyroscopes are taken as ~ 16313 Hz, which is the mid-band frequency of the 2 DoF design.

Table 2.4: Mechanical design parameters of the 1 DoF matched-mode gyroscope and proposed 2 DoF sense mode gyroscope.

1 DoF Matched-Mode Design	**Proposed 2 DoF Design**
$m = 100\ \mu g$	$m_1 = m_2 = 100\ \mu g$
$k_d = k_s = 1050\ N/m$	$k_1 = 1000\ N/m$
	$k_2 = 100\ N/m$
	$k_3 = 900\ N/m$
$\varpi_n = 102470\ rad/s$	$\varpi_{m1} = \varpi_{m2} = 100000\ rad/s$
$c_s = c_d = 2.5 * 10^{-7}\ Ns/m$	$c_1 = c_2 = c_3 = 2.5 * 10^{-7}\ Ns/m$

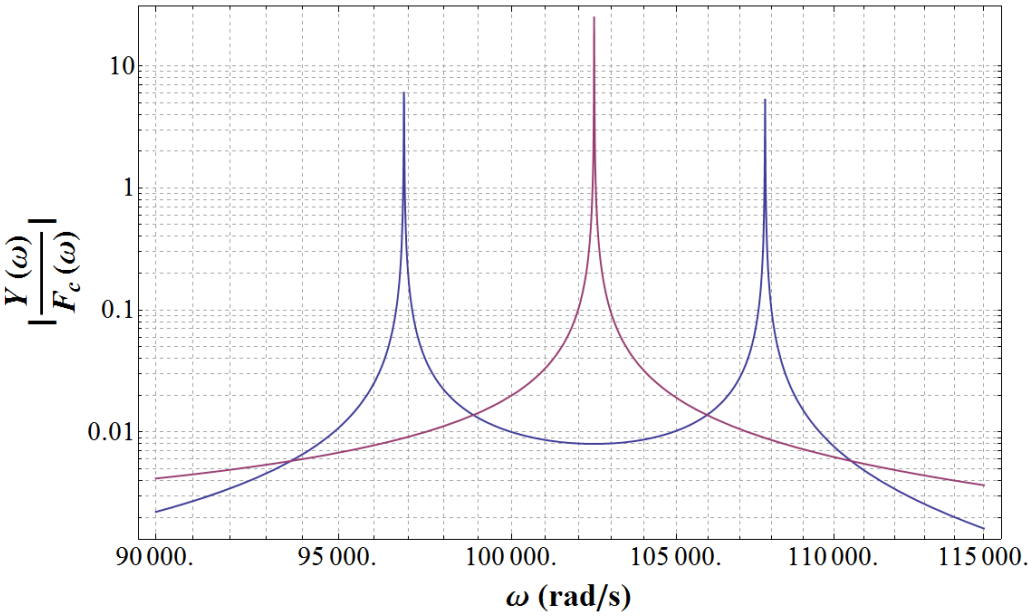

Figure 2.30: Magnitude receptance FRF plots of the sense mode of 1 DoF matched-mode gyroscope and proposed 2 DoF sense mode gyroscope.

It is observed from Figure 2.30 that, the mechanical sensitivity of the matched-mode design is much better than the proposed design due to the resonance effect at the operating frequency. On the other hand, it is clear that as a mode-mismatch is introduced to improve the bandwidth of the 1 DoF gyroscope, the mechanical sensitivity of 1 DoF design degrades very rapidly and gets close to the proposed 2 DoF design. Therefore, the proposed 2 DoF design has the capacity to compete with its 1 DoF counterparts with the use of high performance readout electronics and optimized mechanical structure.

2.4 Sense Mode Dynamics of Gyroscopes with 1 DoF Drive and 2 DoF Sense Modes

Equation 2.77 demonstrates the forcing due to Coriolis coupling, f_c, for a 2 DoF sense mode gyroscope, assuming drive mode forcing is $F_d = F_0 cos(\Omega t)$.

$$f_c = \frac{-2\, m_1\, \omega\, F_0\, \Omega_d}{c_d} \sqrt{\frac{m_d}{k_d}}\, cos(\Omega_d t) \tag{2.77}$$

It is observed from Figure 2.29 that, the phase difference with f_c and sense mode response at the mid-band frequency, which is also the drive frequency, is π rad. Then, Equation 2.77 presents the sense mode response to applied angular rate input.

$$y_2(t) = \left|\frac{Y_2(\Omega_d)}{F_c(\Omega_d)}\right| \frac{2\, m_1\, \omega\, F_0\, \Omega_d}{c_d} \sqrt{\frac{m_d}{k_d}}\, cos(\Omega_d t) \tag{2.78}$$

The result obtained for time-varying angular rate inputs is also applicable to 2 DoF oscillator design. Equation 2.79 demonstrates the sense mode response to the time varying angular rate input of $\varpi(t) = \varpi cos(\Omega_{in} t)$ for a 2 DoF sense mode oscillator gyroscope.

$$y_2(t) = \frac{2\, m_1\, \omega\, F_0\, \Omega_d}{c_d} \sqrt{\frac{m_d}{k_d}} \left(\left|\frac{Y_2(\Omega_d + \Omega_{in})}{F_c(\Omega_d + \Omega_{in})}\right| cos\big((\Omega_d + \Omega_{in})t\big) + \left|\frac{Y_2(\Omega_d - \Omega_{in})}{F_c(\Omega_d - \Omega_{in})}\right| cos\big((\Omega_d - \Omega_{in})t\big) \right) \tag{2.79}$$

Figure 2.31 demonstrates the superiority of 2 DoF sense mode gyroscopes in terms of operation bandwidth. It is clear that for a wide band the sense mode response will be same to time-varying angular rate inputs with same amplitude but different frequencies.

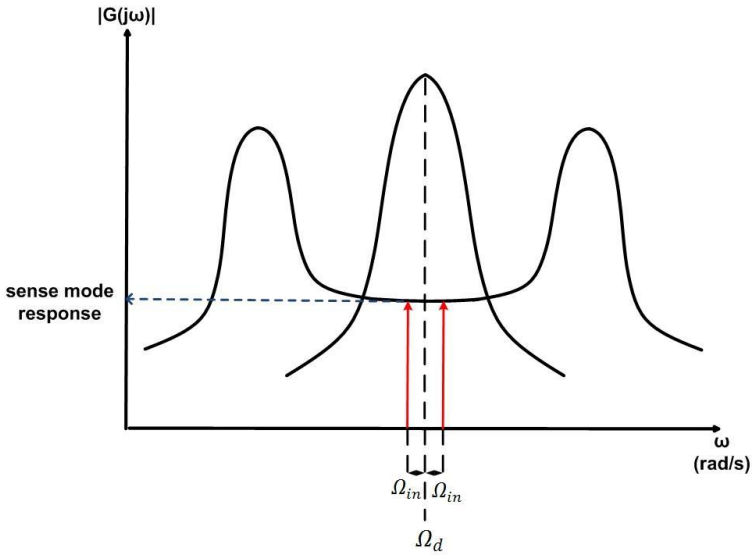

Figure 2.31: Sense mode response to time varying angular rate input of a 1DoF drive and 2 DoF sense mode gyroscope.

2.5 Implementation of a Vibratory Gyroscope using MEMS Technology

Previous sections demonstrate the theoretical background to be utilized in the conceptual design of a vibratory gyroscope. After the completion of the conceptual design, the 3D physical structure of the gyroscope needs to be designed and implemented. This section demonstrates the electromechanical structures utilized in the physical design phase of a micromachined vibratory gyroscope.

2.5.1 Electrostatic Actuation

Figure 2.32 shows the parallel plate capacitor structure, which is the primary building block for electrostatic transduction method of MEMS technology. In this figure *g* denotes the gap distance between the electrode plates, *h* denotes the height of the electrode plates, *l* denotes the length of the electrode plates and l_o denotes the length of the overlapping area of electrode plates.

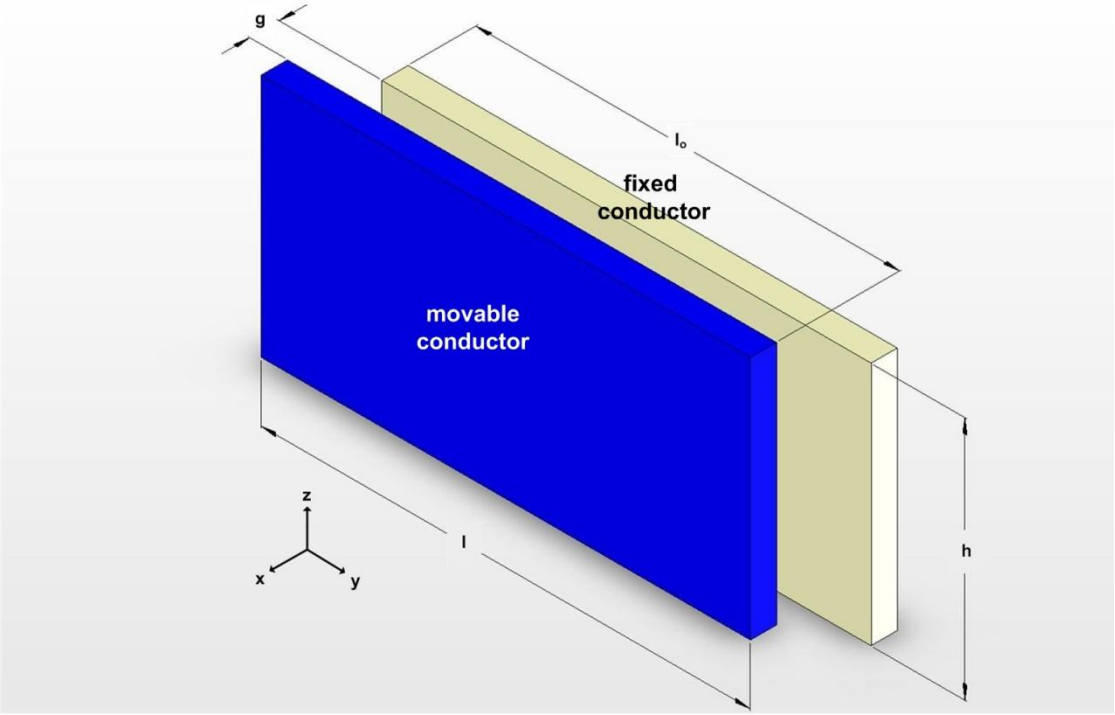

Figure 2.32: Parallel plate capacitor structure.

Equation 2.80 expresses the capacitance value for the parallel plate capacitor structure of Figure 2.32, where ε is the permittivity of the medium between the electrodes.

$$C = \varepsilon \frac{A_{overlap}}{distance\ between\ electrodes} = \varepsilon \frac{h\,(l_o + y)}{g + x} \tag{2.80}$$

Fabrication is performed planar wise, such that the plate heights are the same and the plates are fully overlapping in the z direction in typical micromachining technologies. On the other hand, electrodes are drawn with some non-overlapping area on purpose in y direction. One of the most famous laws of thermodynamics is the tendency of any matter or process in nature to reduce its potential energy. This law can be expressed mathematically as the negative gradient of potential energy (U) of a system being applied on the system as a force to minimize its potential energy. Equation 2.81 demonstrates that expression.

$$\vec{F} = -\nabla U \tag{2.81}$$

This law holds true but with a positive sign before the gradient operator for a parallel plate capacitor with a fixed potential difference of V applied between electrodes [37]. Equation 2.82 presents the potential energy stored at the parallel plate capacitor system, while Equations 2.83 and 2.84 demonstrate the net forces on electrode plates in x and y directions, respectively, where α is a correction factor used to account for fringing electric fields.

$$U = \frac{1}{2} CV^2 = \frac{1}{2} \varepsilon \frac{h\,(l_o + y)}{g + x} V^2 \tag{2.82}$$

$$F_x = +\frac{\partial U}{\partial x} = -\frac{1}{2} \alpha\, \varepsilon \frac{h\,(l_o + y)}{(g + x)^2} V^2 \tag{2.83}$$

$$F_y = +\frac{\partial U}{\partial y} = \frac{1}{2} \alpha\, \varepsilon \frac{h}{g + x} V^2 \tag{2.84}$$

The minus sign in Equation 2.83 means that the electrostatic force is in –x direction, so as to attract the movable conductor to the fixed one. The force equation in y

direction tells that, the movable conductor is forced to make the two electrode areas to be perfectly overlapping by aligning itself with the fixed conductor. If there were any non-overlapping portion in z direction there would be a force so as to align the electrodes in z direction too.

The parallel plate capacitors are formed into groups called *comb drive actuators* by using a number of parallel plate capacitor structures in *varying-overlap-area* and *varying-gap* configurations in micromachined electrostatic actuators. The 3D views of those structures are shown in Figure 2.33. For the varying-gap configuration the smaller gap, or g_1 is called the gap, while the larger one is called the anti-gap in literature.

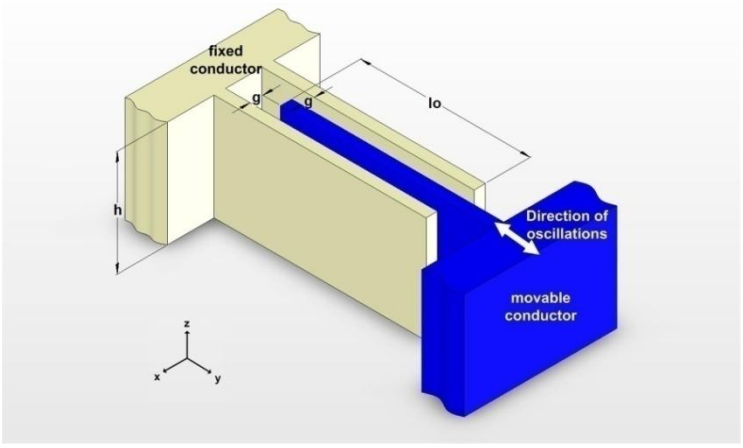

(a)

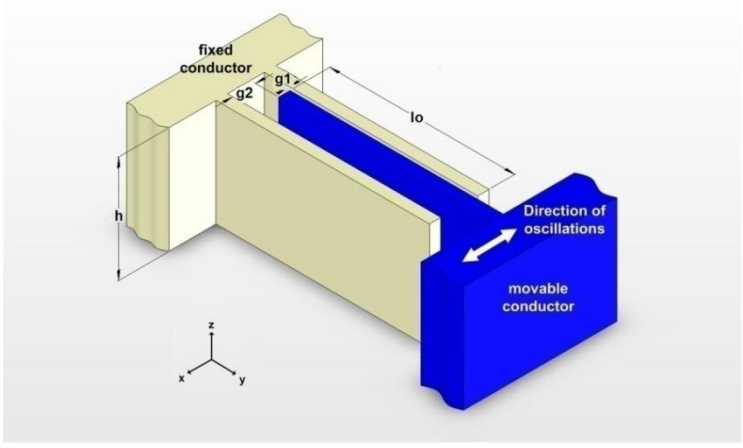

(b)

Figure 2.33: 3D views of comb drives with (a) the varying-overlap-area and (b) the varying-gap configurations

Equations 2.85 and 2.86 represent the drive force for a comb actuator with *N* number of varying-overlap-area type capacitive parallel plates and *N* number of varying-gap type capacitive parallel plates, respectively. Usually anti-gap distance is designed to be much higher than the gap distance; therefore, the force component associated with anti-gap is neglected in Equation 2.86.

$$F_d = 2\,\frac{1}{2}\,N\,\alpha\,\varepsilon\,\frac{h}{g}\,V^2 = N\,\alpha\,\varepsilon\,\frac{h}{g}\,V^2 \tag{2.85}$$

$$F_d = -\frac{1}{2}N\,\alpha\,\varepsilon\,\frac{h\,l_o}{{g_1}^2}\,V^2 + \frac{1}{2}N\,\alpha\,\varepsilon\,\frac{h\,l_o}{{g_2}^2}\,V^2 = -\frac{1}{2}N\,\alpha\,\varepsilon\,\frac{h\,l_o}{{g_1}^2}\,V^2 \tag{2.86}$$

When Equations 2.85 and 2.86 are inspected, it is observed that a varying-overlap-area type of comb actuator generates a constant force in the direction of actuation, while the force generated by a varying-gap type of comb actuator depends on the displacement of the movable capacitor plate in the direction of actuation, with an inverse square relationship. The inverse square relationship makes the varying-gap type of comb actuators ideal for applications requiring large forces applied on very small stroke amplitudes, such that force-deflection characteristics is linearized. On the other hand, the smaller but constant force generated by the varying-overlap-area type of comb actuators makes them ideal for oscillating the movable conductor linearly with high stroke amplitudes. Varying-overlap-area type of comb actuators are to be used for the drive mode oscillator in this research as the drive mode of a micromachined vibratory gyroscope requires high oscillation amplitudes for maximum mechanical sensitivity.

The force equations reveal one more fact that, the mechanical force generated by the comb actuators are a function of the square of the voltage applied between the fixed and movable conductors. A time varying voltage with a frequency equal to resonance frequency of the drive mode oscillator (ϖ_{rd}), on top of a DC voltage is applied to the comb actuator in practice, in order to obtain maximum oscillation amplitude. Equation 2.87 gives the general form of the voltage applied to a comb actuator, while Equation 2.88 shows the force generated by the applied voltage for the varying-overlap-area type comb actuator.

$$v_{DRIVE} = V_{DRIVE} + v_{drive} = V_D + v_d \sin(\varpi_{rd} t) \tag{2.87}$$

$$F_d = N \alpha \varepsilon \frac{h}{g} (V_D + v_d \sin(\varpi_{rd} t))^2$$

$$= N \alpha \varepsilon \frac{h}{g} \left(\underbrace{\left(V_D{}^2 + \frac{v_d{}^2}{2} \right)}_{\text{DC forcing term}} + \underbrace{V_D \, v_d \sin(\varpi_{rd} t)}_{\text{AC forcing term at } \varpi_{rd}} - \underbrace{\frac{v_d{}^2}{2} \cos(2\varpi_{rd} t)}_{\text{AC forcing term at } 2\varpi_{rd}} \right) \tag{2.88}$$

Examining Equation 2.88 it is observed that a complicated forcing situation is applied to the comb drive structure. As the forces on the fixed conductor are supported at the anchor points, it is necessary to talk about the motion of the movable conductor which is connected to the anchor point through flexible linkages. As the drive mode oscillators are designed to have high resonance peaks only at ϖ_{rd}, second harmonic AC forcing term will generate negligible oscillations. DC forcing term will also be eliminated by placing a second fixed conductor in symmetry condition to the first one, and applying it a voltage of $v_{DRIVE} = V_{DRIVE} - v_{drive}$. Then, only the effect of AC forcing with frequency equal to drive mode resonance frequency will be observed. This kind of drive mode actuation is called *differential drive actuation* and it will be utilized in the design study of this research.

2.5.2 Capacitive Sensing

Electrostatic transduction is one of the most commonly used transduction techniques in MEMS applications because the transduction elements, varying-overlap-area and varying-gap type capacitive structures, do not need extra processing steps during fabrication. Primary reason for electrostatic transduction to be preferred for micromachined gyroscopes is another important property of the electrostatic transduction structures that, same structures can be utilized both for the sense and drive mode mechanisms. A DC voltage is applied between the fixed and movable conductors in order to use the electrostatic transduction elements for sensing the magnitude of oscillations generated by Coriolis coupling. When the movable capacitor plates oscillate, the capacitance of the structure changes, resulting in a flow of current through sense mode readout electronics. Equation 2.89 demonstrates

generated sense mode current, i_s, where C_s is the sense capacitance and V_s is the voltage applied between the fixed and movable plates of sense mode comb structure.

$$i_s = \frac{\partial C_s V_s}{\partial t} = V_s \frac{\partial C_s}{\partial t} + C_s \frac{\partial V_s}{\partial t} = V_s \frac{\partial C_s}{\partial t} \tag{2.89}$$

Equations 2.90 and 2.91 demonstrate the sense mode current equations for varying-overlap-area and varying-gap type structures, respectively.

$$i_s = V_s \frac{\partial C_s}{\partial t} = V_s \frac{\partial C_s}{\partial y} \frac{\partial y}{\partial t} = V_s N \alpha \varepsilon \frac{h}{g} \frac{\partial y}{\partial t} \tag{2.90}$$

$$i_s = V_s \frac{\partial C_s}{\partial t} = V_s \frac{\partial C_s}{\partial x} \frac{\partial x}{\partial t} = \frac{1}{2} V_s N \alpha \varepsilon \frac{h\, l_o}{g^2} \frac{\partial x}{\partial t} \tag{2.91}$$

When the sense mode current expressions for varying-overlap-area and varying-gap type capacitive structures are compared, it is observed that varying-gap comb structure has an inverse square relation in the direction of oscillations. As sense mode oscillation amplitudes are on the order of nanometers, this square relationship does introduce a negligible non-linearity while offering a great sensitivity to sense mode oscillations. Therefore, varying-gap type capacitive plates are to be used in the design study of this research.

2.5.3 Flexible Linkages

Movable conductors are connected to the anchor points via flexible linkages in micromachined vibratory gyroscopes. Flexible linkages are designed so as to show a required amount of flexibility in determined directions, while restricting motion in all other directions. The simplest of flexible linkages is the cantilever beam structure shown in Figure 2.34.

Equation 2.92 represents the deflection of the tip point when a force is applied at the tip of the cantilever beam, where E is the Young's Modulus of the material [38]. Equation 2.93 presents the spring constant of the cantilever beam obtained by manipulating Equation 2.92.

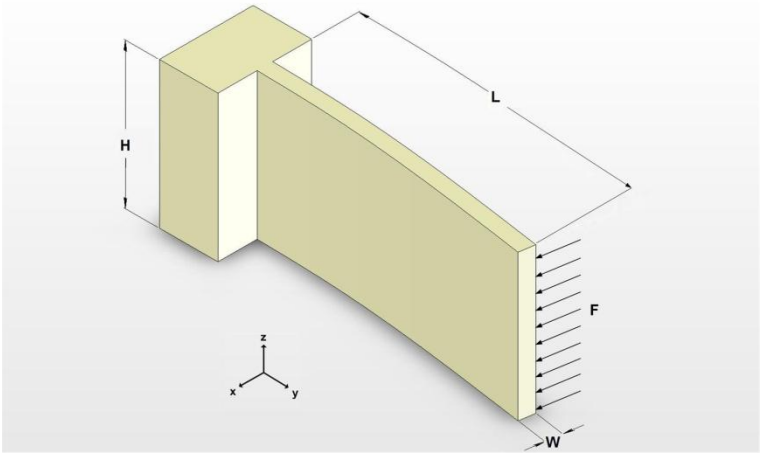

Figure 2.34: Cantilever beam structure.

$$x_{tip} = F_x \frac{4\,l^3}{E\;h\,w^3} \tag{2.92}$$

$$k_x = \frac{1}{4} E\,h \left(\frac{w}{l}\right)^3 \tag{2.93}$$

Figure 2.35 illustrates a clamped-guided beam configuration, where one end of the beam is fixed while the other end is guided to move only in the x direction (no rotation allowed). Equation 2.94 expresses the spring constant of a clamped-guided beam structure obtained from the deflection expression of the guided end.

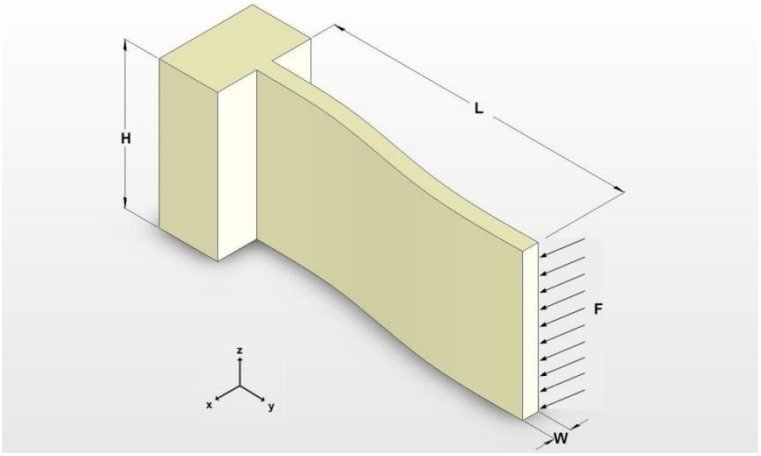

Figure 2.35: Clamped-guided beam structure.

$$k_x = E\, w \left(\frac{h}{l}\right)^3 \tag{2.94}$$

Cantilever and clamped-guided beams are flexible linkage elements that are simple to fabricate and design. On the other hand, as the end deflections increase, they show considerable nonlinearity in their force-deflection characteristics. Clamped-guided beams are usually formed into double folded linkage configuration in order to increase the linear displacement range, as shown in Figure 2.36. For this structure, it is observed that beam 1 and beam 4 are serially connected, just like the connection of beam 2 and beam 3. Then, beam 1-4 combination is parallel connected to beam 2-3 combination through the rigid link. For this structure the stiffness of the rigid link should be much stiffer than the beams in x direction so as to assume it as rigid. Equation 2.95 presents the spring constant of the overall folded-beam structure, which is equal to one of the clamped-guided beams if all the beams show the same spring constant in x direction.

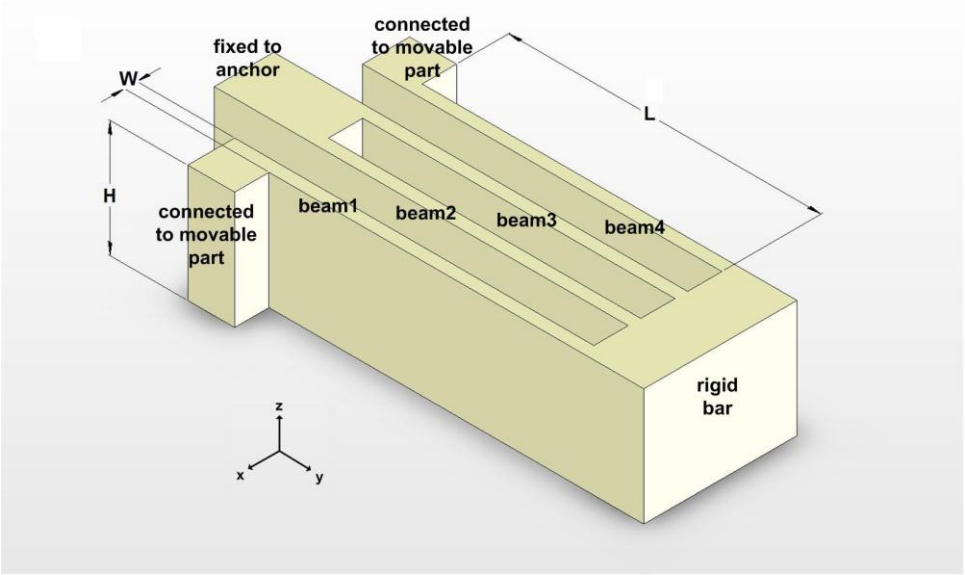

Figure 2.36: Double folded linkage configuration.

$$K_x = \left(\left(\frac{1}{k_{x1} + k_{x4}}\right) + \left(\frac{1}{k_{x2} + k_{x3}}\right)\right)^{-1} = k_x \tag{2.95}$$

2.6 Secondary Effects

2.6.1 Inherent Nonlinearities of Vibratory Gyroscopes

The use of simplified dynamics equations demonstrated in Section 2.2 is questioned in this section. The mechanical components are represented with Simulink blocks to obtain numerical solution of the nonlinear coupled differential equation system, as the modeling of the full dynamics requires dealing with the nonlinear coupled differential equation system given in Equations 2.44 and 2.45. Figure 2.37 and Figure 2.38 illustrate the Simulink block diagrams for the simplified and the full gyroscope dynamics, respectively.

The simulations are performed for a vibratory gyroscope with the mechanical parameters given in Table 2.5. The quality factor Q of the drive and sense modes is 40000, while the drive mode oscillation amplitude is calculated to be 10μm using Equation 2.41 for this parameter set. Hence, the parameters satisfy the requirements stated in [9] for inertial-grade operation.

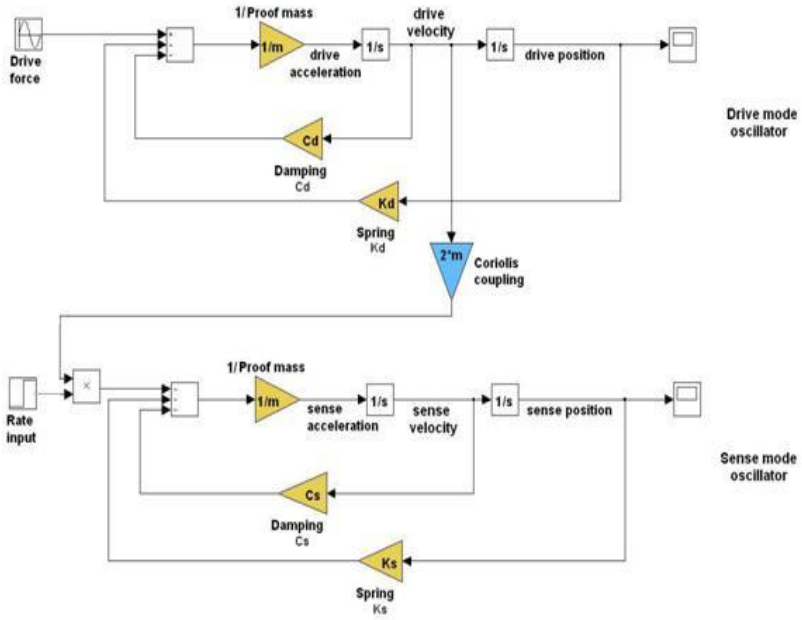

Figure 2.37: Simulink block diagram for simplified gyroscope dynamics model

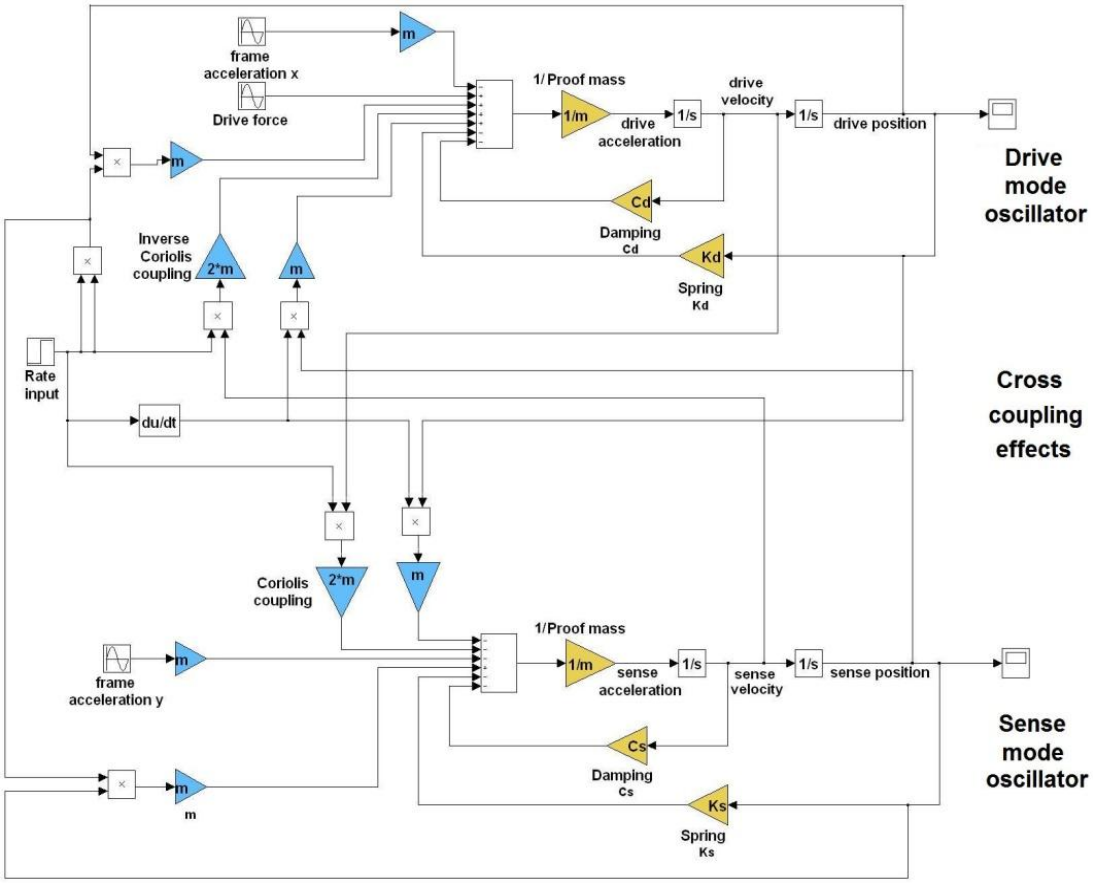

Figure 2.38: Simulink block diagram for the full gyroscope dynamics model

Table 2.5: Mechanical parameter values for the vibratory gyroscope analyzed in Simulink.

$m = 100\ \mu g$
$k_d = k_s = 1000\ N/m$
$\varpi_n = 100000\ rad/s$
$c_s = c_d = 2.5 * 10^{-7}\ Ns/m$
$F_d(t) = 0.25 \cos(\varpi_n t)\ \mu N$

No linear acceleration inputs are given to the system during simulations as the sensitivity of a gyroscope to external accelerations can be eliminated by using a tuning fork structure. Firstly, no rate input is applied to the system and a convergence study is performed on the drive mode response to determine the numerical solution parameters that will give accurate results. Figure 2.39 shows the

simulated drive mode response verifying the accuracy of simulation results obtained after the convergence study.

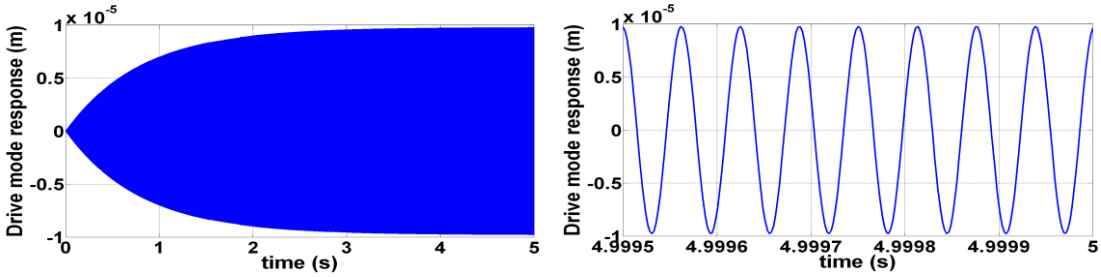

(a) **(b)**

Figure 2.39: Drive mode response verifying the accuracy of simulation results (a) overall response (b) close up view.

After the accuracy of simulation results is verified, angular rate input of 1 °/s, 50 °/s and 100 °/s at t=0.5s are applied to the system and the plots of drive and sense mode responses for 5 s are shown through Figure 2.40 to Figure 2.45.

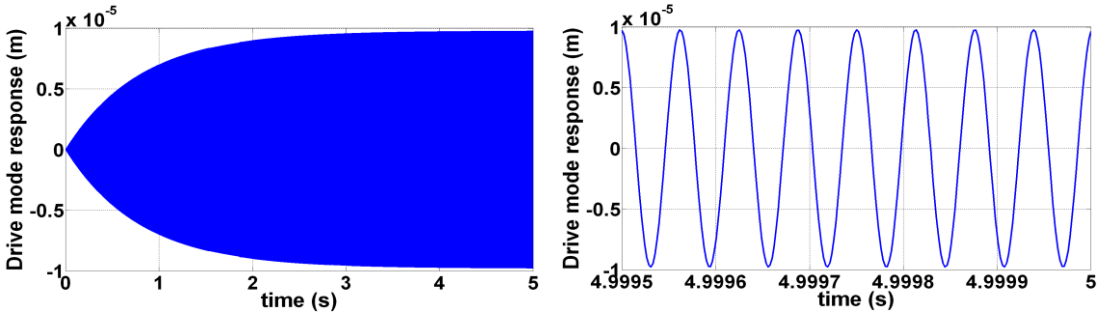

(a) **(b)**

Figure 2.40: Drive mode response to an angular rate input of 1 °/s (a) overall response (b) close up view.

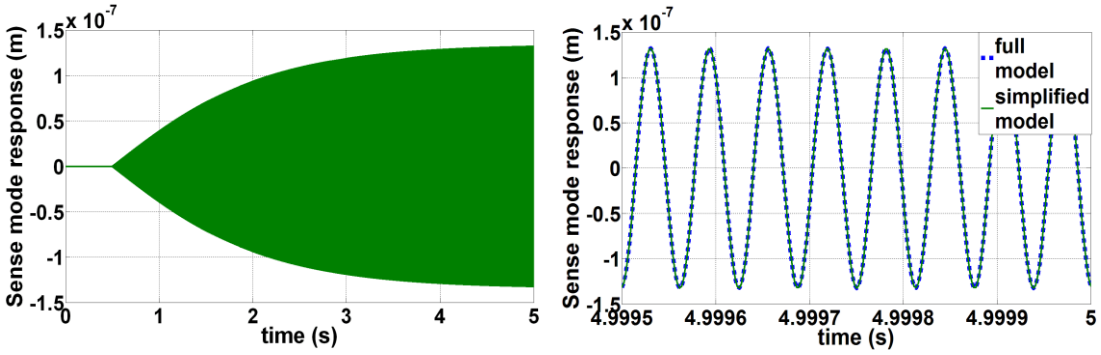

(a) **(b)**

Figure 2.41: Sense mode response to an angular rate input of 1 °/s (a) overall response (b) close up view.

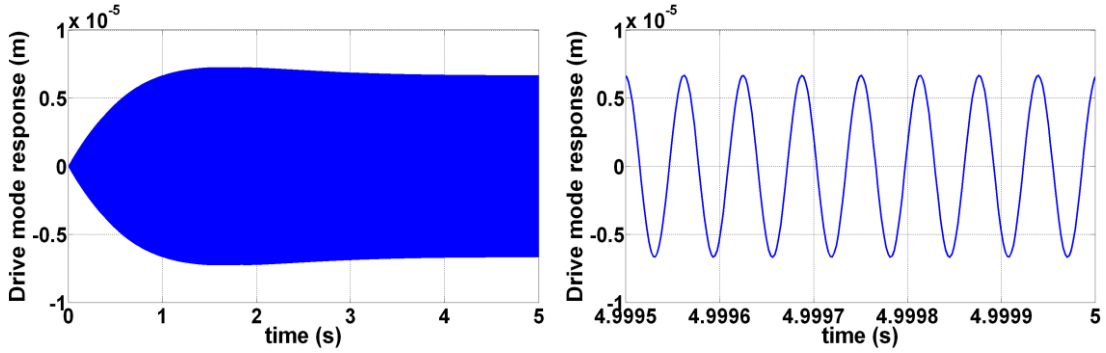

(a) **(b)**

Figure 2.42: Drive mode response to an angular rate input of 50 º/s (a) overall response (b) close up view.

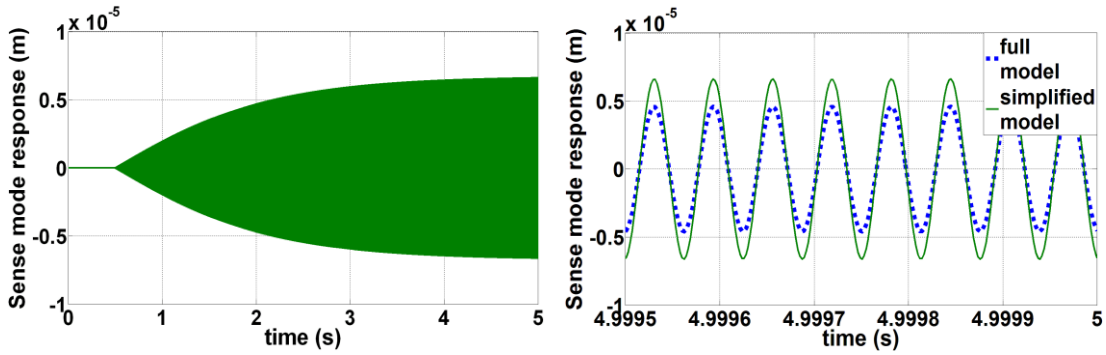

(a) **(b)**

Figure 2.43: Sense mode response to an angular rate input of 50 º/s (a) overall response (b) close up view.

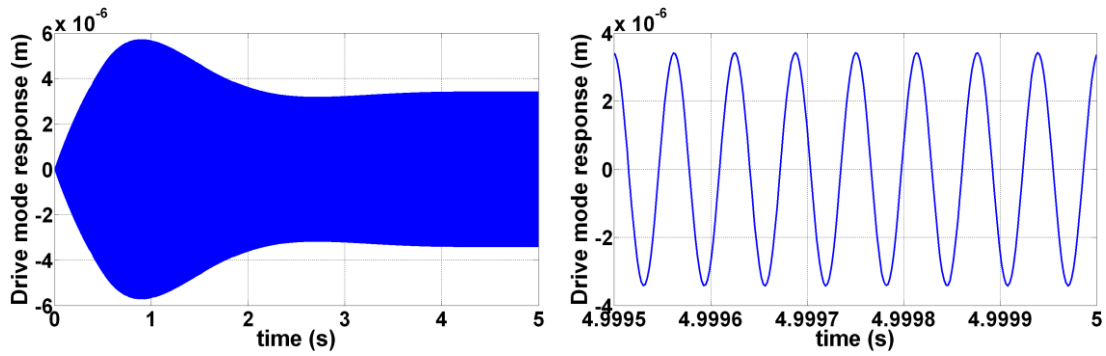

(a) **(b)**

Figure 2.44: Drive mode response to an angular rate input of 100 º/s (a) overall response (b) close up view.

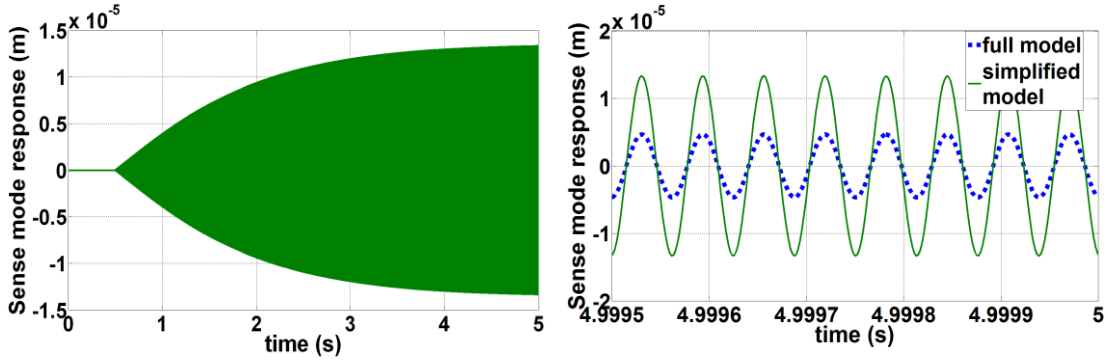

(a) **(b)**

Figure 2.45: Sense mode response to an angular rate input of 100 °/s (a) overall response (b) close up view.

Table 2.6 summarizes the response amplitudes for the simplified dynamics and full dynamics models of the gyroscope calculated using Simulink, for angular rate inputs of of 1 °/s, 50 °/s and 100 °/s, in addition to the error introduced by using the simplified model for matched-mode conditions.

Table 2.6: The response amplitudes for the simplified dynamics and full dynamics models of the gyroscope calculated using Simulink, for angular rate inputs of 1 °/s, 50 °/s and 100 °/s, in addition to the error introduced by using the simplified model for matched-mode conditions.

Angular rate input (°/s)	**Drive mode response**			**Sense mode response**		
	Simplified Model (µm)	**Full Model (µm)**	**Error (%)**	**Simplified Model (µm)**	**Full Model (µm)**	**Error (%)**
1	9.95	9.95	0	0.13	0.13	0
50	9.95	6.7	48.5	6.5	4.5	44.4
100	9.95	3.4	192.6	13.2	4.65	183.8

Examining Table 2.6 it is clear that the sense mode oscillator displays a highly nonlinear response to applied angular rate inputs, as expected from the existence of nonlinear cross-coupling terms in Equations 2.44 and 2.45. The discrepancy between the full model and simplified model can be decreased if the drive mode

oscillations in the full model are kept at 10μm by increasing the drive force. Keeping the drive mode oscillation amplitude constant by adjusting drive force via closed-loop drive mode amplitude control electronics are suggested in literature [16, 28, 39]. On the other hand, the aim for the utilization of those closed-loop circuits are reported to be keeping the drive mode oscillation constant in spite of Q factor changes, that are originating from variations in ambient pressure conditions. Simulink simulations on sense mode response while keeping the drive mode oscillation amplitude at 10μm are performed. Figure 2.46 to Figure 2.49 show the plots of drive and sense mode responses to angular rate inputs of 50 °/s and 100 °/s.

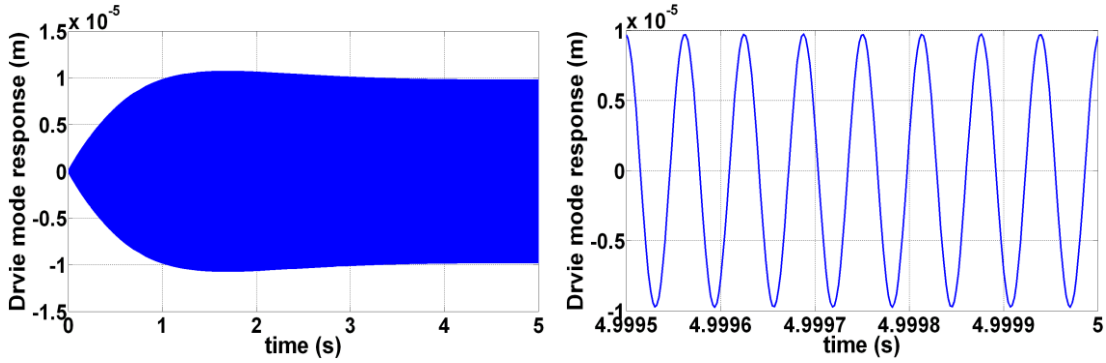

(a) **(b)**

Figure 2.46: Drive mode response being kept constant at 10μm while an angular rate input of 50 °/s is applied to the gyroscope (a) overall response (b) close up view.

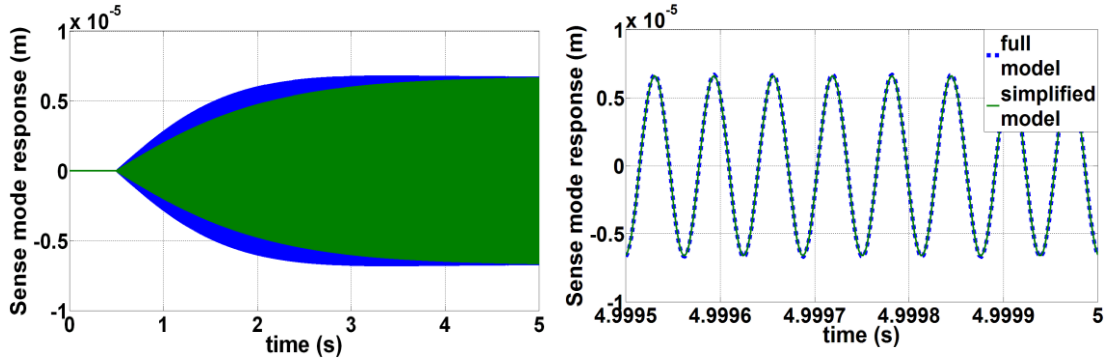

(a) **(b)**

Figure 2.47: Sense mode response to an angular rate input of 50 °/s (a) overall response (b) close up view.

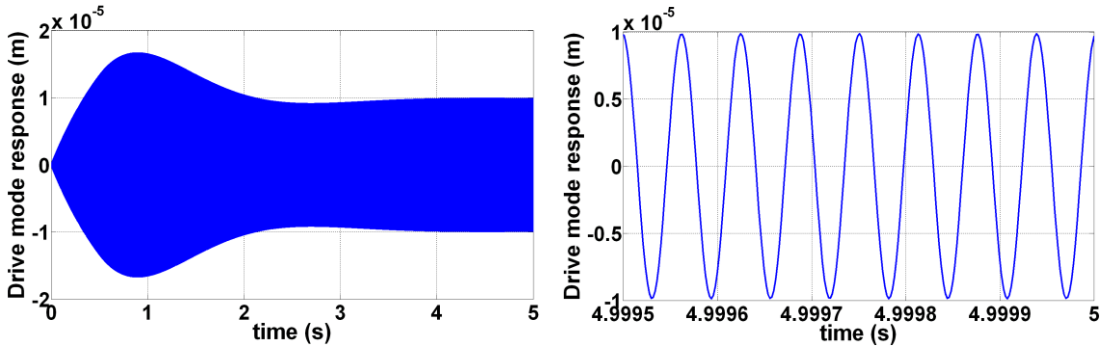

(a) **(b)**

Figure 2.48: Drive mode response being kept constant at 10μm while an angular rate input of 100 °/s is applied to the gyroscope (a) overall response (b) close up view.

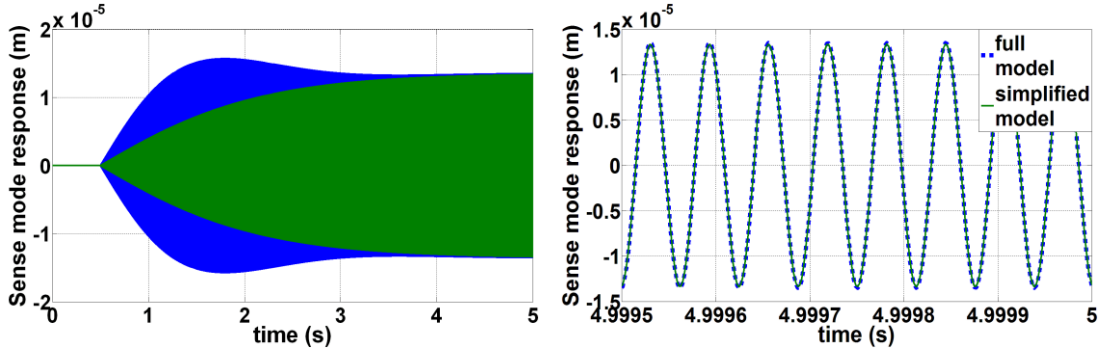

(a) **(b)**

Figure 2.49: Sense mode response to an angular rate input of 100 °/s (a) overall response (b) close up view.

Table 2.7 summarizes the sense mode response amplitudes for the simplified dynamics and full dynamics models of the gyroscope calculated using Simulink, for angular rate inputs of 50 °/s and 100 °/s, in addition to the error introduced by using the simplified model for matched-mode conditions while drive mode response amplitude is kept constant at 10 μm.

It is clear from Table 2.7 that, the discrepancy between the results obtained from the simplified and full models significantly reduce if drive mode oscillation amplitude is kept constant. Moreover, the sense mode response becomes more linear although a small nonlinearity remains with drive mode amplitude control. Therefore, drive amplitude control circuits seem very useful considering both inherent nonlinearities of vibratory gyroscopes and Q factor changes originating from variations in ambient pressure conditions.

Table 2.7: The sense mode response amplitudes for the simplified dynamics and full dynamics models of the gyroscope calculated using Simulink, for angular rate inputs of 50 °/s and 100 °/s, in addition to the error introduced by using the simplified model for matched-mode conditions while drive mode response amplitude is kept constant at 10 μm.

Angular rate input (°/s)	Sense mode response		
	Simplified Model (μm)	Full Model (μm)	Error (%)
50	6.5	6.7	2.9
100	13.2	15.5	14.8

2.6.2 Electrostatic Spring Effect of Varying-Gap Type Capacitive Plates

An important property of varying-gap type capacitive plates is the phenomenon of electrostatic spring. This effect can be observed if the force-deflection characteristics of a varying-gap type capacitive plate structure is drawn. Figure 2.50 demonstrates a typical force–deflection curve for a varying-gap type capacitive plate.

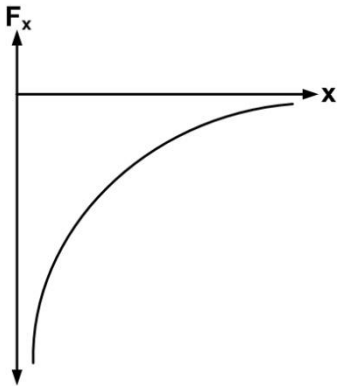

Figure 2.50: Force-deflection characteristics of a varying-gap capacitive plate structure.

It is observed from the force-deflection characteristics that, the attractive force between the fixed and movable plates increases very fast as the gap spacing decreases, but it will diminish as the gap spacing is increased. A force-deflection curve of this type resembles a nonlinear spring connected between the two electrode

plates with a negative spring constant such that, as the spring elongates (gap spacing increases) the force applied by the spring on the electrodes diminishes, but it increases tremendously when the spring elongation is reduced. Equation 2.96 expresses this result mathematically by taking the derivative of the force expression with respect to displacement.

$$\frac{\partial F_d}{\partial x} = \frac{\partial}{\partial x}\left(-\frac{1}{2} N\,\alpha\,\varepsilon\,\frac{h\,l_o}{(g_1+x)^2}\,V^2\right) = N\,\alpha\,\varepsilon\,\frac{h\,l_o\,(g_1+x)}{(g_1+x)^4}\,V^2 = N\,\alpha\,\varepsilon\,\frac{h\,l_o}{(g_1+x)^3}\,V^2 = k_x \qquad (2.96)$$

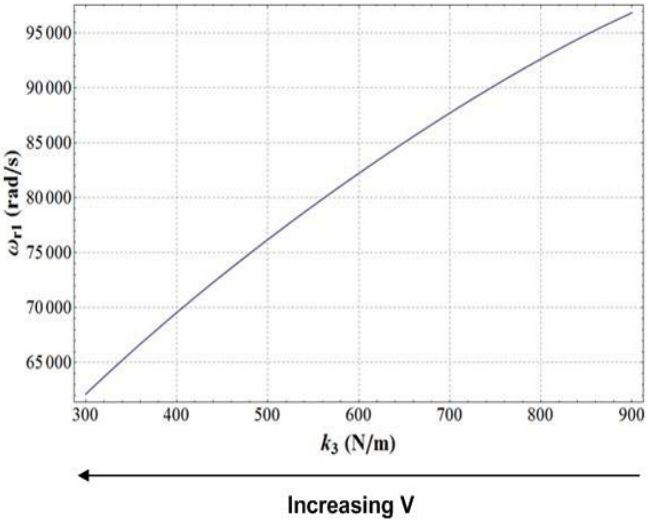

Figure 2.51: Variation of the first resonance frequency of the proposed 2 DoF sense mode oscillator due to negative electrostatic spring effect.

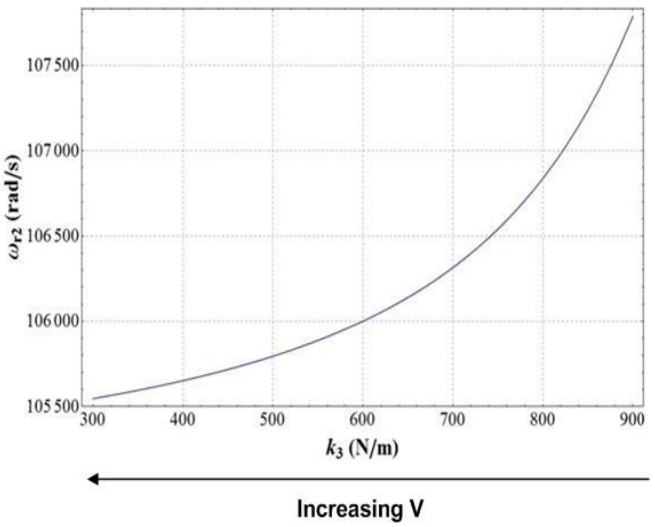

Figure 2.52: Variation of the second resonance frequency of the proposed 2 DoF sense mode oscillator due to negative electrostatic spring effect.

In the design of the proposed 2 DoF sense mode gyroscope, this negative electrostatic spring will decrease the k_3 value shown in Figure 2.17. This results in a significant decrease in the first resonance frequency of the 2-DoF sense mode oscillator, while decreasing the second resonance frequency with a smaller amount. Figure 2.51 and Figure 2.52 demonstrate variation of the resonance frequencies due to negative electrostatic spring, for the 2 DoF sense mode gyroscope with mechanical parameters given in Table 2.4. Poor tolerances in micromachining technologies result in discrepancies between the designed and fabricated mechanical structures, therefore, there is a need to tune the sense mode oscillator resonance frequencies after fabrication, and negative electrostatic spring effect is utilized for this purpose in practice.

2.6.3 Quadrature Coupling

Flexible linkages utilized in a gyroscope show deviations between each other due to poor fabrication tolerances. This results in a misalignment of the drive mode axis with respect to its designed position. Figure 2.53 demonstrates an exaggerated view of drive axis misalignment due to fabrication tolerances, on a decoupled gyroscope. Due to the misalignment of drive axis, orthogonality between the drive and sense mode oscillators is lost and the sustained oscillations show a component in the sense axis. Therefore, the sense mode oscillator shows a small but finite oscillation amplitude in the absence of any angular rate input, resulting in a constant DC offset at the gyroscope output, called ZRO that was defined in Section 1.2. It was shown in Sections 2.2 and 2.4 that, sense mode response to Coriolis coupling shows a phase shift of $\frac{\pi}{2}$ rad from drive mode oscillations, both for 1 DoF and 2 DoF sense mode oscillators. Phase sensitive sense mode readout electronics circuits are utilized in most of the reported gyroscopes. The purpose of these circuits is to differentiate between the electrical signal at the output of the gyroscope originating from quadrature coupling and Coriolis coupling. Perfect cancellation of quadrature coupling is possible through the use of phase sensitive electronics theoretically; on the other hand, there remains a very small signal due to quadrature coupling, resulting in degrading ZRO performance in practice.

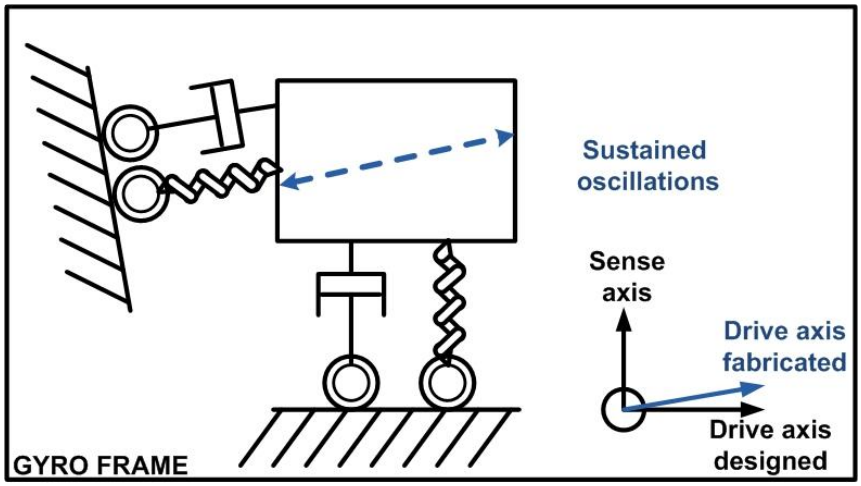

Figure 2.53: An exaggerated view of drive axis misalignment due to fabrication tolerances

2.6.4 Mechanical – Thermal noise in Micromachined Vibratory Gyroscopes

For micromachined vibratory gyroscopes one of the main noise sources is mechanical-thermal noise [40]. Atoms and molecules of any matter in thermal equilibrium with its surroundings are in random motion due to their thermal energy. In solids these motions are observed as phonon waves. For fluids, the molecules are more free to make random motion, as intermolecular forces are less pronounced. The random motion of fluids due to their thermal energy causes collisions and random agitations, known as Brownian motion. Sense mode oscillations on the order of atomic dimensions are required to be detected by sense mode electronics to achieve high angular rate resolution in micromachined vibratory gyroscopes. On the other hand, due to the collisions of gas molecules to the gyroscope structure, sense mode oscillator makes random oscillations on the order of atomic dimensions. Therefore, those random oscillations set a limit on the minimum resolvable angular rate input. Equation 2.97 presents the mean square oscillation amplitude for a spring-mass oscillator, with spring constant k, where k_B is the Boltzmann's constant and T is the absolute temperature [40].

$$\langle x^2 \rangle = \frac{k_B T}{k} \tag{2.97}$$

It has been reported that mechanical-thermal noise for any mechanical system in thermal equilibrium with its surroundings can be analyzed by adding a noise generator alongside of each damper [40]. Equation 2.98 presents the spectral density of added randomly fluctuating force related to any mechanical damper with damping constant *c*.

$$F = \sqrt{4k_B Tc} \tag{2.98}$$

It is concluded from Equation 2.98 that, decreasing the damping introduced to the gyroscope will decrease the mechanical-thermal noise, in addition to increasing the mechanical sensitivity of the gyroscope due to increased Q factors. Therefore, most of the gyroscopes are vacuum packaged to eliminate the damping introduced to the gyroscope, although complete elimination of Brownian noise requires the structures to be cooled to absolute 0 K temperature, which is practically impossible.

2.7 Summary

This chapter presented the theoretical background lying behind the design of micromachined vibratory gyroscopes. It demonstrated the kinematics and dynamics of relative motion, in addition to fundamental mechanical vibrations theory. The theoretical work behind 2 DoF sense mode oscillators is thoroughly investigated and a novel 2 DoF sense mode oscillator is proposed in this chapter. The advantages and disadvantages of the proposed oscillator against previous 2 DoF sense mode oscillator gyroscope designs, and against mode-matched gyroscopes are investigated. Next, inherent nonlinearities of micromachined gyroscopes, effect of negative electrostatic springs to the two vibration modes of the proposed sense mode oscillator, and mechanical-thermal noise are presented thoroughly.

CHAPTER 3

ELECTROMECHANICAL DESIGN AND FABRICATION OF THE PROPOSED GYROSCOPE

This chapter demonstrates electromechanical design and fabrication of a mode-decoupled tuning-fork gyroscope based on the proposed 2 DoF sense mode oscillator. Section 3.1 presents the electromechanical design. This section demonstrates design stages from conceptual design to physical design. Section 3.2 presents results of FEA simulations, performed to verify the design parameters extracted by using analytical background developed in Chapter 2. Finally, Section 3.3 summarizes the steps of in-house SOG micromachining process developed at METU Microelectronics (METU-MET) facilities which is the micromachining process used for fabricating the designed gyroscope.

3.1 Electromechanical Design

3.1.1 Conceptual Design

Figure 3.1 illustrates schematic view of the designed mode-decoupled tuning-fork gyroscope utilizing the proposed 2 DoF sense mode oscillator. In this figure k_1, k_2, and k_3 values are the sense mode oscillator spring constants that were demonstrated in Figure 2.17. Proof masses are the Coriolis coupling elements, therefore, they have freedom to oscillate both in x and y directions. On the other hand, drive frames are allowed to oscillate only in x direction, while the sense masses are allowed to oscillate only in y direction. Therefore, proof mass, which is m_1 of Figure 2.17,

both acts as the decoupling frame and the first mass of the 2 DoF oscillator owing to its dedicated flexible linkage design.

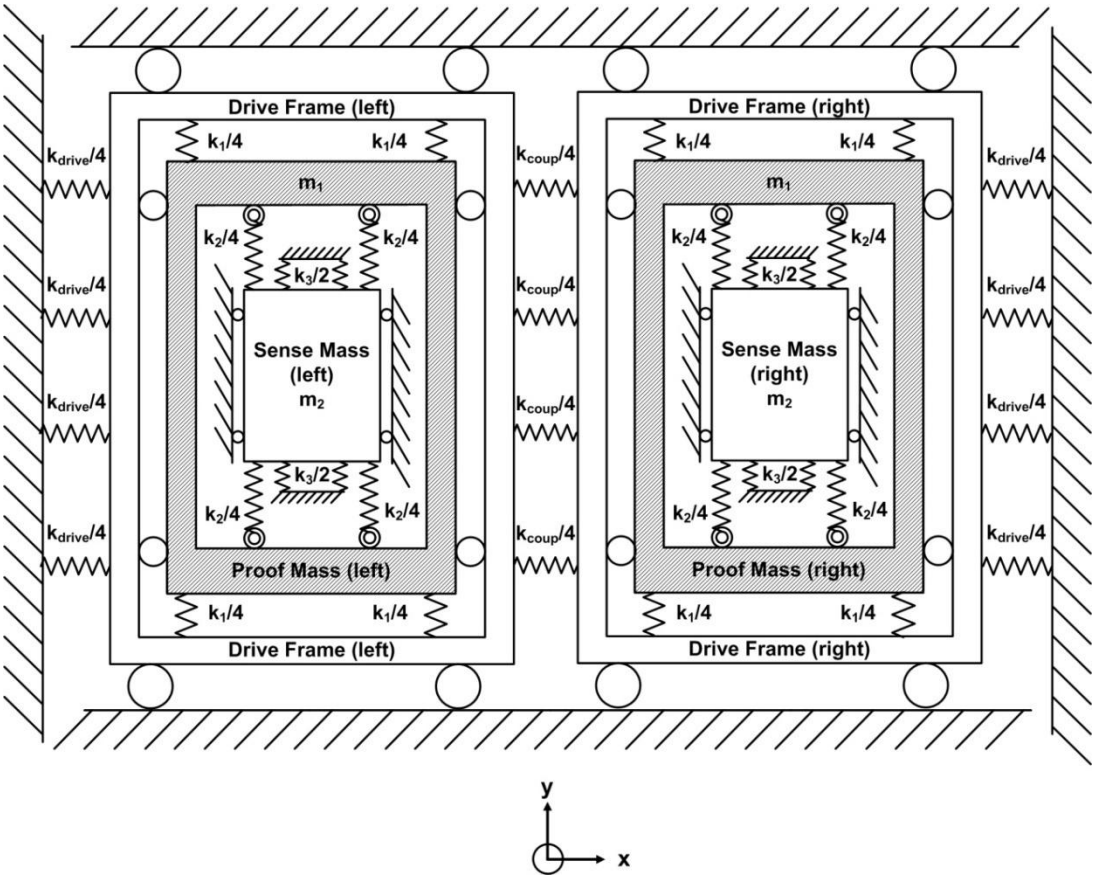

Figure 3.1: Schematic view of the designed mode-decoupled tuning-fork gyroscope utilizing the proposed 2 DoF sense mode oscillator.

Sense mode natural frequencies for the proposed 2 DoF oscillator have already been introduced in Equations 2.73 and 2.74. Proof mass and the drive frame oscillate together in the drive direction in this tuning-fork structure. During operation left and right drive mode oscillators are driven into anti-phase oscillations, therefore, the midpoint of the coupling springs act as the node of oscillations. Hence, Equation 3.1 expresses the natural frequency of drive mode oscillations considering only one of the drive mode oscillators, using system symmetry.

$$\varpi_{ndrive} = \sqrt{\frac{k_{drive} + 2k_{coupling}}{m_1 + m_{drive\ frame}}} \tag{3.1}$$

3.1.2 Physical Design

Figure 3.3 illustrates 2D layout of the physical structure. In this figure all photomask layers are shown, while Figure 3.3 shows only the structural layer. Abbreviations for separate silicon islands are annotated on the structural layer and Table 3.1 summarizes the descriptions of separate silicon islands observed on 2D layout of structural layer.

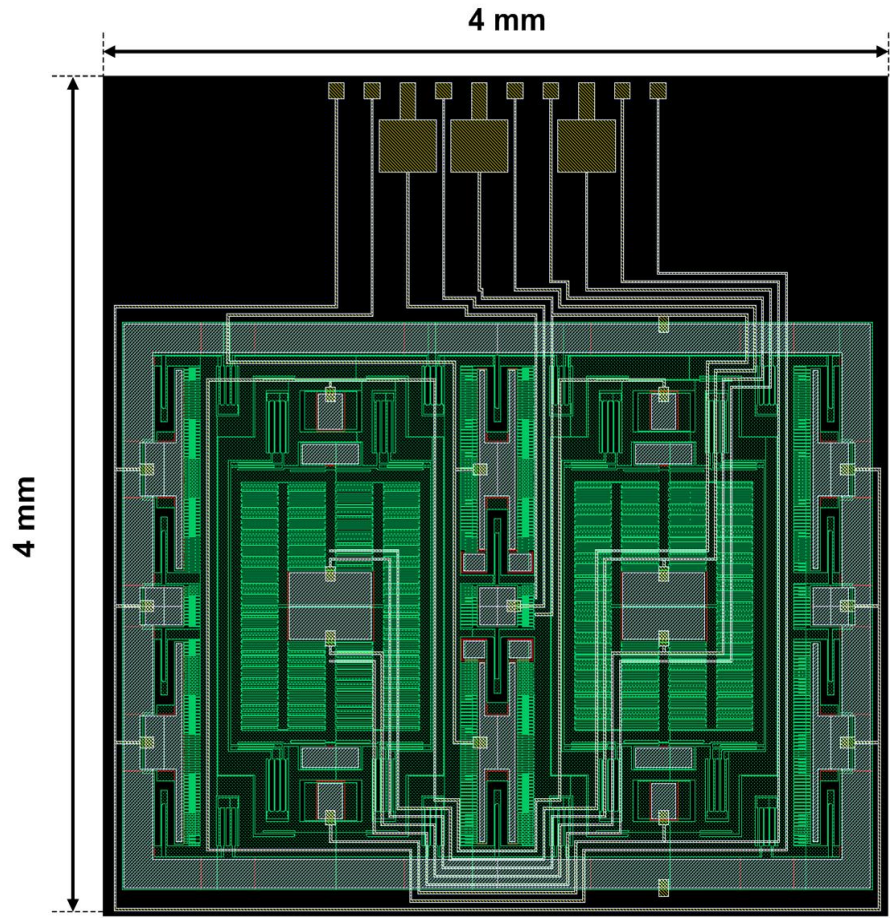

Figure 3.2: 2D layout of all photomask layers for the physical structure of the gyroscope.

Table 3.2 summarizes the electromechanical parameters extracted from the layout for the physical structure. When Table 3.2 is investigated it is observed that, the drive mode natural frequency is designed to be around 100000 rad/s as stated in Section 2.3.2. On the other hand, it is clear that drive mode frequency or the operation frequency of the gyroscope is not between the sense mode natural

frequencies. There are two reasons for this situation. First, it is observed in fabrication stage that sense mode flexible linkages are more prone to get thinner than designed, due to fabrication tolerances, than the drive mode flexible linkages. The result of thinning in linkages is a reduction in the designed spring constant. Therefore, it is expected that sense mode frequencies that are designed to be larger than operating frequency will reduce and get closer to operating frequency. Second, due to electrostatic spring effect mentioned in Section 2.6.2, the first sense mode resonance frequency can be tuned to be lower than the operating frequency, therefore, the drive mode frequency will remain in the flat-band region of sense mode oscillator frequency response. On the other hand, while sense mode resonance frequencies are tuned, second sense mode resonance frequency is not decreasing as fast as the first one. This results in an increase in the sense mode response bandwidth, with the cost of decreased sense mode mid-band sensitivity. Therefore, there is a need to characterize the fabrication tolerances in detail, so that an optimum window for the sense mode natural frequencies can be found. Then the design can be updated to achieve the highest SNR performance with sufficient operation bandwidth.

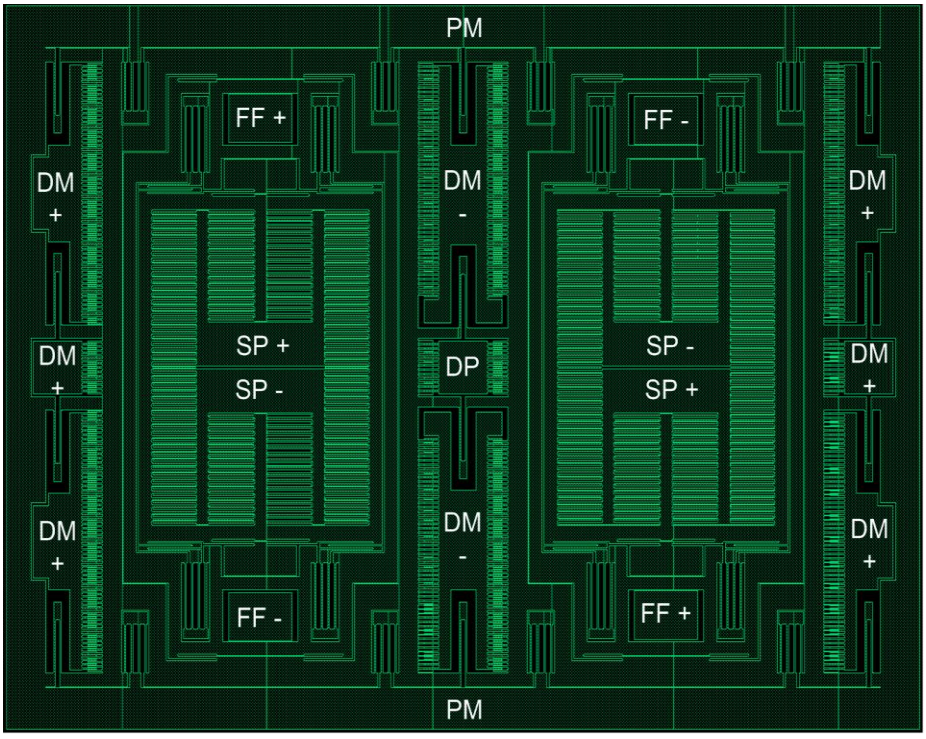

Figure 3.3: 2D layout of physical structure of the structural layer.

Table 3.1: Descriptions of the silicon islands on 2D layout of structural layer.

Silicon Island	Description
PM	Proof mass. This silicon piece contains all the movable parts of the structure, in addition to the outer anchor frame.
DM	Comb drive actuators to drive PM into oscillations in x direction. There are two opposite polarities; therefore, the structure can be driven into oscillations differentially.
DP	Capacitive comb structure to measure the amplitude of drive mode oscillations. This measurement is fed to the external drive mode closed loop amplitude control circuit, which controls amplitude of drive mode oscillations by varying electrical signals applied to DM electrodes.
SP	Capacitive comb structures to measure the amplitude of induced sense mode oscillations. There are two opposite polarities; therefore, the sense mode oscillations can be measured differentially. Differential readout scheme is aimed to cancel sense mode deflections due to common mode external accelerations.
FF	Electrostatic actuator used for force feedback type sense mode readout scheme. Force feedback type sense mode control circuit generates required amount of force to damp the oscillations in sense mode, by applying signal to FF electrodes. From the amplitude of the electrical signal applied to FF, angular rate applied to the gyroscope is extracted. As differential sense mode readout scheme is utilized, there are two polarities of FF electrodes. Open-loop sense mode readout circuits are utilized in this research study; therefore, FF electrodes are not used in operation. On the other hand, FF electrodes are used to drive the sense mode into oscillations during sense mode oscillator characterization.

Table 3.2: Electromechanical design parameters for the presented physical structure.

Parameter	Value	Parameter	Value
$m_{drive\ frame}$	189 μg	$m_{proof\ mass} = m_1$	128 μg
$m_{sense\ mass} = m_2$	106 μg	k_{drive}	2230 *N/m*
$k_{coupling}$	3262 *N/m*	k_1	2230 *N/m*
k_2	269 *N/m*	k_3	1710 *N/m*
ϖ_{ndrive}	109975 *rad/s*	f_{ndrive}	17500 *Hz*
$\varpi_{n1,sense}$	132366 *rad/s*	$f_{n1,sense}$	21066 *Hz*
$\varpi_{n2,sense}$	136445 *rad/s*	$f_{n2,sense}$	21715 *Hz*
C_{DM}	4.18 *pF*	$\frac{\partial C_{DM}}{\partial x}$	11.9 $\mu F/m$
C_{DP}	372 *fF*	$\frac{\partial C_{DP}}{\partial x}$	10.6 *nF/m*
C_{SP}	6.11 *pF*	$\frac{\partial C_{DP}}{\partial y}$	1.53 $\mu F/m$

Figure 3.4 presents the 3D view of the structural layer. The thickness of the structural layer is 100 µm, owing to SOG process.

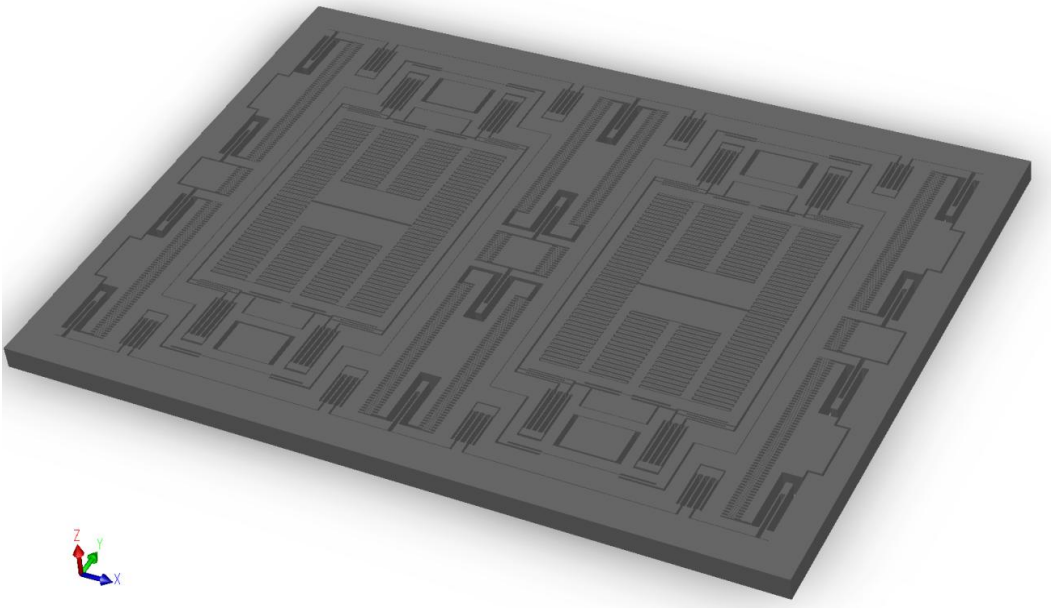

Figure 3.4: 3D view of the structural layer of designed robust tuning-fork gyroscope.

3.2 Verification of Electromechanical Design via FEA Simulations

Firstly, the mode shapes of the mechanical structure need to be simulated as the most important parameters of mechanical design are the natural frequencies of the drive and sense modes. In addition to verification of analytical calculations, unwanted oscillation modes that may cause unstable oscillations can be detected and precautions to eliminate those by structural modifications can be taken. Moreover, nonlinearities due to large deformations, spring stiffening effects, and small but finite elasticity for all silicon plates; that are not considered in analytical calculations are of concern in FEA calculations. Therefore, properly performed FEA simulations give more accurate estimations of mechanical design parameters. For mechanical FEA simulations ANSYS 11 package is used. Symmetries of a structure need to be utilized to simplify the mathematical model in an FEA study, in order to perform accurate simulations with fine FEA meshes within the computational capabilities of even today's high performance computers. Therefore, only the left half of the gyroscope structure is analyzed in this research. Moreover, electrostatic comb structures are replaced with equivalent mass plates to use computational resources effectively. Figure 3.5, Figure 3.6, and Figure 3.7 demonstrate first three oscillation modes of the mechanical structure at room temperature, which are the drive, in-phase sense and out-of phase sense modes, respectively. The deflections are exaggerated for clarity on mode shape figures. Table 3.3 lists analytically calculated and FEA simulated mode frequencies for comparison purposes.

Table 3.3: Analytically calculated and simulated mode frequencies.

Oscillation Mode	**FEA Simulated Frequency (Hz)**	**Analytically Calculated Frequency (Hz)**
Drive mode	16747	17500
Sense mode 1 (in-phase)	21343	21066
Sense mode 2 (out-of-phase)	24147	21715

It is observed from Table 3.3 that, drive mode frequency, which is the operating frequency of the gyroscope, is 16747 Hz. Moreover, it is clear that, bandwidth of sense mode oscillator is greater than designed. On the other hand, as stated earlier, this high bandwidth is required for safety purposes, as the fabrication tolerances are limiting the ability to optimize the bandwidth. Fourth oscillation mode is at 32875 Hz, which is far away from the operating frequency. Therefore, risk of unstable oscillations due to unwanted oscillation modes is minimized in this design, owing to its dedicated flexible linkage elements that very well define the allowed oscillation axes.

Then modal analyses are performed at varying temperatures in order to examine the effects of thermal expansion on mode frequencies. Table 3.4 summarizes the results of those simulations.

Table 3.4: Mode frequencies simulated at varying temperatures.

Oscillation Mode	**FEA Simulated Frequency at varying T (Hz)**								
	10 °C	**20 °C**	**25 °C**	**30 °C**	**40 °C**	**50 °C**	**60 °C**	**70 °C**	**80 °C**
Drive mode	16743	16748	16747	16744	16730	16704	16665	16609	16537
Sense mode 1	21345	21344	21343	21343	21341	21340	21338	21335	21332
Sense mode 2	24169	24155	24147	24139	24122	24105	24087	24069	24051
4^{th} Mode	32891	32882	32875	32866	32840	32803	32753	32690	32613
5^{th} Mode	61758	61754	61751	61749	61744	61738	61732	61726	61720
6^{th} Mode	68827	68827	68827	68827	68827	68827	68827	68827	68827
7^{th} Mode	71282	71280	71280	71279	71278	71276	71275	71273	71271
8^{th} Mode	71470	71471	71472	71472	71474	71476	71477	71479	71481
9^{th} Mode	71630	71630	71630	71630	71630	71630	71630	71630	71630
10^{th} Mode	72029	72028	72028	72027	72026	72025	72024	72023	72022

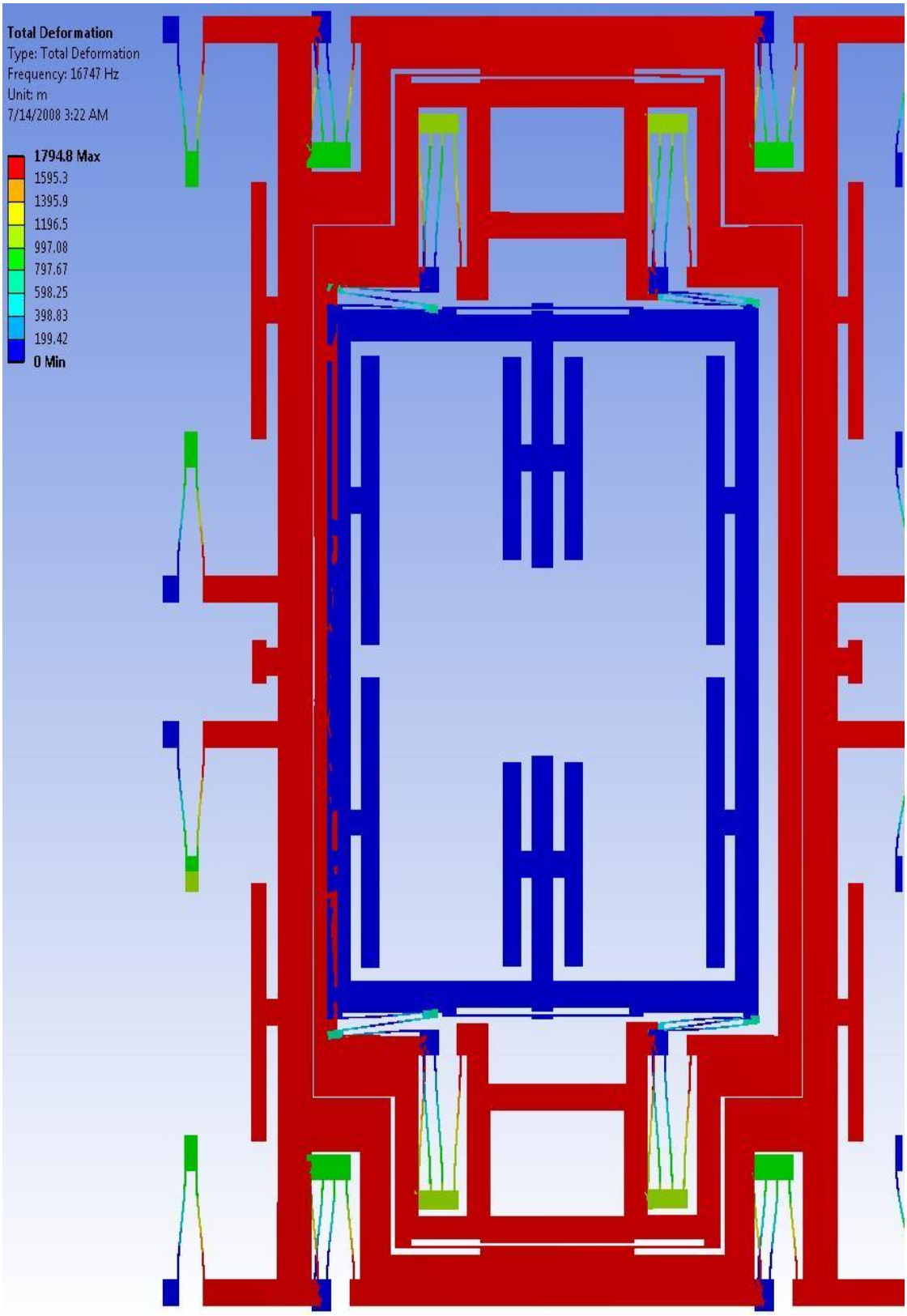

Figure 3.5: Mode shape of first oscillation mode, which is the drive mode, at 16747 Hz.

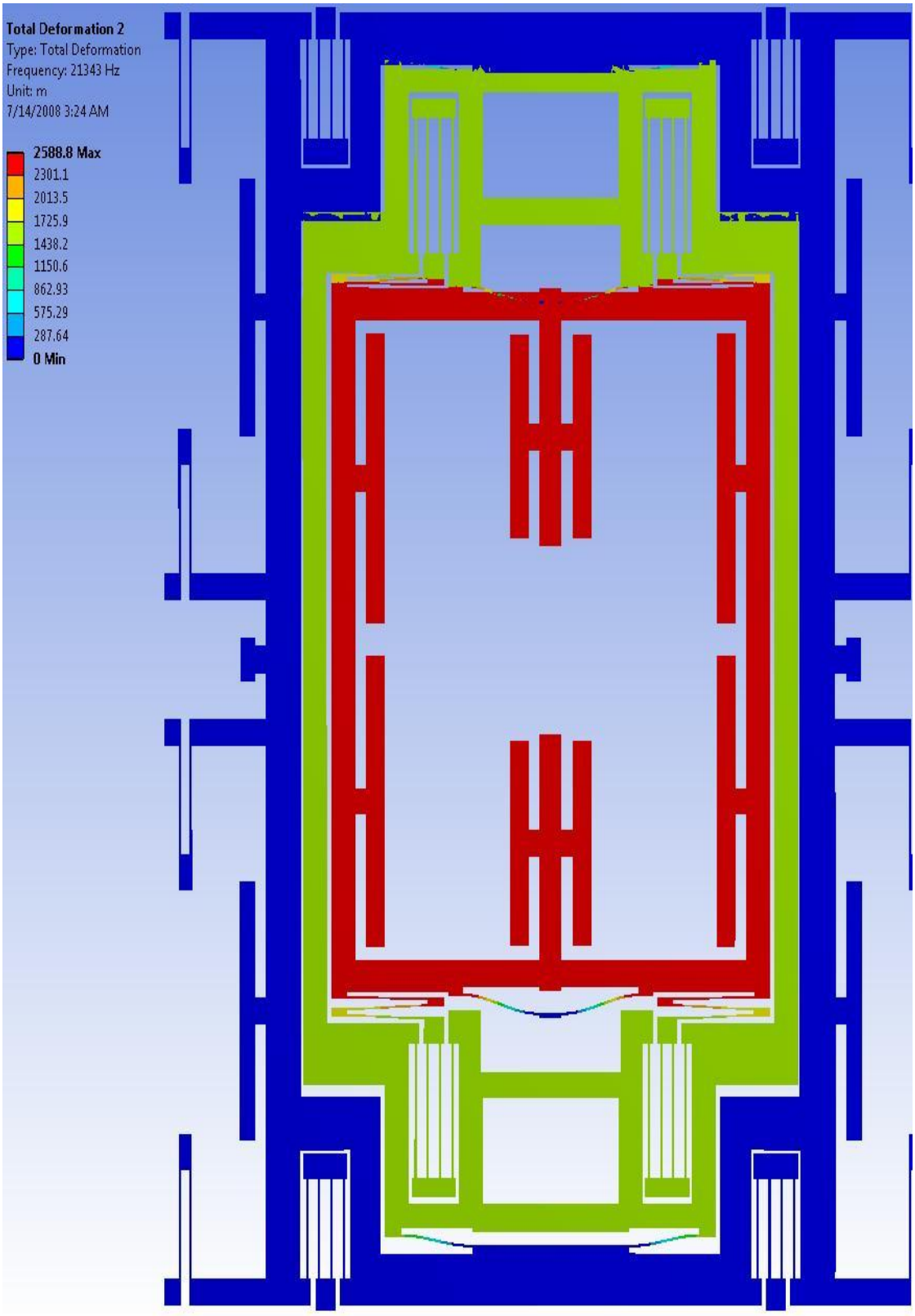

Figure 3.6: Mode shape of second oscillation mode, which is the in-phase sense mode, at 21343 Hz.

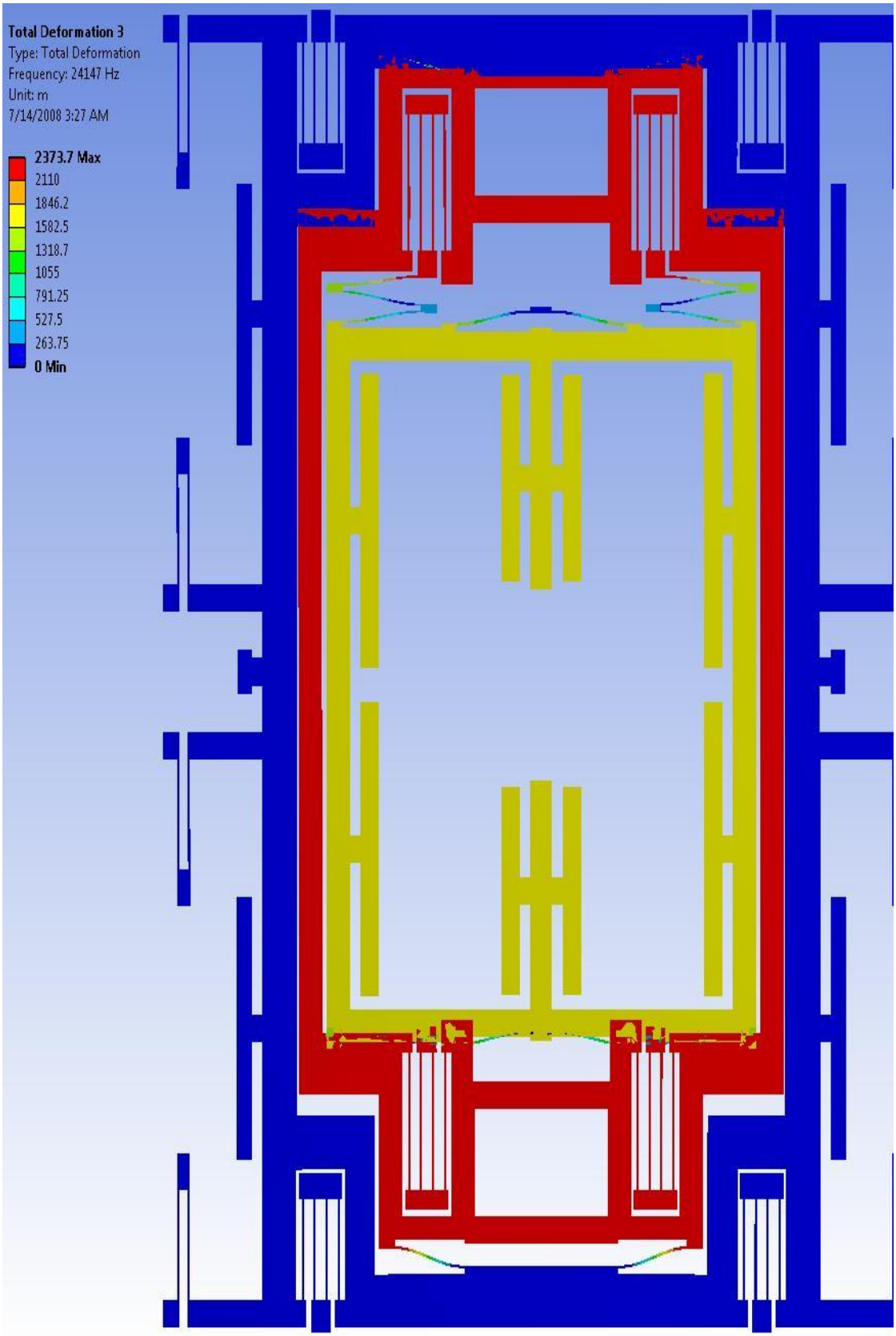

Figure 3.7: Mode shape of third oscillation mode, which is the out-of-phase sense mode, at 24147 Hz.

It is observed from Table 3.4 that, thermal expansion of the mechanical structure affects the frequencies of oscillation modes slightly. On the other hand, unwanted oscillation modes do not slide into the operating frequency region, verifying structure's immunity to ambient temperature variations. Moreover, sense mode oscillator mode frequencies vary in same proportion with temperature, therefore, mechanical sensitivity of the designed mechanical structure can be said to be independent of temperature changes. As a result, robustness to temperature variations is limited by the sensitivity of closed-loop drive mode amplitude control and open-loop sense mode readout circuits for this gyroscope.

Next, response of the structure to external acceleration loads of 1000 g in x, y and z axes need to be examined in order to verify shock survivability of the structure. Single crystal silicon used in SOG process is a brittle material with an ultimate tensile strength of 7 GPa, owing to its perfect crystalline structure. Hence, maximum von Mises stress under g loading should not exceed 7 GPa. Moreover, maximum permitted deflection in x and y axes before a collision with the anchored silicon islands are 10 μm and 2 μm, respectively. Figures 3.8, 3.9 and 3.10 illustrate maximum deformation and von Mises stresses under 1000 g acceleration loading, and verify g survivability of the design.

Capacitance values for intentionally generated capacitive structures have already been calculated in electromechanical design phase. On the other hand, there are two types of parasitic capacitances, in addition to the analytically calculated capacitance values. Those parasitic capacitances affect the performance of drive mode amplitude control and sense mode readout circuits, therefore, parasitic capacitance values extracted through FEA simulations need to be utilized in electronics design study, which is out of scope of this research study. In this research study electrostatic FEA solver of CoventorWare software package is used for extracting parasitic capacitance values.

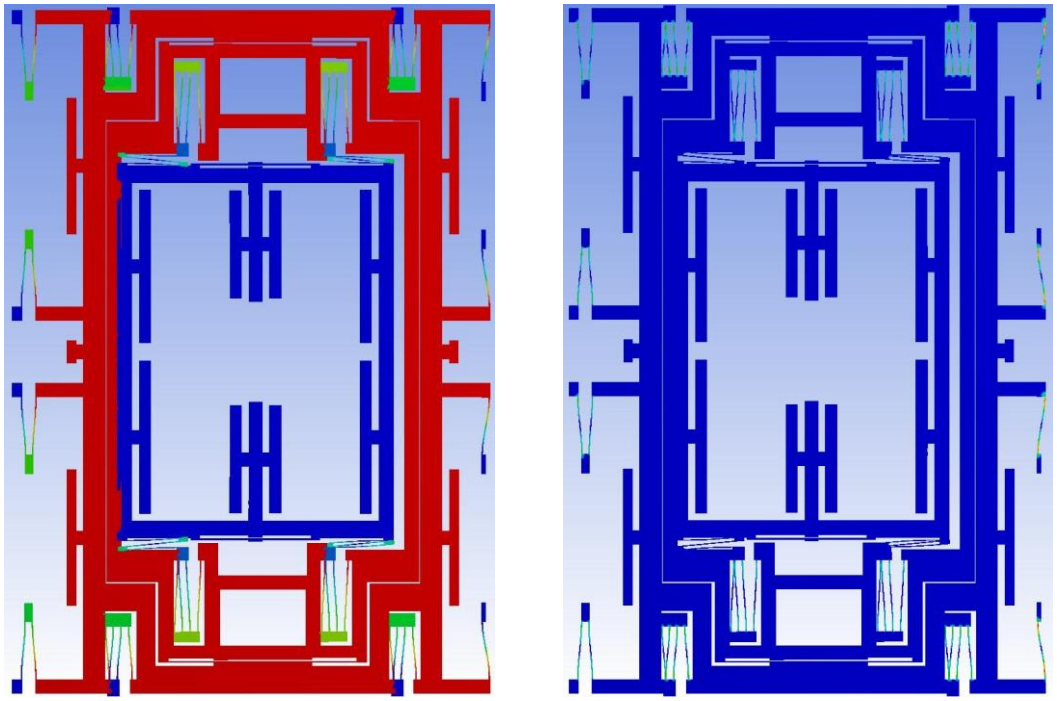

(a) **(b)**

Figure 3.8: Response to 1000 g in x direction (a) deformation plot (maximum 0.92 μm) (b) von Mises stress plot (maximum 57.5 MPa).

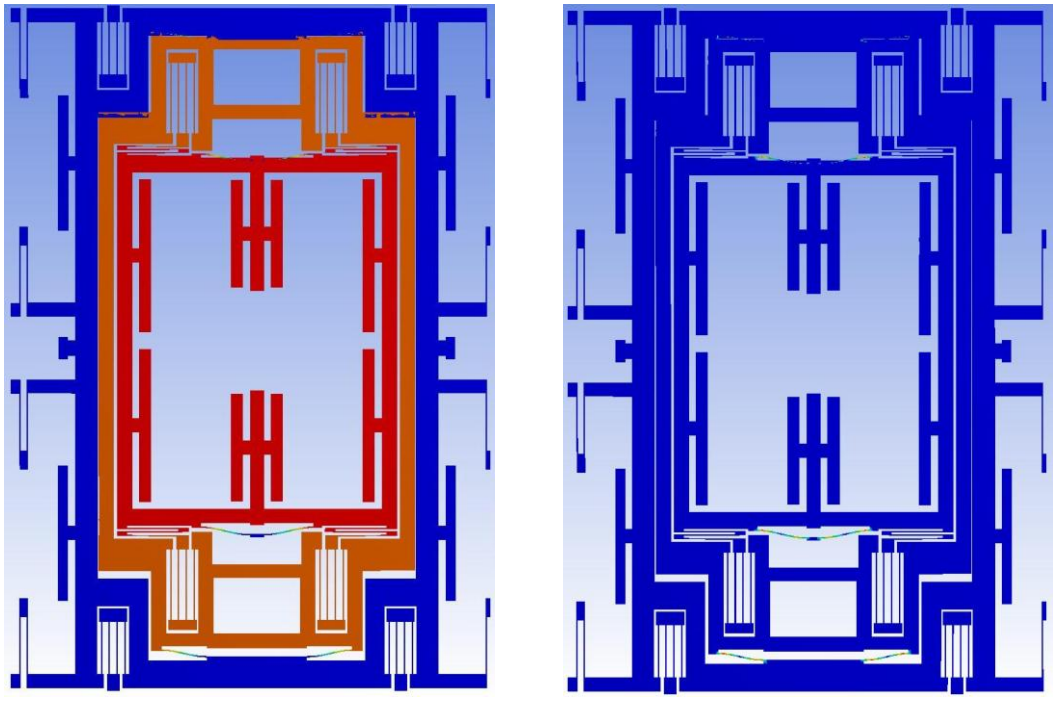

(a) **(b)**

Figure 3.9: Response to 1000 g in y direction (a) deformation plot (maximum 0.59 μm) (b) von Mises stress plot (maximum 49.7 MPa).

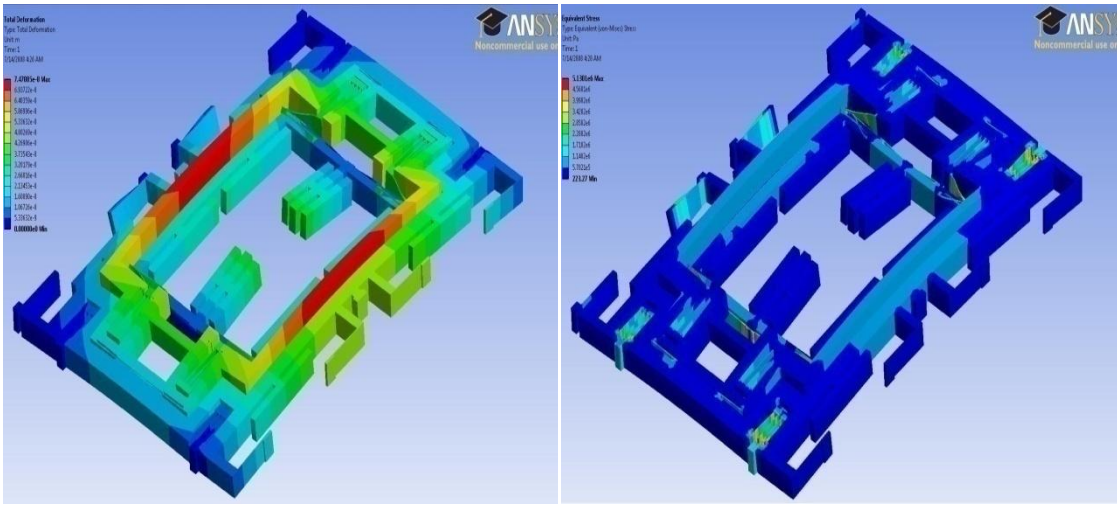

(a) **(b)**

Figure 3.10: Response to 1000 g in z direction (a) deformation plot (maximum 0.07 μm) (b) von Mises stress plot (maximum 5.1 MPa).

First of the sources of parasitic capacitances is the electrostatic fields between separate silicon islands of structural layer, while the second parasitic capacitance source is the electrostatic fields between metal routings. In FEA study of structural layer, capacitive comb structures are taken out of the electrostatic model and an FEA model shown in Figure 3.11 is used. Table 3.5 summarizes the cumulative silicon structural layer parasitic capacitances, referred to the electrodes, while Table 3.6 summarizes the cumulative metallization layer parasitic capacitances, referred to the electrodes.

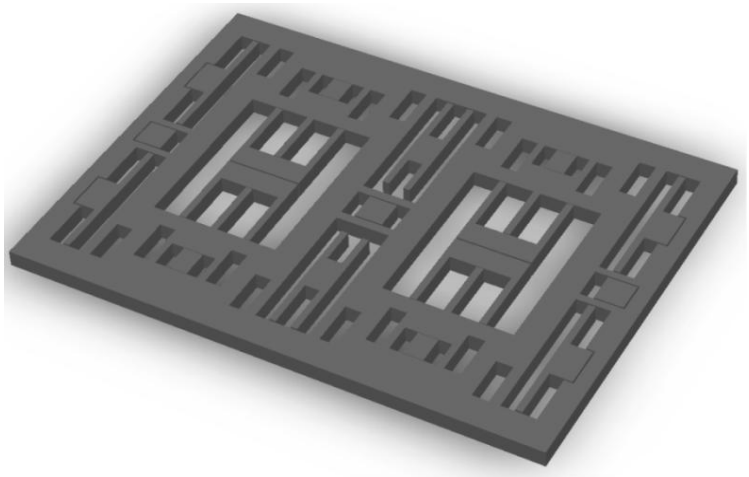

Figure 3.11: 3D view of the FEA model used in extracting structural layer parasitic capacitances.

Table 3.5: Cumulative silicon structural layer parasitic capacitances referred to the electrodes.

Capacitance Matrix (pF)								
Electrode	**PM**	**SP-**	**DM+**	**SP+**	**FF+**	**DP+**	**DM-**	**FF-**
PM		-1.57E-1	-1.24E-1	-1.57E-1	-2.13E-1	-5.70E-2	-5.19E-1	-2.12E-1
SP-	-1.57E-1		-1.23E-3	-1.05E-1	-8.48E-5	-2.38E-4	-1.50E-3	-3.07E-4
DM+	-1.24E-1	-1.23E-3		-1.23E-3	-1.29E-4	-8.90E-4	-5.37E-4	-1.29E-4
SP+	-1.57E-1	-1.05E-1	-1.23E-3		-3.07E-4	-2.38E-4	-1.50E-3	-8.48E-5
FF+	-2.13E-1	-8.48E-5	-1.29E-4	-3.07E-4		-9.63E-6	-1.53E-4	-6.71E-6
DP+	-5.70E-2	-2.38E-4	-8.90E-4	-2.38E-4	-9.63E-6		-5.73E-5	-9.62E-6
DM-	-5.19E-1	-1.50E-3	-5.37E-4	-1.50E-3	-1.53E-4	-5.73E-5		-1.53E-4
FF-	-2.12E-1	-3.07E-4	-1.29E-4	-8.48E-5	-6.71E-6	-9.62E-6	-1.53E-4	

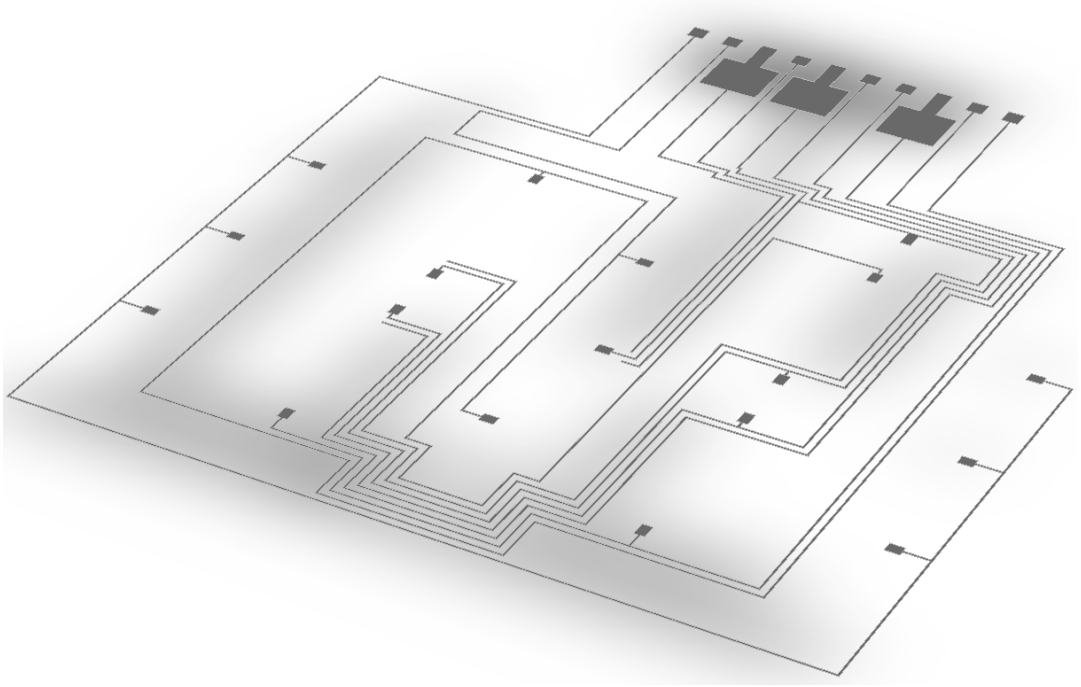

Figure 3.12: 3D view of the FEA model used in extracting metallization parasitic capacitances.

Table 3.6: Cumulative metallization parasitic capacitances referred to the electrodes.

Capacitance Matrix (pF)								
Electrode	**PM**	**SP-**	**DM+**	**SP+**	**FF+**	**DP+**	**DM-**	**FF-**
PM		-3.70E-2	-1.16E-2	-1.34E-2	-2.07E-2	-5.32E-3	-4.88E-2	-5.28E-2
SP-	-3.70E-2		-5.92E-3	-5.73E-3	-1.47E-2	-2.15E-3	-1.16E-2	-2.03E-2
DM+	-1.16E-2	-5.92E-3		-3.59E-2	-1.85E-3	-1.12E-3	-8.21E-3	-6.30E-2
SP+	-1.34E-2	-5.73E-3	-3.59E-2		-2.74E-3	-2.16E-3	-4.86E-3	-6.86E-2
FF+	-2.07E-2	-1.47E-2	-1.85E-3	-2.74E-3		-2.68E-3	-1.43E-3	-1.61E-2
DP+	-5.32E-3	-2.15E-3	-1.12E-3	-2.16E-3	-2.68E-3		-6.74E-4	-3.59E-2
DM-	-4.88E-2	-1.16E-2	-8.21E-3	-4.86E-3	-1.43E-3	-6.74E-4		-3.24E-2
FF-	-5.28E-2	-2.03E-2	-6.30E-2	-6.86E-2	-1.61E-2	-3.59E-2	-3.24E-2	

3.3 Fabrication of the Designed Gyroscope

Figure 3.13 illustrates steps of the in-house silicon-on-glass (SOG) micromachining process with metal etch stop for deep reactive ion etching (DRIE), developed by Dr.Said Emre Alper [11]. This microfabrication process is utilized to implement the designed novel 2 DoF sense mode tuning-fork gyroscope, and fabrication of prototypes are performed by Dr. Said Emre Alper and METU-MET staff.

In-house SOG process starts with a blank pyrex glass wafer with a thickness of 500 μm. In the first step, anchor regions on the pyrex wafer are generated. For the second step, a thinned blank (111) silicon wafer with a thickness of 100 μm is coated with Cr-Au on back side. Then, Cr-Au layer is patterned to form the DRIE etch stop layer. In the third step, processed pyrex and silicon wafers are anodically bonded to each other. Fourth step starts with coating of silicon wafer with a Cr-Au layer. Then Cr-Au layer is patterned to form the interconnect metallizations. After the photoresist mold for DRIE is prepared and patterned, step 5 which is the DRIE patterning starts. DRIE patterning forms the suspended movable structures of the gyroscope. DRIE patterning continues until it reaches the Cr-Au etch stop layer.

This metal etch stop layer aids in preventing notching at the back side of silicon wafer by conducting out the heat generated during DRIE process, so that the structural layer is cooled properly. Metal etch stop layer and the photoresist mold are stripped at the last step, so that a suspended structural layer with on top interconnect metallization is obtained. One of the advantages of this SOG process is that, it does not require back etching. Moreover, the structural layer has a thickness of 100 μm, which allows eliminating unnecessary oscillation modes in out of plane direction easily with proper flexible linkage design, while giving designer the freedom to concentrate on in plane oscillation modes. On the other hand, undercutting of flexible linkages due to poor DRIE tolerances need to be examined in order to design an optimum gyroscope which shows sufficient operation bandwidth with high mechanical sensitivity.

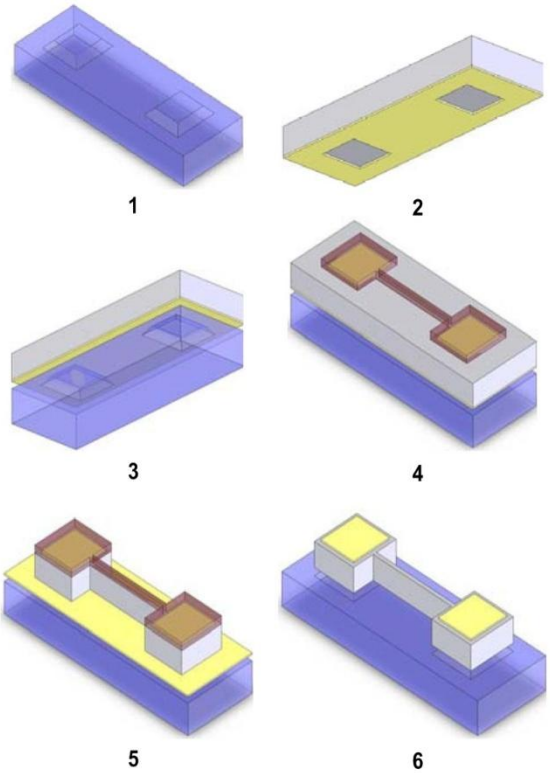

Figure 3.13: Steps of in-house silicon-on-glass (SOG) micromachining process with metal etch stop for DRIE patterning [11].

Figure 3.14 shows the photograph, Figure 3.15, Figure 3.16, and Figure 3.17 show the SEM images of the fabricated gyroscope.

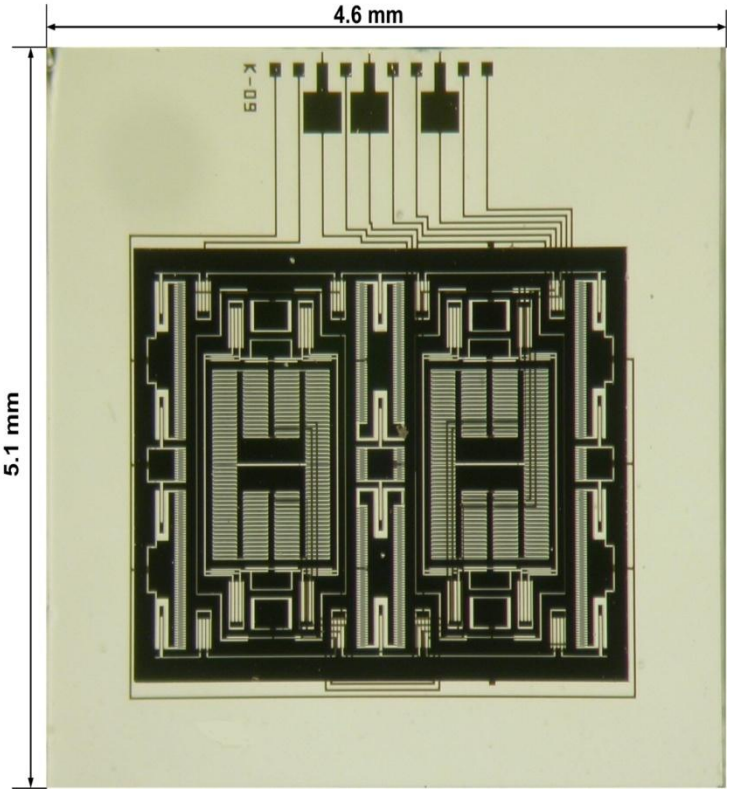

Figure 3.14: Photograph of the fabricated gyroscope.

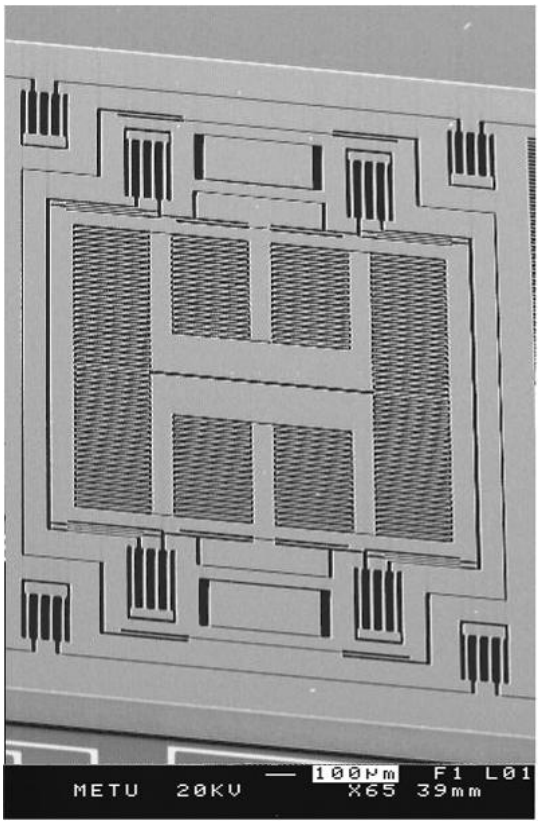

Figure 3.15: SEM image of one half of the fabricated gyroscope.

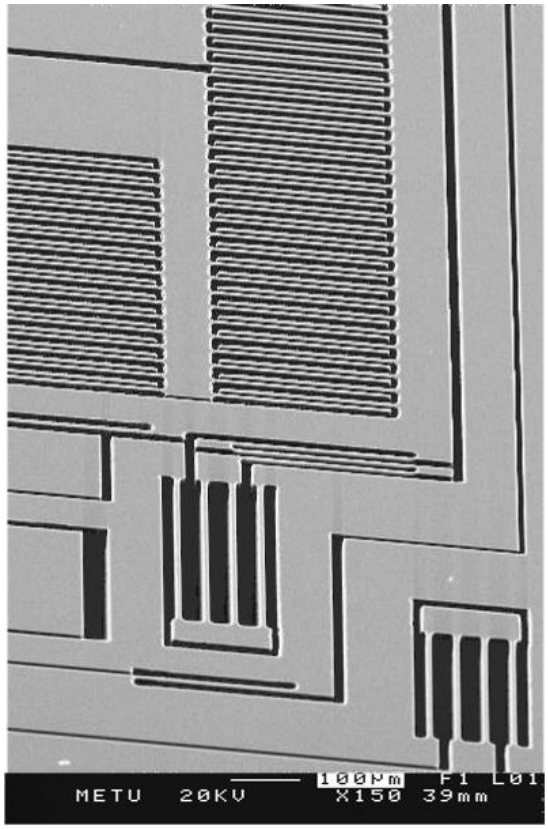

Figure 3.16: SEM image of the 2 DoF spring structure utilized in the designed gyroscope.

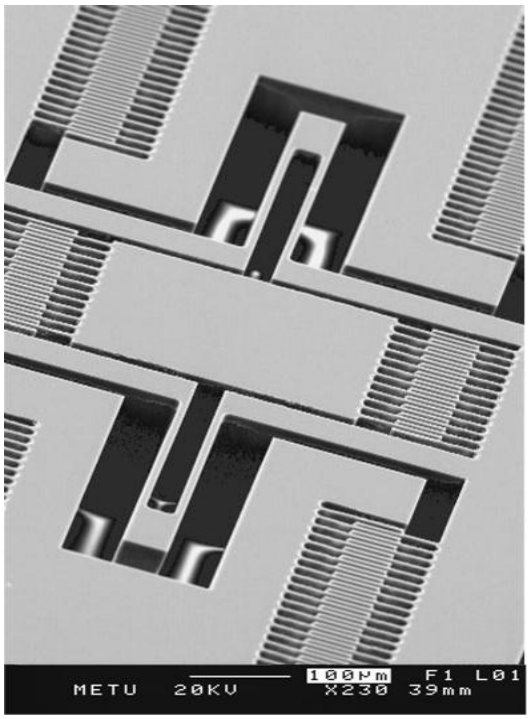

Figure 3.17: SEM image demonstrating the thickness of the structural layer, in addition to high aspect ratio flexible linkage structures.

3.4 Summary

This chapter presented the electromechanical design and fabrication of the proposed gyroscope. It demonstrated the conceptual design and physical design phases, in addition to the FEA simulations for verification of design parameters. Moreover, this chapter demonstrated the FEA simulations carried on to investigate the effects of thermal expansion and parasitic capacitances on the performance of the designed gyroscope. The details of the in-house developed SOG fabrication process used in the fabrication of the proposed gyroscope are also presented in this chapter. The chapter is concluded with the photograph and SEM images of the fabricated gyroscope.

CHAPTER 4

CHARACTERIZATION OF THE DESIGNED GYROSCOPE

This chapter presents the characterization procedure followed to measure the performance parameters of a fabricated gyroscope, in addition to the test results of the fabricated wide-bandwidth high-sensitivity tuning-fork, mode-decoupled micromachined vibratory gyroscope. Section 4.1 demonstrates the probe tests performed to separate the working prototypes from the failing ones. The hybrid package that the gyroscope is mounted on is also demonstrated in this section. Section 4.2 deals with the operational tests for a micromachined vibratory gyroscope. Operation bandwidth, scale factor, scale factor linearity, dependence of scale factor to ambient vacuum conditions, long term bias stability, and angle random walk of the complete angular rate measurement system (ARMS) are extracted from the operational tests. Moreover, Section 4.2 summarizes the measured performance parameters of the designed wide-bandwidth, high sensitivity, tuning-fork, mode-decoupled gyroscope based on the proposed 2 DoF sense mode oscillator. The chapter is concluded by performance comparison presented in Section 4.3.

4.1 Probe Tests and Hybrid Packaging

First step in characterization of fabricated gyroscopes is the measurement of the frequency response characteristics of the gyroscope both in drive and sense modes, in order to separate the working prototypes from the failing ones. Figure 4.1 shows this rough measurement performed using the probe station and network analyzer under atmospheric pressure condition. Figure 4.2 shows the connection of the

network analyzer to the designed gyroscope to measure drive mode frequency response characteristics.

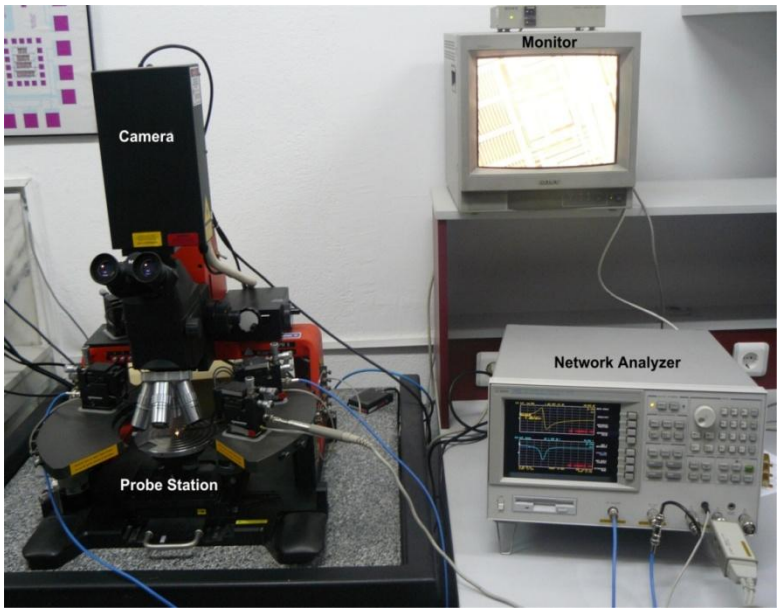

Figure 4.1: Setup used for the probe tests of gyroscopes**.**

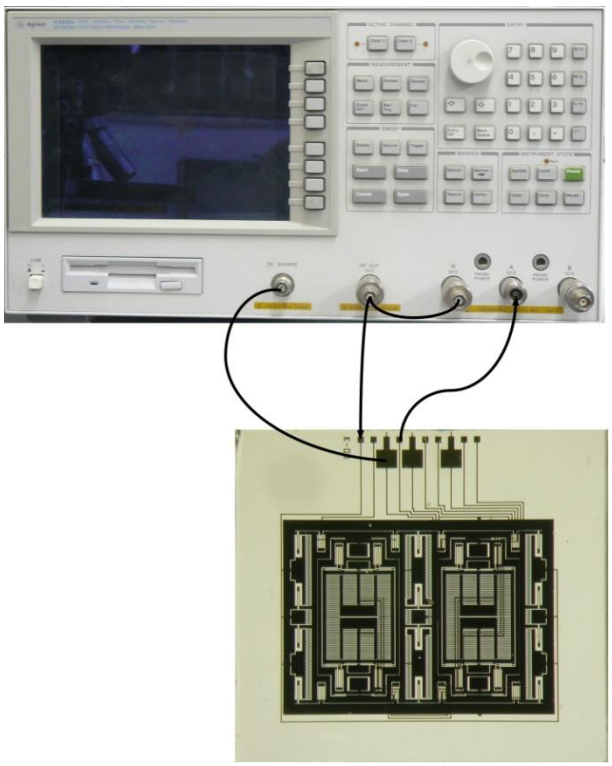

Figure 4.2: The connection of the network analyzer to the designed gyroscope to measure drive mode frequency response characteristics.

Next, working prototypes are mounted on a platform package and hybrid connected to preamplifiers using a glass substrate developed by Dr. Said Emre Alper. Figure 4.3 shows a gyroscope prototype hybrid connected to preamplifiers on the platform package.

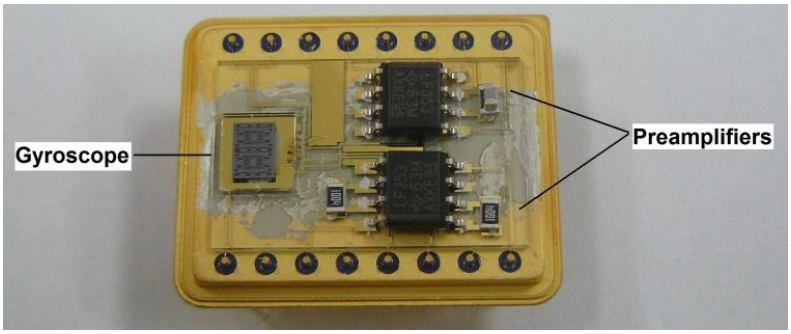

Figure 4.3: A gyroscope hybrid connected to preamplifiers on a platform package.

After the gyroscope is packaged, it gets ready for characterization under vacuum conditions. Figure 4.4 shows the test setup used for all tests under vacuum conditions.

Figure 4.4: Test setup used for all tests under vacuum conditions.

First tests performed under vacuum conditions are the frequency response characterization of the drive and sense mode oscillators, by using the dynamic signal analyzer. Figure 4.5 shows the connection of the dynamic signal analyzer and the DC power supply to the gyroscope under test, in order to obtain drive mode frequency response characteristics. Figure 4.6 demonstrates the drive mode frequency response, measured at 20 V proof mass voltage (V_{PM}) under 25 mTorr vacuum condition. Operating frequency of the gyroscope is measured to be 15155 Hz with a drive mode quality factor of 8760.

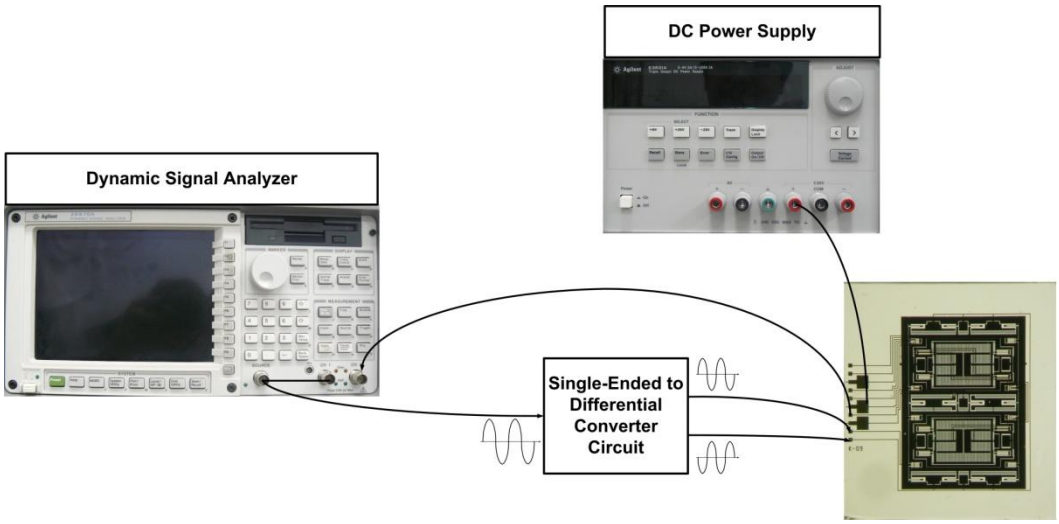

Figure 4.5: The connection of the dynamic signal analyzer and the DC power supply to the gyroscope under test in order to obtain drive mode frequency response characteristics.

Figure 4.7 demonstrates measured sense mode frequency response curves for varying V_{PM} voltages, at 25 mTorr vacuum ambient. It is clear that, as V_{PM} increases the flat-band of the sense mode oscillator gets wider, as expected, due to the electrostatic spring effect mentioned in Section 2.6.2.

Next, frequency response characteristics of designed 2 DoF sense mode oscillator for varying vacuum levels are measured. Figure 4.7 demonstrates the magnitude frequency response curves for the designed 2 DoF sense mode oscillator measured at V_{PM} = 35 V for varying vacuum conditions. It is clear that, sense mode response around the operating frequency of the gyroscope (15155Hz) is almost constant for varying vacuum conditions, verifying the immunity of the gyroscope to ambient

pressure variations. Flat-band region of the sense mode response curve extends up to 2.5 kHz, which can be the maximum system bandwidth provided that the operating frequency of the gyroscope is set to 16.25 kHz.

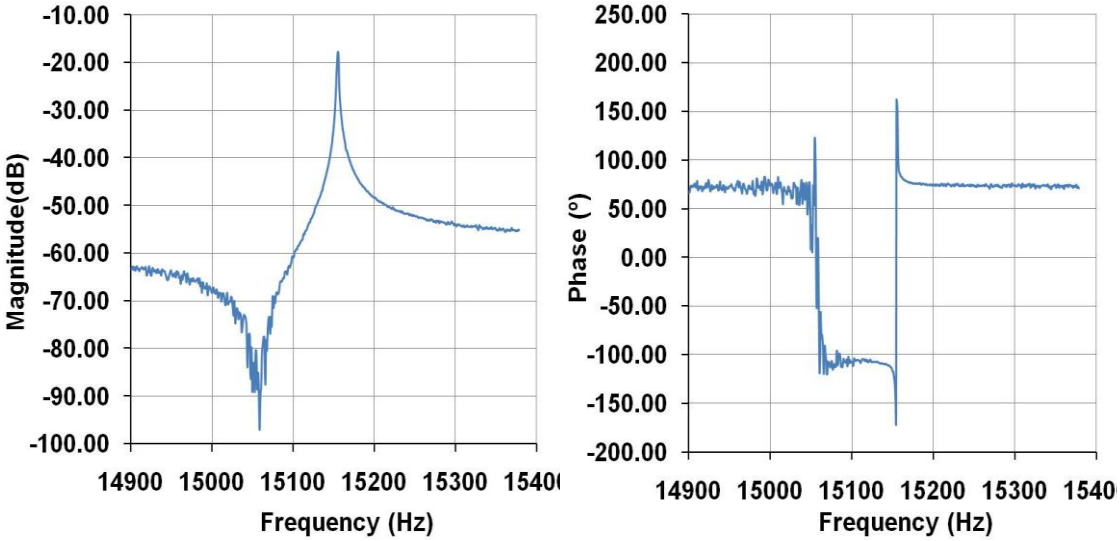

(a) **(b)**

Figure 4.6: Drive mode frequency response characteristics measured at 20 V proof mass voltage (V_{PM}) under 25 mTorr vacuum condition (a) magnitude plot and (b) phase plot.

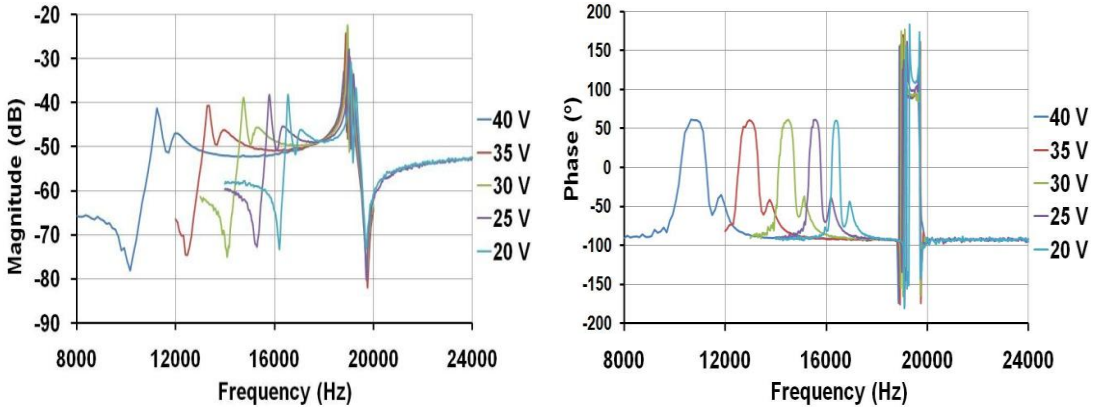

(a) **(b)**

Figure 4.7: Sense mode frequency response characteristics measured for varying proof mass voltages at 25 mTorr vacuum ambient (a) magnitude plot and (b) phase plot.

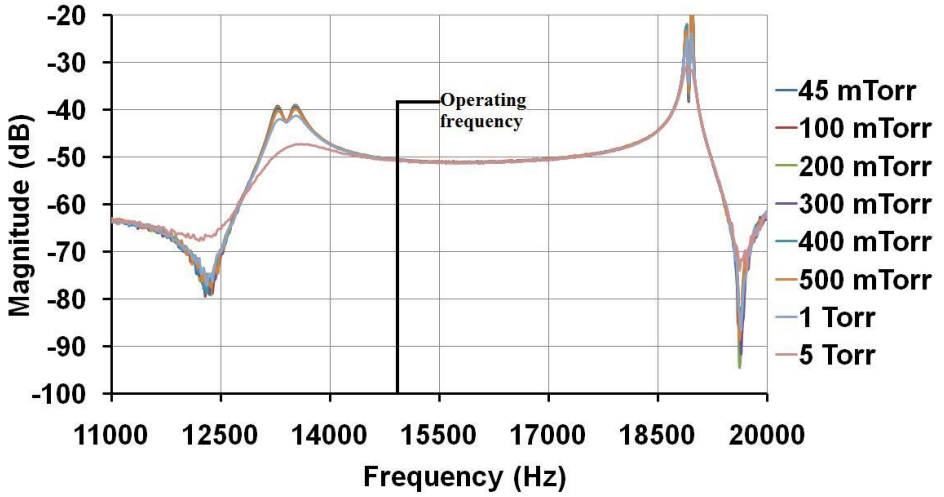

Figure 4.8: Magnitude frequency response curves for the designed 2 DoF sense mode oscillator measured at V_{PM} = 35 V for varying vacuum conditions.

The pressure level at the vacuum chamber of the rate table is precisely controlled via a needle valve connected to the vacuum pump. Figure 4.9 shows the vacuum pump, needle valve assembly externally connected to the vacuum chamber of the rate table.

Figure 4.9: Vacuum pump, needle valve assembly externally connected to vacuum chamber of rate table.

4.2 Operational Tests

After the characterization of drive and sense mode oscillators, the gyroscope is connected to external closed-loop drive mode amplitude control and open-loop sense mode readout electronics developed by Mr. Emre Şahin to form the complete ARMS.

Figure 4.10 shows the measured DC voltage output of the ARMS in response to constant angular rate inputs from zero-rate up to ±100 ◦/s using 10 ◦/s steps and then back to zero-rate, at 35V proof mass voltage under 40mTorr vacuum condition.

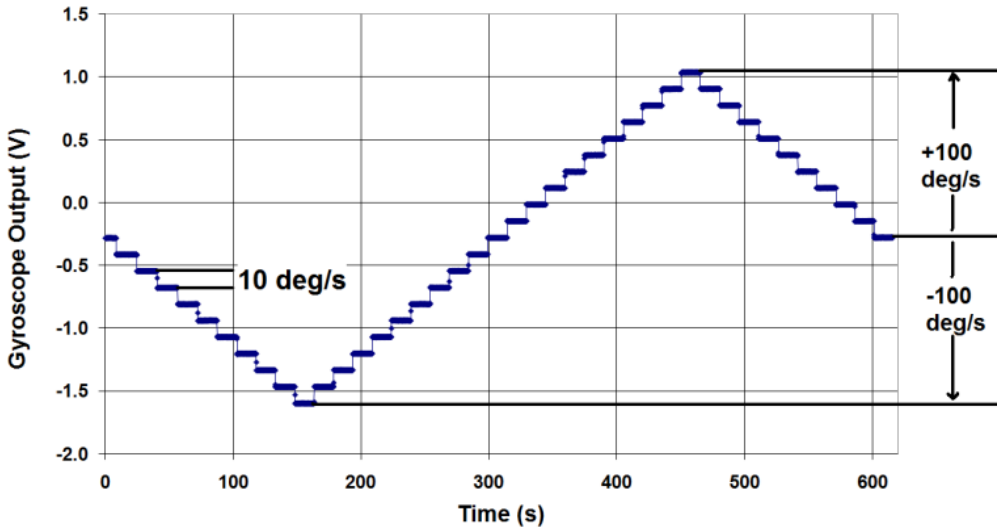

Figure 4.10: Measured DC voltage output of the ARMS in response to constant angular rate inputs from zero-rate up to ±100 ◦/s using 10 ◦/s steps and then back to zero-rate.

Figure 4.11 demonstrates the measured scale factor and R^2-linearity of the output response of the ARMS. The system demonstrates a scale factor of 13.1 mV/(◦/s) in a measurement range of ±100 ◦/s, with 40 dB amplification of the raw sense mode output. The R^2-linearity of the measured scale factor is better than 0.01 % within ±100 ◦/s full scale.

Table 4.1 summarizes the measured scale factor, R^2-nonlinearity, and maximum percent deviation nonlinearity which is defined as the maximum percent deviation

from the best straight line fit for varying ambient pressures from 40 mTorr to 500 mTorr. The maximum variation in the scale factor of the gyroscope is measured to be less than 0.38 %, proving the immunity of the gyroscope against ambient pressure variations.

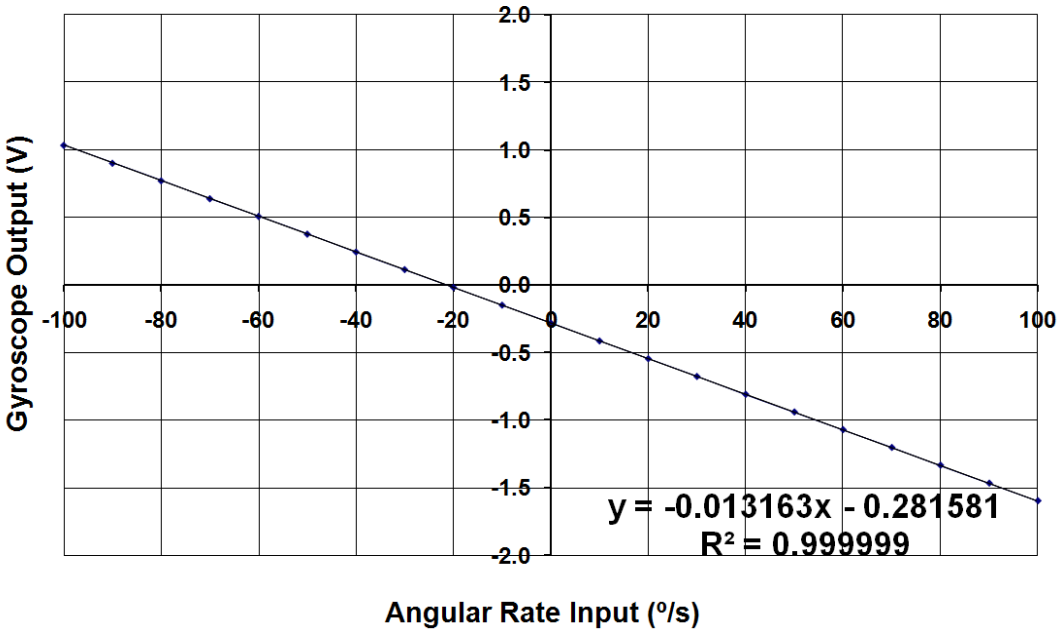

Figure 4.11: Measured scale factor and R2-linearity of the output response of the ARMS in a measurement range of ±100◦/s.

Table 4.1: Scale factor and nonlinearity for varying vacuum levels.

Pressure, mTorr	**Scale Factor, mV/(°/s)**	**R^2-Nonlinearity, %**	**Maximum % Deviation Nonlinearity**
40	-13.163	0.0001	0.04527
100	-13.142	0.0001	0.06049
200	-13.176	0.0001	0.05451
300	-13.149	0.0001	0.06184
400	-13.210	0.0002	0.04853
500	-13.213	0.0006	0.141

Although the mechanical bandwidth of the gyroscope is about 1 kHz at V_{PM}=35V, the bandwidth of the ARMS is currently limited to 10Hz by the readout electronics of the sense mode. Figure 4.12 shows the output of the ARMS in response to sinusoidal angular rate inputs with amplitude of 1.25 º/s and frequencies of 1, 2, and 4 Hz, verifying the constant sense mode output amplitude to time-varying angular rate inputs with same amplitude.

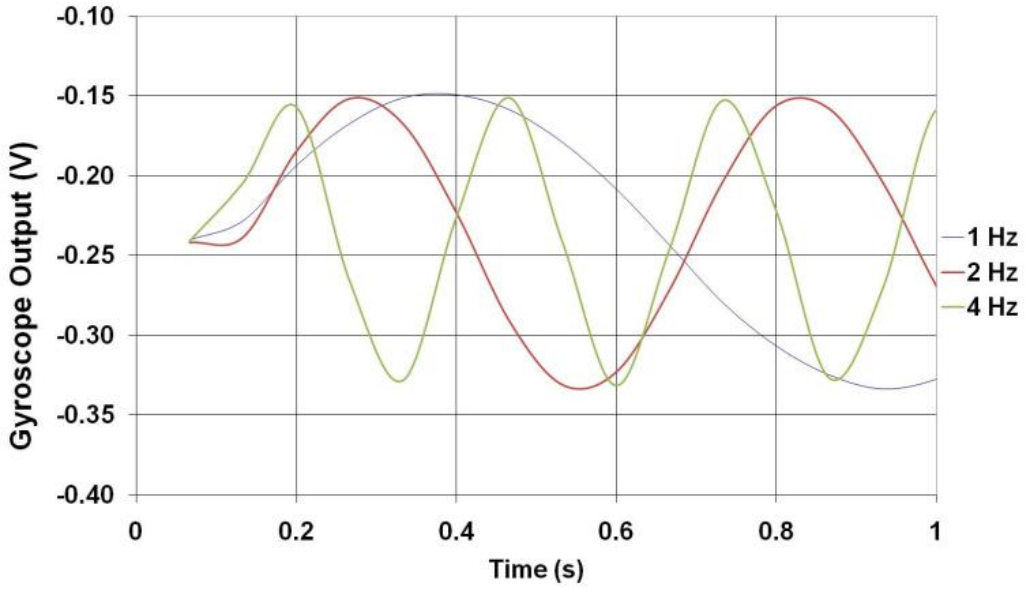

Figure 4.12: Output of the ARMS in response to sinusoidal angular rate inputs with amplitude of 1.25 º/s and frequencies of 1, 2, and 4 Hz.

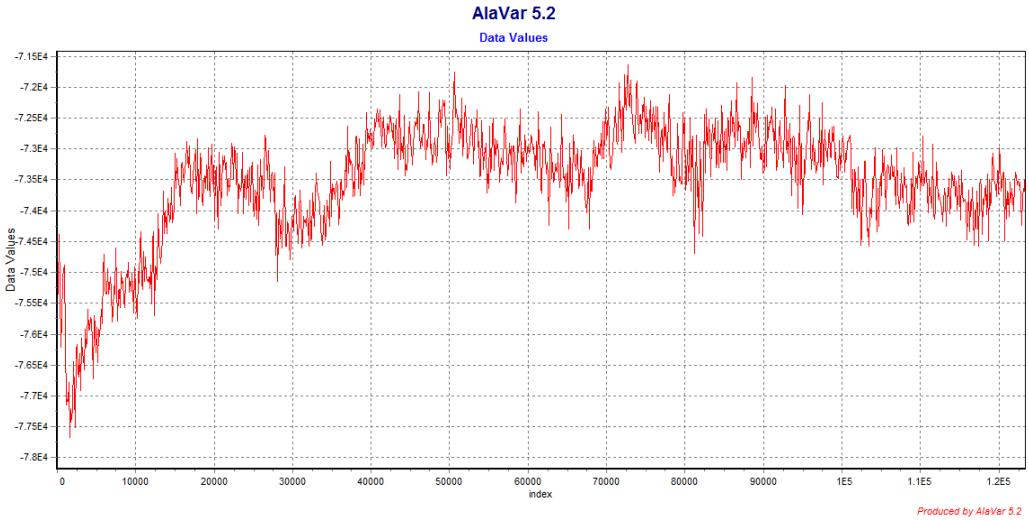

Figure 4.13: ZRO of the ARMS measured for 2 hours.

In order to determine the long term bias stability of the ARMS, the sense mode electrical output for zero applied angular rate input, or ZRO data is measured and collected for 2 hours. Figure 4.13 shows the plot of ZRO of the ARMS measured for 2 hours. In order to extract the bias stability and angle random walk from the ZRO data, Allan variance method is used. Allan variance is a mathematical tool that is used to predict the sources of noise terms observed at the collected ZRO data set using statistical methods. Figure 4.14 shows the Allan variance plot of the collected ZRO data, which gives the bias stability and angle random walk of the ARMS as 131 °/h (87 °/h /0.664) and 1.15 °/$\sqrt{h}$, respectively.

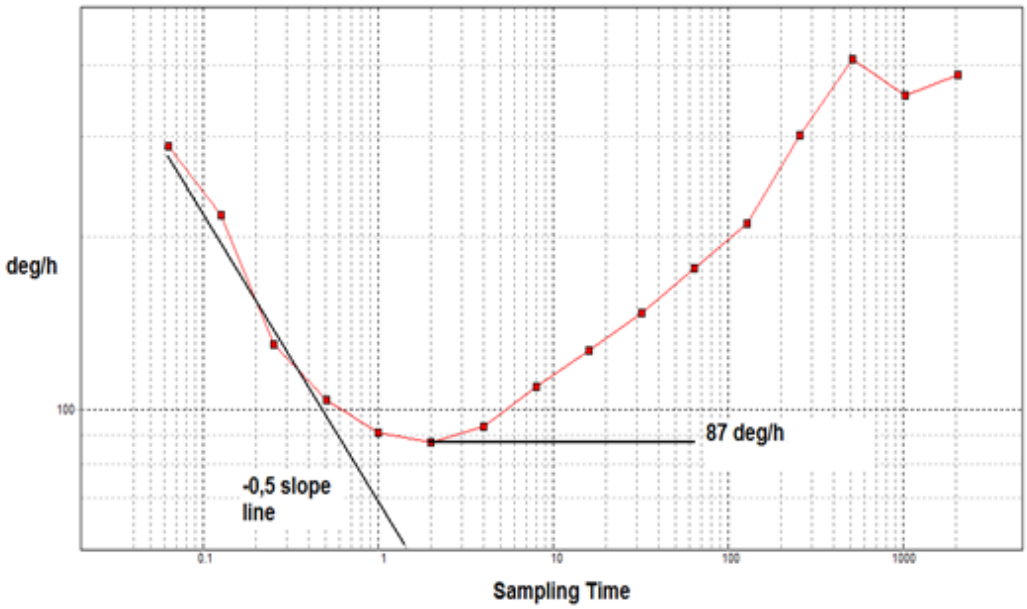

Figure 4.14: Allan variance plot of the ARMS ZRO measured for 2 hours.

4.3 Performance Comparison

Table 4.2 summarizes the performance parameters of some gyroscopes reported in literature, in order to compare the performance of the gyroscope developed in this research. In addition to bias drift, angle random walk and bandwidth, two figures of merit are defined in order to account for sensitivity and bandwidth at the same time, as given in Equations 4.1 and 4.2 for these gyroscopes.

$$FOM1 = \frac{Bandwidth}{Bias\ drift} \tag{4.1}$$

$$FOM2 = \frac{Bandwidth}{Angle\ random\ walk} \tag{4.2}$$

Table 4.2: Performance comparison table.

Gyroscope	**Bias Drift, º/h**	**Angle Random Walk, º/$\sqrt{\mathbf{h}}$**	**Bandwidth, Hz**	**FOM1**	**FOM2**
[15]	0.15	0.003	1	6.67	333
[25]	50	-	20	0.4	-
[27]	55	0.72	60 (projected)	1.09	83.33
[30]	200	5.47	10	0.05	1.82
[31]	14.3	0.126	10	0.7	79.36
This Study	131	1.15	1000	7.63	869

From Table 4.2 it is observed that presented gyroscope is not giving the best performance in terms of bias drift and angle random walk. On the other hand, when bandwidth is taken in account as given in FOM1 and FOM2 the presented gyroscope is showing superior performance. Hence, this gyroscope proves to be a wide-bandwidth gyroscope showing high-sensitivity to angular rate inputs.

4.4 Summary

This chapter demonstrated the characterization procedure and test setups used for the characterization of the fabricated gyroscope. The first tests on the probe station and the hybrid packaging of the fabricated gyroscopes are followed by the operational tests under vacuum environment. Obtaining drive and sense mode frequency responses, determination of the dependency of the sense mode frequency response to ambient vacuum conditions and V_{PM}, obtaining the scale factor and its dependency on vacuum conditions, determining the long term bias stability and angle random walk values of the gyroscope through operational tests are

demonstrated in this chapter. The chapter is concluded with the comparison of the performance parameters of the presented gyroscope with the previously reported gyroscopes.

CHAPTER 5

CONCLUSIONS AND FUTURE WORK

The research presented in this thesis involves the development of an environmentally robust, tuning-fork, mode-decoupled, high performance micromachined vibratory gyroscope, based on a never before reported 2 DoF sense mode mechanical oscillator. The designed micromachined vibratory gyroscope based on the proposed concept is fabricated at METU-MET facilities using the in-house silicon-on-glass micromachining technology. Characterization of the fabricated gyroscope proved the superior robustness of the novel 2 DoF oscillator sense mode design against ambient pressure variations with minimal mechanical sensitivity reduction when compared with matched-mode single DoF gyroscopes.

Based on the achievements and results of this study, following conclusions can be drawn:

1. Theory of 2 DoF mechanical oscillators is investigated in detail. It is concluded that SNR degradation problem observed in reported 2 DoF sense mode vibratory gyroscopes can be solved without losing from the robustness performance of the gyroscope. A novel 2 DoF sense mode oscillator for high performance applications is proposed, based on thorough theoretical study of 2 DoF mechanical oscillators.

2. Mechanics principles lying behind vibratory gyroscope designs are analyzed thoroughly. Through the complete use of mechanics principles, the dynamics of vibratory gyroscopes are investigated in detail and inherent

nonlinearities of vibratory gyroscopes originating from vibratory gyroscope dynamics are presented.

3. Electromechanical design of an environmentally robust, tuning-fork, mode-decoupled micromachined vibratory gyroscope based on the proposed 2 DoF sense mode oscillator is performed. Utilization of proof mass both as a decoupling element and the first mass of sense mode oscillator through the use of a dedicated 2 DoF flexible linkage is seen to be a feasible way when employment of die area is considered. In the mechanical design phase shock survivability against 1000 g acceleration loadings required for tactical and inertial-grade operations is also considered. It is concluded that, required shock survivability can be obtained by supporting the gyroscope structure evenly around the periphery. Through FEA simulations mode-decoupled 2 DOF sense mode oscillator operation immune to unwanted oscillation modes and extreme external acceleration loadings is verified.

4. It is concluded that, SOG fabrication process with a 100 μm structural layer is very suitable for elimination of unwanted oscillation modes, with careful design of peripheral anchorage through dedicated flexible linkages. Therefore, SOG process is chosen for fabrication of the designed gyroscope. Designed tuning-fork mode-decoupled micromachined vibratory gyroscope based on the proposed 2 DoF sense mode oscillator is fabricated at METU-MET facilities using the in-house SOG micromachining process, by Dr. Said Emre Alper. Size of a fabricated SOG gyroscope die is measured to be 5.1 x 4.6 mm^2.

5. Gyroscope samples are hybrid connected to external gyroscope electronics designed by Mr. Emre Şahin and Dr. Said Emre Alper to form the complete angular rate measurement system (ARMS). External gyroscope electronics were based on off-the shelf IC components. It is concluded through characterization of the ARMS in terms of operation bandwidth, scale factor, scale factor linearity, dependence of scale factor to ambient vacuum

conditions, long term bias stability and angle random walk that, proposed 2 DoF sense mode oscillator has the potential to be utilized in tactical-grade applications.

Although all of the major research objectives have been achieved within this research study, the performance of the designed gyroscope can be further improved by considering the issues listed below:

1. The band between the two resonance peaks of the 2 DoF sense mode oscillator is designed to be unnecessarily high due to poor fabrication tolerances as stated in Section 3.1.2. The SNR performance of the gyroscope is far below its potential limits, as unnecessarily high bandwidth of the 2 DoF design results in a decreased mid-band mechanical sensitivity, Therefore, DRIE undercutting problem resulting in poor fabrication tolerances should be investigated in detail. When fabrication tolerances are improved, bandwidth of 2 DoF oscillator can be designed to be below 50 Hz and by electrostatic tuning the flat mechanical sensitivity window of the sense mode can be set to 100 Hz around the operating frequency of the gyroscope. Optimum SNR performance with required bandwidth can be achieved by this way.

2. The capacitive gap of sense mode capacitor plates are fabricated at a minimum of ~ 3.5 μm due to poor fabrication tolerances, which severely limits the raw electrical sensitivity to angular rate inputs. Limited raw electrical sensitivity necessitates amplifier stages in the sense mode electronics, degrading the SNR performance due to electronics noise generated by amplifier stages. Hence, the necessity of investigation of DRIE undercutting problem is emphasized once more. On the other hand, in addition to improvements in fabrication tolerances, post process mechanisms to decrease the sense mode capacitive gaps need to be investigated. By this way capacitive gaps can be decreased controllably after the structures are released.

3. The vacuum pump connected to the rate table vacuum chamber is operated continuously during tests, as characterization tests need to be performed in vacuum environment of the rate table. On the other hand, this pump has a powerful motor to reach high vacuum conditions. This results in random vibrations around the rate table, prohibiting the observation of real ZRO performance of the gyroscope. Ways of packaging the gyroscope with vacuum proof packages need to be investigated in order to cope with this problem. Long term reliability of the vacuum packaged gyroscope will not be a problem, as the designed structure proves to be immune to vacuum leaks.

4. External off-the shelf electronic components interconnected on a printed circuit board (PCB) is a big source for electronics noise, degrading the SNR performance of the gyroscope. Designing dedicated CMOS circuits and hybrid connecting those with the mechanical sensor in a vacuum proof package is a good practice to improve SNR performance, therefore, ways to design dedicated CMOS circuits should be investigated.

In conclusion; major achievement of this research is the design of a novel 2 DoF sense mode oscillator for high performance gyroscope applications. During characterization study, gyroscopes based on the new 2 DoF design are observed to demonstrate the potential of tactical-grade operation while showing extreme immunity to environment pressure variations. Therefore, high long term reliability performance, which is one of the most important requirements for tactical and inertial-grade operations, is achieved without sacrificing from the SNR performance of the gyroscope.

REFERENCES

[1] J. S. Kilby, “The integrated circuit’s early history,” Proceedings of the IEEE. 2000, Vol. 88, 1, pp. 109-111, 2000.

[2] N. Yazdi and K. Najafi, “An All-Silicon Single-Wafer Micro-g Accelerometer with a Combined Surface and Bulk Micromachining Process,” Journal of Microelectromechanical Systems, Vol. 9, 4, pp. 544-550, 2000.

[3] J. Chae, H. Kulah, and K. Najafi, “A Monolithic Three-Axis Micro-g Micromachined Silicon Capacitive Accelerometer,” Journal of Microelectromechanical Systems, Vol. 14, 2, pp. 235-242, 2005.

[4] N. Yazdi, F. Ayazi, and K. Najafi, “Micromachined Inertial Sensors. Proceedings of the IEEE,” Vol. 86, 8, pp. 1640-1659, 1998.

[5] IEEE Standard for Inertial Sensors Terminology. IEEE Std 528-2001, 2001.

[6] IEEE Standard Specification Format Guide and Test Procedure for Single-Axis Interferometric Fiber Optic Gyros. IEEE Std 952-1997, 1997.

[7] S. E. Alper and T. Akin, “A Symmetric Surface Micromachined Gyroscope with Decoupled Oscillation Modes,” Sensors and Actuators A, Vols. 97-98C, pp. 337-348, 2002.

[8] S. E. Alper and T. Akin, “A Symmetrical and Decoupled Nickel Microgyroscope on Insulating Substrate,” Sensors and Actuators A, Vol. 115, 2-3, pp. 336-350, 2004.

[9] A. Sharma, et al. “A High Q In-Plane SOI Tuning-Fork Gyroscope,” Proceedings of IEEE Sensors ,Vol. 1, pp. 467-470, 2004.

[10] S. E. Alper and T. Akin, “A Single-Crystal Silicon Symmetrical and Decoupled MEMS Gyroscope on an Insulating Substrate,” Journal of Microelectromechanical Systems,Vol. 14, 4, pp. 707-717, 2005.

[11] S. E. Alper, K. M. Silay, and T. Akin, “Tactical-Grade Silicon-on-Glass Gyroscope with Very-Small Quadrature Coupling,” Proceedings of the 20th European Conference on Solid-State Transducers (Eurosensors XX), Vol. 1, pp. 56-57, 2006.

[12] S. E. Alper, K. M. Silay, and T. Akin, “A Low-Cost Rate-Grade Nickel Microgyroscope,” Sensors Actuators A, Vol. 132, 1, pp. 171-181, 2006.

[13] S. E. Alper, K. Azgin, and T. Akin, “High Performance SOI-MEMS Gyrocope with Decoupled Oscillation Modes,” Technical Digest of 19th IEEE International Conference on Micro Electro Mechanical Systems (MEMS 2006), pp. 70-73, 2006.

[14] M. F. Zaman, A. Sharma, and F. Ayazi, “High Performance Matched-Mode Tuning Fork Gyroscope,” Technical Digest of 19th IEEE International Conference on Micro Electro Mechanical Systems (MEMS 2006), pp. 66-69, 2006.

[15] A. Sharma, et al. “A 0. 1°/HR bias drift electronically matched tuning fork microgyroscope,” Technical Digest of the 21th International Conference on Micro Electro Mechanical Systems (MEMS 2008), pp. 6-9, 2008.

[16] W. Geiger, et al. “Decoupled microgyros and the design principle DAVED,” Sensors and Actuators A, Vol. 95, 2-3, pp. 239-249, 2002.

[17] C. Acar, and A. M. Shkel, “Nonresonant micromachined gyroscopes with structural mode-decoupling,” IEEE Sensors Journal, Vol. 3, 4, pp. 497-506, 2003.

[18] C. Acar, and A. M. Shkel, “Structurally decoupled micromachined gyroscopes with post-release capacitance enhancement,” Journal of Micromechanics and Microengineering, Vol. 15, pp. 1092–1101, 2005.

[19] X. Jiang, et al. “A Monolithic Surface Micromachined Z-Axis Gyroscope with Digital Output,” Digest of Technical Papers Symposium on VLSI Circuits, pp. 16-19, 2000.

[20] S. A. Bhave, et al. “An integrated, vertical-drive, in-plane-sense microgyroscope,” Proceedings of the 12th International Conference on Solid-State Sensors, Actuators and Microsystems (TRANSDUCERS 2003), Vol. 1, pp. 171-174, 2003.

[21] M. Kranz, et al. “Performance of a Silicon-on-Insulator MEMS gyroscope with digital force feedback,” Proceedings of Position Location and Navigation Symposium (PLANS 2004), pp. 7-14, 2004.

[22] X. Li, R. Lin, and K. W. Leow, “Performance-enhanced micro-machined resonant systems with two-degrees-of-freedom resonators,” Journal of Micromechanics and Microengineering, Vol. 10, pp. 534-539, 2000.

[23] C. Acar, and A. M. Shkel, “Inherently robust micromachined gyroscopes with 2-DOF sense-mode oscillator,” Journal of Microelectromechanical Systems, Vol. 15, 2, pp. 380-387, 2006.

[24] A. R. Schofield, et al. “Anti-Phase Driven Rate Gyroscope with Multi-Degree of Freedom Sense Mode,” Proceedings of the Solid-State Sensors,Actuators and Microsystems Conference (TRANSDUCERS 2007), pp. 1199-1202, 2007.

[25] J. A. Geen, et al. “Single-Chip Surface Micromachined Integrated Gyroscope With 50 deg/h Allan Deviation,” IEEE Journal of Solid-State Circuits, Vol. 37, 12, pp. 1860-1866, 2002.

[26] P. Greiff, et al. “Silicon monolithic micromechanical gyroscope,” Technical Digest of 6th International Conference on Solid-State Sensors and Actuators (Transducers’91), pp. 966-968, 1991.

[27] M. Weinberg, et al. “A micromachined comb-drive tuning fork gyroscope for commercial applications,” Proceedings of Sensor Expo, pp. 187-193, 1994.

[28] F. Ayazi and K. Najafi, “A HARPSS polysilicon vibrating ring gyroscope,” Journal of Microelectromechanical Systems, Vol. 10, 2, pp. 169-179, 2001.

[29] H. Xie, and G. K. Fedder, “Integrated Microelectromechanical Gyroscopes,” Journal of Aerospace Engineering, Vol. 16, 2, pp. 65-75, 2003.

[30] K. Azgin, Y. Temiz, and T. Akin, “An SOI-MEMS tuning fork gyroscope with linearly coupled drive mechanism,” Proceedings of IEEE 20th International Conference on Micro Electro Mechanical Systems (MEMS2007), pp. 607-610, 2007.

[31] Y. Temiz, “Advanced Readout and Control Electronics for MEMS Gyroscopes.,” Msc. Thesis Middle East Technical University, 2007.

[32] J. L. Meriam and L. G. Kraige, “Engineering Mechanics, Volume 2 Dynamics.,” John Wiley and Sons Inc., Fifth Edition, 2003.

[33] G.G. Coriolis, “Mémoire sur les équations du mouvement relatif des systèmes de corps,” Journal de l'école Polytechnique, Vol. 15, pp. 142-154, 1835 (in French).

[34] I. H. Shames, “Engineering mechanics, Statics and dynamics,” Fourth Edition, Prentice Hall, Upper Saddle River, N.J. 1997.

[35] S. G. Kelly, “Fundamentals of mechanical vibrations,” Second Edition, McGraw-Hill, Boston, 2000.

[36] J. He, and F. F. Zhi, “Modal analysis,” Butterworth-Heinemann, Oxford, Boston, 2001.

[37] D. K. Cheng, “Field and wave electromagnetics,” Addison-Wesley Pub. Co, Reading, Mass, 1989.

[38] C. Y. Warren, “Roark's formulas for stress and strain ,” McGraw-Hill, New York, 1989.

[39] A. M., Shkel, et al. “Dynamics and Control of Micromachined Gyroscopes,” Proceedings of the American Control Conference, 1999.

[40] T. B. Gabrielson, “Mechanical-thermal noise in micromachined acoustic and vibration sensors,” IEEE Transactions on Electron Devices, Vol. 40, 5, pp. 903-909, 1993.